UC Berkeley
UC Berkeley Electronic Theses and Dissertations

Title

Superconducting Circuits for Quantum Metrology with Nonclassical Light

Permalink

https://escholarship.org/uc/item/7z79m845

Author

Eddins, Andrew Wilson

Publication Date

2017

Peer reviewed|Thesis/dissertation

Superconducting Circuits for Quantum Metrology with Nonclassical Light

by

Andrew Wilson Eddins

A dissertation submitted in partial satisfaction of the

requirements for the degree of

Doctor of Philosophy

in

Physics

in the

Graduate Division

of the

University of California, Berkeley

Committee in charge:

Professor Irfan Siddiqi, Chair
Professor Hartmut Haeffner
Professor Jeffrey Bokor

Fall 2017

Superconducting Circuits for Quantum Metrology with Nonclassical Light

Abstract

Superconducting Circuits for Quantum Metrology with Nonclassical Light

by

Andrew Wilson Eddins

Doctor of Philosophy in Physics

University of California, Berkeley

Professor Irfan Siddiqi, Chair

The laws of quantum mechanics imply the existence of an intrinsic uncertainty, or noise, in the electromagnetic field. These noise fluctuations are central to many processes in atomic physics and quantum optics, including spontaneous emission of radiation by an atomic system, backaction on an atomic system during non-demolition measurement by probe light, and intrinsic bounds on the noise performance of an ideal amplifier. While quantum noise cannot be eliminated, the noise of one observable quantity may be reduced provided that of the conjugate observable is increased in accord with the relevant Heisenberg uncertainty relation; this process is known as squeezing.

Recently, superconducting circuits have emerged as a powerful platform for studying the interaction of squeezed light and matter, leveraging the low-dimensionality of the circuit environment to efficiently couple atomic systems to squeezed radiation. Beyond enabling the verification of canonical predictions of quantum optics, these experiments explore the potential utility of squeezing for the state readout of quantum bits, or qubits, used for quantum information processing.

In this thesis, we present three experiments probing the interaction of a superconducting qubit with squeezed radiation. First, we observe how the fluorescence spectra emitted by a two-level atomic system are modified by squeezing of a resonant drive. The subnatural linewidths of the resulting spectra provide the first successful verification in any system of predictions from nearly three decades prior, and provide a tool for characterization of microwave squeezed states. Second, we combine injected squeezed noise with a stroboscopic measurement scheme to demonstrate the first improvement of the signal-to-noise ratio of qubit state readout due to input squeezing. This study includes a characterization of the effect of squeezing on measurement backaction, exhibiting the first use of squeezing to slow measurement-induced dephasing. Finally, we develop a circuit incorporating the qubit inside of a squeezed-microwave source and extensively study the measurement physics of this hybrid system. This device enables the transfer of quantum information from the qubit at $\sim$30 milliKelvin to a room temperature detector with a marked increase in steady-state efficiency.

Contents

List of Figures

Acknowledgments

It has been a privilege to have many thoughtful, talented, and kind individuals as friends, mentors, and supporters during graduate school.

Thanks first to Prof. Irfan Siddiqi for the opportunity to work in the Quantum Nanoelectronics Lab. Irfan has an unusual capacity for intensely pursuing the high-level needs of the lab while simultaneously maintaining a deep understanding of the latest technical developments. His commitments to education and professionalism are equally admirable and important components of the lab's success and growth. It's been a pleasure to work with Irfan, and to learn skills from him ranging from subtleties of device fabrication, to how to give a clear presentation, to the proper taste in upper-tier automobiles.

Thanks to the other members of my thesis committee, Profs. Hartmut Haeffner, Jeffrey Bokor, and Jonathan Wurtele, for their time, feedback, and support in this endeavor.

Thanks also to our collaborators outside QNL, particularly the teams of Profs. Aashish Clerk, Alexandre Blais, and William Oliver, and to the cQED community more broadly.

This research would not have been possible without the support of the Berkeley Physics staff. Thanks especially to Anne Takizawa, Donna Sakima, Anthony Vitan, Katalin Markus, Carlos Bustamante, Eleanor Crump, Stephen Raffel, Joseph Kant, and Warner Carlisle.

A major perk of working in QNL has been learning from excellent post-docs. Particular thanks to those I worked with more closely, in rough chronological order: Rajamani Vijayaraghavan, for investing a great deal of time and effort training me and helping me get oriented in the lab when I wandered in as a first-year. Shay Hacohen-Gourgy, for answering my many questions with seemingly infinite patience, and for keeping the lab a fun place to be. David Toyli, for being available as my go-to mentor for most everything, and acting as a role model of scientific professionalism. And Sydney Schreppler, for the scientific, academic, and professional advising, and for generally helping me keep it together in the final stretch of the Ph.D. Thanks also to Kater Murch, Andy Schmidt, Nico Roch, Allison Dove, Emmanuel Flurin, Kevin O'Brien, James Colless, and Machiel Blok for their collective guidance.

My fellow graduate students in QNL were equally important to my time in Berkeley. Thanks to Eli Levenson-Falk, Natania Antler, Ned Henry, Steve Weber, Chris Macklin, Mollie Schwartz, Leigh Martin, Vinay Ramasesh, Will Livingston, John Mark Kreikebaum, Marie Lu, Brad Mitchell, and Dar Dahlen for being awesome labmates, teachers, sympathizers, co-conspirators, and climbing buddies. It was a delight and good fortune to work with John Mark on the QPA project; his persistence, creativity, and meticulousness were central to the device and results in Chapter 6. Jeff Birenbaum and Sean O'Kelley of Clarke Lab were also immensely helpful. Thanks also to (former) undergrads Aditya Venkatramani, Nick Frattini, Reinhard Lolowang, Dirk Wright, and Jack Qiu for their excellent work.

Most importantly, thanks to my family for their unwavering support, to my girlfriend Vicky Xu for making the bad days bearable and the average days celebrations, and to my friends near and far for filling these years with many great memories.

Select Scientific Works

While this thesis is built upon the many scientific works cited in the bibliography and more broadly is indebted to the superconducting-circuit and atomic-physics communities, the following scientific papers were produced en route to this thesis.

- D.M. Toyli*, A.W. Eddins*, S. Boutin, S. Puri, D. Hover, V. Bolkhovsky, W.D. Oliver, A. Blais, and I. Siddiqi, "Resonance Fluorescence from an Artificial Atom in Squeezed Vacuum," *Physical Review X* **6**, 031004, July 2016 [1].

- S. Boutin, D.M. Toyli, A.V. Venkatramani, A.W. Eddins, I. Siddiqi, and A. Blais, "Effect of Higher-Order Nonlinearities on Amplification and Squeezing in Josephson Parametric Amplifiers," *Physical Review Applied* **8**, 054030, November 2017 [2].

- N. Roch*, M.E. Schwartz*, F. Motzoi, C. Macklin, R. Vijay, A.W. Eddins, A.N. Korotkov, K.B. Whaley, M. Sarovar, and I. Siddiqi, "Observation of Measurement-Induced Entanglement and Quantum Trajectories of Remote Superconducting Qubits," *Physical Review Letters* **112**, 170501, April 2014 [3].

- A. Eddins, S. Schreppler, D.M. Toyli, L.S. Martin, S. Hacohen-Gourgy, L.C.G. Govia, H. Ribeiro, A.A. Clerk, and I. Siddiqi, "Stroboscopic Qubit Measurement with Squeezed Illumination," *arXiv*:1708.01674, August 2017 [4].

- "High-Efficiency Measurement of an Artificial Atom inside a Parametric Amplifier," in preparation.

---

*Equal contributors

Chapter 1

Introduction

1.1 Quantum circuits and measurement

The development of increasingly complex quantum-coherent systems using superconducting circuits has been driven by potential high-impact applications including cryptanalysis [5], database search [6], simulation of chemical properties and dynamics [7, 8, 9], and basic research into quantum mechanics. In comparison with other popular quantum platforms such as trapped ions, nitrogen-vacancy centers, or semiconducting qubits, superconducting circuits have several strengths. These strengths include system-size scalability facilitated by well-established lithographic fabrication and materials processing technology, high customizability of atomic properties and couplings, and ready availability of microwave control electronics and associated microwave engineering knowledge already developed by the communications and defense industries. Exploiting these strengths has enabled steady improvement of superconducting qubit lifetimes from the first reported value of 1 ns in 1999 [10] to modern qubits which commonly exhibit lifetimes on the order of 10 to 100 μs [11, 12, 13, 14], making accessible increasingly complex classes of experiments. Despite this progress, to date the requirements for universal quantum computation remain daunting, requiring integration of large numbers of individually controllable qubits on-chip with minimal crosstalk effects, high-fidelity single- and multi-qubit gate operations, and high-fidelity qubit measurement for error-correction and final state readout.

Qubit measurement poses a particularly interesting problem, requiring first the efficient transfer of information from a qubit to an itinerant microwave field, and second the room-temperature detection of this signal, which originates inside a dilution refrigerator and often corresponds to only a few microwave photons (energetically comparable to $\sim$100 milliKelvin). The first step was largely addressed by the development of circuit quantum-electrodynamics (cQED) techniques [15], the circuit analogue of cavity quantum-electrodynamics [16], enabling, among many other results, the approximately ideal transfer of state information from a qubit to a microwave transmission line by means of a highly detuned linear resonant circuit. The second step has driven the development of superconducting microwave am-

plifiers capable of increasing signal powers by orders of magnitude while adding almost no more noise than required by fundamental quantum mechanics. These amplifier technologies, first explored in the 1970's and 80's [17], then more recently intensely developed for cQED applications, have culminated in qubit readout with fidelities of $\sim 99\%$ or more with acquisition times on the order of ~ 100 ns [18, 19], and have enabled a generation of experiments studying e.g. wavefunction-collapse dynamics such as discrete quantum jumps [20], continuous quantum trajectories [21, 22], measurement-induced entanglement [3], and quantum feedback [23] including application to quantum error-correction [24], among others. However, as the major scientific goal of universal quantum computation requires increasing both system size and algorithmic complexity by many more orders of magnitude, improvements in measurement technology are expected to remain desirable for facilitating error-correction and final state readout.

Standard qubit measurements are performed by probing the qubit using coherent electromagnetic states, arguably the closest quantum analogue to the sinusoidal behavior of a classical light field; a natural question is whether other, more distinctly quantum fields might be advantageous for performing measurements faster or with lower power. Specifically, superconducting amplifiers have long been recognized not only as a means of achieving gain with ultra low-noise but also as a source of squeezed radiation [25, 26, 27, 28], famous as a means of lowering the noise-floor in some measurements below that set by the intrinsic fluctuations of the electromagnetic vacuum. The development of squeezing in the optical spectrum has a long history [29, 30], leading to recent applications including enhancing the sensitivity of gravitational wave detectors [31, 32]. Squeezing microwave-frequency fields has surged as a topic of interest in the modern contexts of cQED and dark matter detection [33] given the ability to couple squeezed fields to low-dimensional quantum systems such as superconducting qubits [34, 1, 35], optomechanical circuits [36, 37], or spin ensembles [38]. The interaction of squeezed microwaves with superconducting qubits with an emphasis on potential applications to measurement is the subject of the experiments in this thesis. The remainder of this chapter introduces some of the basic building blocks underlying these experiments.

1.2 The Josephson junction as a nonlinear inductor

Here we briefly motivate the AC and DC Josephson relations [39] from basic quantum mechanics, following an argument akin to the more complete presentation in [40], then proceed to derive the Josephson inductance, the nonlinear quantity central to all superconducting qubits and amplifiers in this thesis. Consider two superconducting regions separated by a thin non-superconducting barrier. We model the superconducting state as the wavefunction $\psi(x) = \sqrt{n}e^{i\phi(x)}$, where n is the density of Cooper-pairs of electrons and ϕ is the phase of the field. We label the wavefunction phases just to the left and right of the barrier, respectively, as $\phi(x < 0) = \phi_1$ and $\phi(x > 0) = \phi_2$ for sufficiently small $|x|$, where for simplicity we assume the barrier has negligible width (delta-function approximation). We represent

the Josephson junction as the narrow tunnel-barrier in the energy potential $U(x)$ for a single Cooper pair as drawn in Fig. 1.1. Applying an electrical potential difference V across the junction as depicted in the inset circuit diagram causes the potential energy difference $U(x < 0) - U(x > 0) = -qV$, where $q = -2|e| = -2e$ is the charge of a Cooper pair. Kirchoff's current rule and the assumption n is approximately independent of x implies the same current and same kinetic energy on both sides of the junction, so the total energy difference between the left and right regions is $-qV$. Thus over time t we expect ψ_2 to accumulate the additional phase $\delta = -qVt/\hbar = 2eVt/\hbar$ relative to ψ_1 per the time-dependent Schrödinger equation [41]. Taking the time derivative of this phase yields the AC Josephson relation,

$$\dot{\delta} = V/\varphi_0, \tag{1.1}$$

where $\varphi_0 = \hbar/2e$ is the reduced flux quantum. The AC Josephson relation gets its name from how the tunneling of a Cooper pair necessarily produces a photon with frequency $\omega = qV/\hbar$, such that applying a constant voltage produces an AC response at ω.

The DC Josephson relation describes the current passing through the junction in terms of δ. The quantum mechanical expression for electrical current in one dimension is

$$I = \frac{\hbar q}{4im_e}(\psi^* \psi' - \psi \psi^{*'}). \tag{1.2}$$

The spatial derivative at the junction should be proportional to the difference of the wavefunction just to the right and left of the junction, $\psi' \propto \lim_{\epsilon \to 0} \psi(\epsilon) - \psi(-\epsilon)$, while symmetry requires the wavefunction itself takes the mean value $\psi = \lim_{\epsilon \to 0}(\psi(\epsilon) + \psi(-\epsilon))/2$, giving

$$I \propto \frac{(e^{-i\phi_1} + e^{-i\phi_2})(e^{i\phi_2} - e^{i\phi_1})}{2} - \frac{(e^{i\phi_1} + e^{i\phi_2})(e^{-i\phi_2} - e^{-i\phi_1})}{2} = (e^{i\delta} - e^{-i\delta}). \tag{1.3}$$

Identifying the overall proportionality constant as the critical current I_0 gives

$$I = I_0 \sin \delta, \tag{1.4}$$

a consequence of which is that a DC current may flow through the Josephson junction even when $V = 0$.

Taken together, the Josephson relations imply the junction acts as a nonlinear inductance. Combining the equations gives

$$\dot{I} = \frac{I_0 \cos \delta}{\varphi_0} V. \tag{1.5}$$

Since inductance is generally defined by $L = V/\dot{I}$, we identify the Josephson inductance

$$L_J = \frac{\varphi_0}{I_0 \cos \delta} = \frac{\varphi_0}{\sqrt{I_0^2 - I^2}} = L_{J,0}\left(1 + \frac{1}{2}(I/I_0)^2 + ...\right), \tag{1.6}$$

which for small current approaches the value $L_{J,0} = \varphi_0/I_0$.
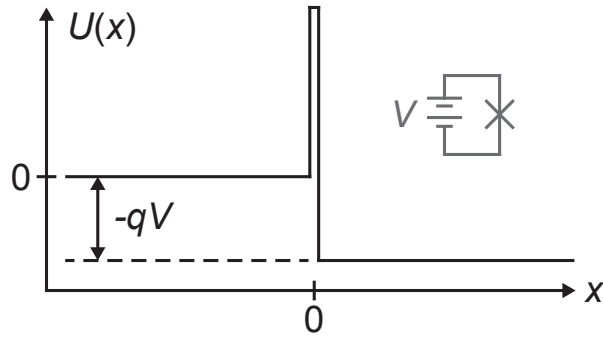
Figure 1.1: Simple model of a Josephson junction with an applied voltage bias.

Putting two Josephson junctions within a superconducting loop forms a Superconducting Quantum Interference Device (SQUID, specifically a dc-SQUID), which has a net inductance that can be tuned via an applied flux. This can be shown mathematically by requiring that the phase ϕ be single-valued at all points around the loop, the end result of which is an inductance of the same form as Eq. 1.6 but with the replacement

$$I_0 \to I_c(\Phi_{\mathrm{app}}) = 2I_0 \cos(\frac{\pi \Phi_{\mathrm{app}}}{\Phi_0}), \tag{1.7}$$

where Φ_{app} is the magnetic flux applied through the SQUID loop. When $\Phi_{\mathrm{app}} = 0$, the standard prediction for two inductors in parallel is recovered. Inspecting the expression for the SQUID inductance,

$$L_J = \frac{\varphi_0}{2I_0 \cos(\frac{\pi \Phi_{\mathrm{app}}}{\Phi_0}) \cos \delta}, \tag{1.8}$$

we see the inductance can be modulated either by varying the flux through the loop Φ_{app}, or by running a large oscillating current through the loop to cause δ to vary. Later chapters discuss how these two $1/\cos$ factors respectively enable amplification produced by flux-pumping or current-pumping methods.

1.3 Superconducting quantum bits

An ideal quantum bit, or qubit, is a quantum system with only two levels, such that its properties are isomorphic to those of a spin-1/2 object. In contrast, an electromagnetic field mode such as the resonant mode of an LC circuit is a harmonic oscillator, which has an infinite number of equally spaced energy levels corresponding to the presence of integer numbers of photons. Whereas a resonant drive applied to a qubit shuttles probability density back and forth between the two levels (Rabi oscillations), resonantly driving an LC circuit as in Fig. 1.2(left) drives transitions between all levels at once, producing a Poisson distribution

of probability density over the ladder of levels. Achieving qubit-like behavior thus requires the introduction of some nonlinear element to lift the degeneracy of the energy level spacing so as to spectrally isolate a single transition.

From the previous section, we conclude that replacing the linear inductance of an LC resonator with a Josephson junction of sufficiently small I_0 will create a nonlinear, or anharmonic, oscillator whose energy levels are no longer evenly spaced, as in Fig. 1.2(right). Each transition may now be individually addressed by driving at the respective resonance frequency, such that the lowest pair of levels acts as an effective qubit. The experiments in this thesis employ transmon-style qubits [42, 43], a popular, simple design consisting of a Josephson-junction in parallel with a large capacitance that helps reduce sensitivity to charge noise, though a variety of other architectures are possible, e.g. capacitively-shunted flux qubits [13] or fluxonium qubits [44]. A typical transmon qubit design has a fundamental resonance frequency in the 4-5 GHz range, and an anharmonicity (detuning of lowest two transitions in the ladder) on the order of 200 MHz.

A qubit requires the use of a low critical-current junction such that the nonlinearity is significant even for a single quantum excitation. Alternatively, the same circuit topology may be made with a high critical-current junction (and the capacitance adjusted accordingly), such that the nonlinearity does not become significant until the excitation number is well into the classical regime; this realizes a quantum-limited amplifier known as the Josephson parametric amplifier. These amplifiers are the subject of the next two chapters. The experiments described in later chapters are built out of combinations of qubits and amplifiers, which one might lyrically describe as the quantum and classical versions of the same nonlinear circuit.

1.4   Thesis Overview

This thesis consists of the following parts. The first half of Chapter 2 deliberately neglects quantum mechanics in order to provide a gentle introduction to the Josephson Parametric Amplifier (JPA), the workhorse of this thesis, including the underlying general operating principle of parametric amplification and its particular realization in the JPA circuit. The second half of Chapter 2 aims to make these ideas more concrete by presenting several JPA devices and discussing circuit design in some detail, including a presentation of measurements indicating that Josephson junction arrays can improve amplifier performance. Chapter 3 provides a quantum description of the JPA and of the microwave squeezed states produced by the circuit. This chapter aspires to be a pedagogical tutorial for any experimentalist desiring an understanding of squeezed-state and quantum-amplification fundamentals, and includes the prerequisite theory common to the experiments discussed in later chapters. The cheat-sheet of equations relating measures of squeezing to measures of amplifier gain in this chapter will hopefully be a convenient reference for future experimentalists.

Chapters 4, 5, and 6 discuss experiments with the common theme of the interaction of squeezed light (microwaves) and matter. Chapter 4 presents measurements of resonance
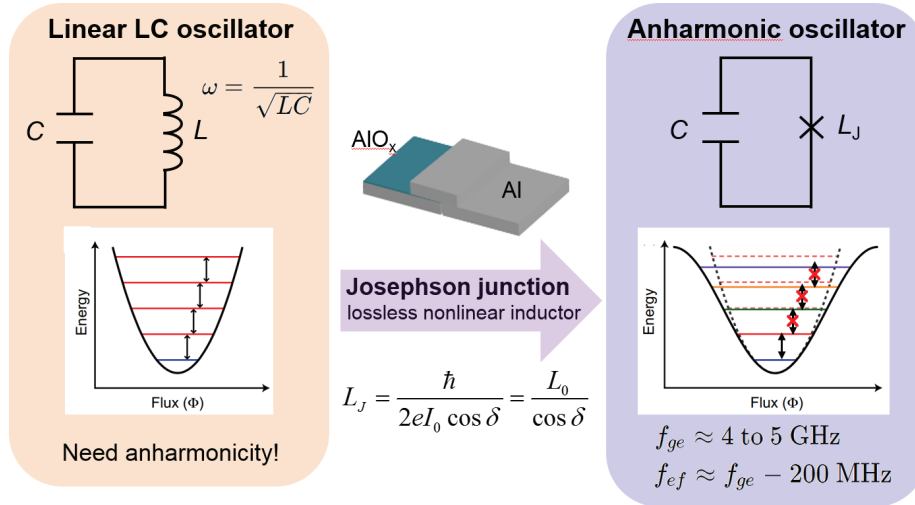
Figure 1.2: Introducing a strongly nonlinear component such as a low critical-current Josephson junction produces a ladder of unequally spaced energy states, such that the lowest pair of levels forms a spectrally isolated two level system, or qubit.

fluorescence from a two-level system under squeezed excitation, confirming two canonical predictions that had gone unverified for nearly three decades. Chapter 5 presents the first use of injected squeezed microwaves to improve the signal-to-noise ratio of a qubit measurement, along with the first demonstration of using squeezed microwaves to slow measurement backaction by increasing pointer-state overlap. Finally, Chapter 6 presents measurements of a hybrid device integrating a qubit on-chip with a JPA enabling qubit measurement with record-breaking steady-state efficiency of the transfer of qubit state information from the qubit to room-temperature.

While hopefully readable as a stand-alone reference, this thesis spends little time on several relevant topics that have been covered in some detail by other recent theses from the same lab, including the Jaynes-Cummings Hamiltonian and dispersive readout [45, 46, 47, 48], device fabrication procedures [45, 46, 49], and the Josephson Traveling Wave Parametric Amplifier (JTWPA) [50]. The curious reader may consult those sources for further details.

Chapter 2

The Josephson Parametric Amplifier: Fundamentals and Hardware

2.1 Classical intuition for parametric amplification

A minimal classical model of a parametric amplifier provides intuition capturing many aspects of device behavior, extending even to the generation of squeezing. We consider a particle oscillating in a time-dependent one-dimensional parabolic potential, $V(x,t) = x^2(1+\epsilon\cos(\omega_p t))$, as shown in Fig. 2.1. Here ϵ represents a small modulation of the steepness of the parabolic potential; in the following we assume $\epsilon \ll 1$. If $\epsilon = 0$, the particle oscillates in the harmonic potential with a resonance frequency ω_0. When $\omega_P = 2\omega_0$ with non-zero ϵ, *phase-sensitive amplification* occurs in which the gain depends on the phase of the oscillation being amplified relative to the modulation. If the particle was initialized such that it oscillates in-phase with the modulation ($x(t) \propto \cos(\omega t)$), then the potential does work on the particle by steepening when the particle is near the extrema of its oscillations, transferring energy to the spatial oscillations twice per cycle. In contrast, if the particle oscillates out-of-phase with the modulation ($x(t) \propto \sin(\omega t)$), the reverse process occurs and energy is transferred from the particle to the drive modulating the potential. The more general case of a particle oscillating with some arbitrary initial phase can be written as a sum of in-phase and out-of-phase components, often referred to as the I and Q quadratures of the oscillation. Thus one quadrature (cos) of the oscillation is amplified while the other (sin) is deamplified. This classical picture leads one to correctly guess that, if we initialize the oscillator in its quantum ground state (vacuum state), which has equal fluctuations in both quadrature phases, the fluctuations in one quadrature will be deamplified, producing a squeezed state.

In contrast, if we detune the modulation frequency sufficiently, then any oscillation will drift in and out of phase with the pump. This averages over the amplification and deamplification conditions, resulting in an average gain that is lower than phase-sensitive amplification for the same ϵ, but now amplifying both oscillation quadratures. Because both quadratures are amplified equally, the phase of the oscillation is not changed by the amplification pro-
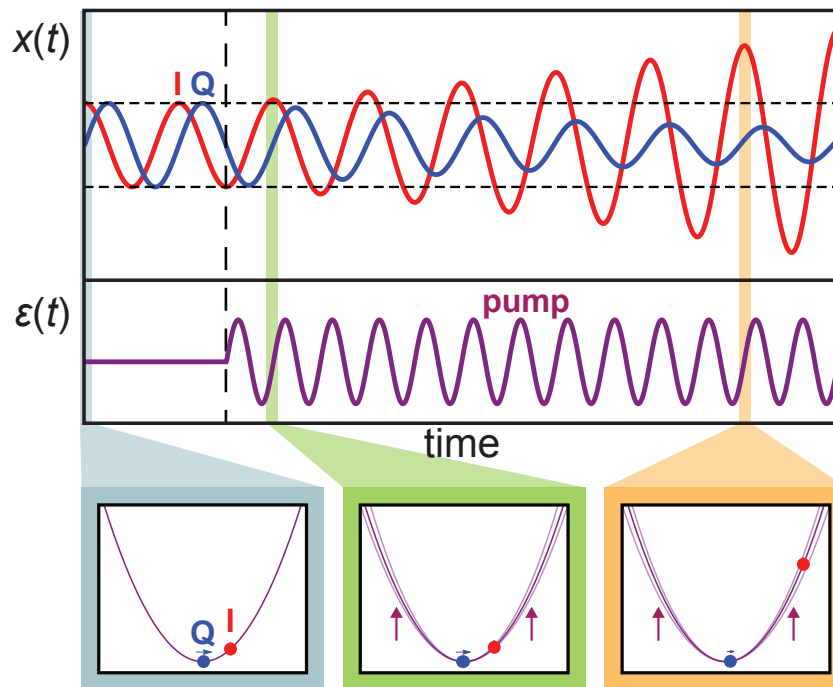
Figure 2.1: Dynamics of a classical parametric amplifier. We consider two particles oscillating in a parabolic potential initialized here with equal amplitudes but orthogonal phases. These represent the two quadrature components of the field in a parametric amplifier. The three lower panels indicate snap-shots of the positions and movements of the particles and of the potential itself. Initially the particles oscillate with fixed amplitude (blue snapshot). After some time (vertical dashed line), an energy source we call the pump begins modulating the potential at twice the oscillation frequency ($\varepsilon(t)$ corresponds to $\epsilon \cos(\omega_p t)$ in the text). The I particle is in-phase with the modulation such that the potential raises when the particle is at an extremum (green snapshot), doing work on the particle by raising it and thus increasing the oscillation amplitude of over time, whereas the opposite process occurs for Q. (Contact me if you would like the animated version of this figure).

cess. This mode of operation is thus often referred to as *phase-preserving* amplification. As discussed later in this chapter and the next, these two modes of operation produce strikingly different outcomes when amplifying signals with noise, such as vacuum-noise limited signals.

2.2 The Josephson parametric amplifier

The Josephson parametric amplifier (JPA) is a superconducting amplifier widely used for qubit measurement and for generating squeezed microwaves. The JPA utilizes the general
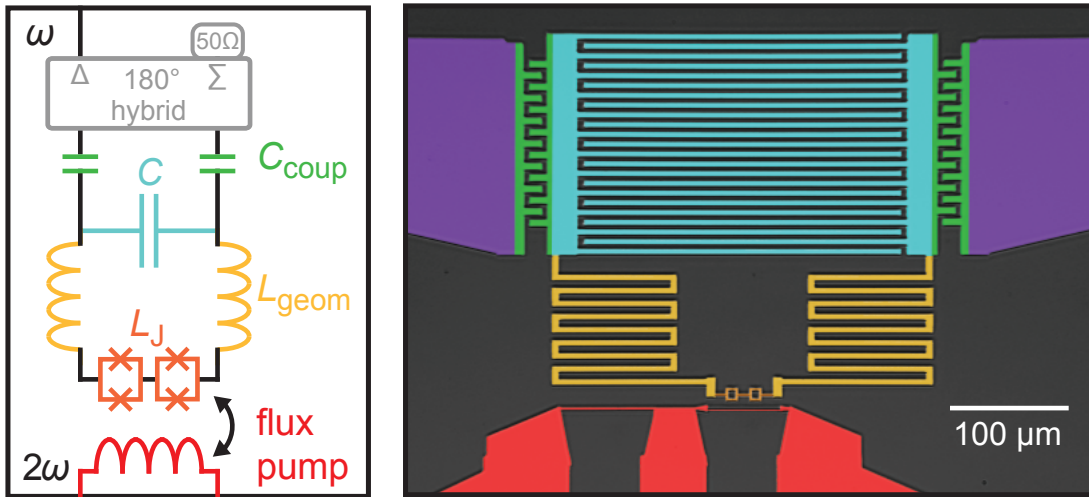
Figure 2.2: Schematic and false-colored photograph of a Josephson parametric amplifier (JPA), reproduced from [1]. The JPA is an LC oscillator wherein the inductance L_J, and thus the resonant frequency, can be modulated by a pump tone. Several pumping schemes are possible; here, the pump line (red) carries a drive at twice the oscillator resonance frequency which modulates L_J via inductive coupling to the SQUID loops (orange).

process described above, consisting of a microwave resonator whose resonance frequency can be modulated via an applied pump tone. The large number of photons in the pump tone permits understanding and simulating many aspects of JPA performance via classical intuition, while the very low loss in the JPA makes the device quantum coherent, allowing for efficient detection of very small measurement signals (usually ~ -120 dBm or less) and for the reduction of quadrature noise below that of vacuum.

Figure 2.2 shows an example of a JPA. A typical JPA consists of one or more Superconducting Quantum Interference Devices (SQUIDs, orange in the figure) shunted by a capacitor (cyan) and connected to a transmission line[1]. The device operates in reflection, with a microwave circulator (not shown) routing signals into and out of the JPA via the port (purple) near the top of the figure[2]. The SQUIDs act as a nonlinear inductance L_J which increases with current. Per Eq. 2.1, the inductance can be increased either by applying flux through the SQUID loops, thus producing circulating currents in the SQUIDs, or by driving current

---

[1]Alternately, a distributed resonator such as a $\lambda/4$ resonator may be used instead of a lumped-element circuit. This introduces additional high-frequency modes into the amplifier, which can be useful [51] or detrimental depending on the application.

[2]In the differential circuit geometry shown here, a microwave hybrid (gray) first converts the incoming single-ended signal (voltage excitation referenced to ground) into a differential signal (antisymmetric voltage across the JPA), which protects the device from any noise on ground or other common-mode noise. Single-ended JPA geometries are also possible and commonly used.
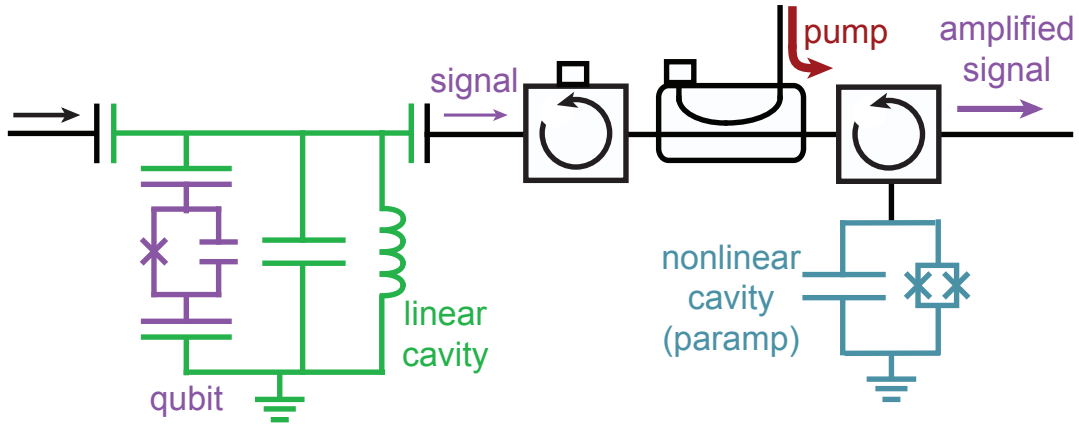
Figure 2.3: Example qubit-measurement circuit. A qubit (purple) is capacitively coupled to a readout resonator (green), causing the cavity resonance frequency to shift depending on $\hat{\sigma}_z$ of the qubit. A readout tone near ω_c is transmitted through the cavity and routed to a JPA (blue). A microwave pump tone, here a current-pump at or near the signal and JPA frequencies, modulates the JPA frequency, producing near quantum-limited amplification of the signal.

across the SQUIDs directly. Thus the resonance frequency of the circuit can be modulated by applying a flux-pump [52] via the shorted coplanar waveguide (red), or by applying a current-pump via the signal port (purple). A static flux-bias Φ_{dc} allows the JPA operating frequency to be tuned by up to an octave in some devices. Since the JPA resonance frequency is locally odd in flux (when $\Phi_{dc} \neq 0$) but even in current, modulation at $2\omega_0$, and thus parametric gain and squeezing, is produced by a flux-pump at $2\omega_0$ or by a current-pump near ω_0. Several other pumping schemes exist, including sideband pumping ("double-pumping") [53, 2, 54] and even subharmonic pumping [55].

Flux-pumping can be understood as a 3-wave mixing process in which a pump photon at $\omega_p = 2\omega_0$ is converted to a pair of signal (ω_s) and idler (ω_i) photons with $\omega_p = \omega_s + \omega_i$, while current-pumping is a 4-wave mixing process in which two pump photons are converted to the signal and idler photons with $2\omega_p = \omega_s + \omega_i$. Of central importance to squeezing, both processes populate the field inside the JPA with correlated pairs of photons (as directly measured in [35]), producing e.g. reduced amplitude fluctuations of the microwave field corresponding to photon antibunching[3]

By efficiently amplifying the input signal, a JPA allows qubit measurements to be performed with less time spent averaging away noise. Fig 2.3 shows one possible qubit measurement circuit incorporating a JPA. A microwave tone transmitted through the readout cavity

---

[3]Though in general it is possible for a quantum state to exhibit squeezing without photon pairs, e.g. the superposition $|0\rangle + |1\rangle$. [56, 29]

(green) acquires a phase shift that depends on the state of the qubit (purple). This measurement tone is typically quite small, perhaps ~ -130 dBm, and therefore must be amplified by many orders of magnitude before it can be detected in the presence of room-temperature thermal noise. It is very generally true that the signal-to-noise ratio (SNR) at the output of an amplifier is less than or equal to the SNR at its input. Ideally, the noise added by each amplifier will be small compared to the noise incident to that amplifier, preserving SNR. Fig. 2.4(a) illustrates how even the lowest-noise commercial non-superconducting amplifier (a high electron-mobility transistor (HEMT) amplifier from Low Noise Factory) adds the equivalent of ~ 10 photons of noise, degrading the power SNR by a factor of ~ 20. A JPA or other superconducting preamplifier upstream of the HEMT, as in Fig. 2.4(b), can be used to amplify the signal by ≥ 20 dB such that the noise added by the HEMT or other lossy components becomes negligible. An ideal JPA operated in phase-preserving mode adds only half a photon of noise, dramatically improving SNR at the end of the amplification chain and reducing necessary averaging times by the same factor. Empirically, overall SNR improvements of 12-16 dB are typical. For measurements of a single known quadrature, the JPA may be operated in phase-sensitive mode in which it ideally adds no noise, providing an additional 3 dB of SNR at the cost of experimental complexity.

2.3 JPA design guidelines

JPA design has been rigorously theoretically analyzed in a number of sources [57, 58, 59, 2]. Here we provide a brief overview of design guidelines light on derivations, focusing on the case of a lumped-element JPA. A starting point for JPA design is an LC resonator consisting of a Josephson inductance L_{J} in parallel with a capacitance C, with the two nodes respectively connected to the center-pin and ground of a transmission line of characteristic impedance Z, similar to the JPA in Fig. 2.3. We use these two design degrees of freedom, L_{J} and C, to set the resonant frequency of the JPA, $\omega_0 = (L_{\mathrm{J}}C)^{-1/2}$, and the coupling of the JPA to the transmission line, $\kappa_{\mathrm{ext}} = \omega/Q_{\mathrm{ext}} = (ZC)^{-1}$. Per Eq. 1.6, a static flux bias applied through the SQUID loop(s) increases L_{J} according to

$$L_{\mathrm{J}} \approx \frac{\varphi_0}{I_c(\Phi_{\mathrm{app}})} = \frac{\varphi_0}{I_{c,0}\cos(\frac{\pi\Phi_{\mathrm{app}}}{\Phi_0})}, \tag{2.1}$$

allowing ω_0 to be tuned downward from its zero-flux value. Here $I_c(\Phi_{\mathrm{app}})$ is the critical current of the SQUID when the SQUID is threaded by the externally applied flux Φ_{app}. Equation 2.1 is strictly valid only when the current driven across the SQUID is small compared to $I_c(\Phi_{\mathrm{app}})$, so this equation is used to predict the linear or low-power resonance frequency, with the expectation that an applied current pump will shift the resonance down by an amount $\sim \kappa$ (usually a negligible distinction at the design stage).

The coupling κ_{ext} influences device behavior in several ways. For a given gain, the amplifier bandwidth, defined here as the full-width half-max (FWHM) of the gain as a function
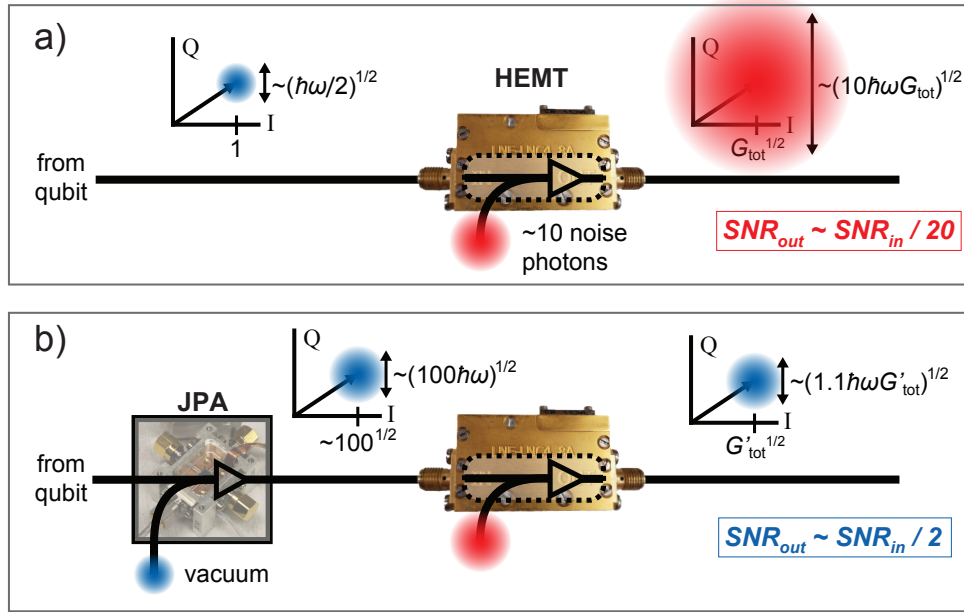
Figure 2.4: A comparison of SNR degradation due to a typical amplification chain (a) without and (b) with a JPA. A JPA can provide large power gain (≥ 20 dB) such that the ~ 10 noise photons typically added by the next amplification stage become negligible. An ideal JPA operating in phase-preserving mode adds only half a photon of noise, such that the total SNR degradation is only a factor of ~ 2 instead of a factor of ~ 20, reducing averaging times $\sim 10\mathrm{x}$. The same reasoning applies if the JPA is swapped for another near quantum-limited amplifier such as the Josephson Traveling Wave Parametric Amplifier (JTWPA). When it is only necessary to detect one electromagnetic quadrature, phase-sensitive amplification can recover the remaining factor of 2 such that $\mathrm{SNR_{out}} \approx \mathrm{SNR_{in}}$.

of frequency[4], increases with greater κ_{ext}. Larger bandwidth implies a faster response time of the JPA, allowing for shorter measurement pulses (typically one wants κ_{ext} of the JPA to be large compared to that of the readout resonator), for frequency multiplexed readout of multiple qubits, and for greater spectral separation of the JPA pump tone and the readout resonator(s). Increasing κ_{ext} can also increase the dynamic range of the JPA [60], or the signal power at which the amplifier response saturates. However, increasing κ_{ext} too much leads to device instability that can destroy the amplification process. When designing this style of lumped-element device, choosing C to give a quality factor of $Q \sim 10 - 15$ is usually a safe compromise between capability and stability. Recent experiments have shown that significantly greater bandwidth can be achieved with a modest increase in device complexity

---

[4]Strictly, the bandwidth is the FWHM of the curve $G(\omega) - 1$. For large gains, $G \approx G - 1$, so one can approximate the bandwidth as the maximum gain minus 3 dB, but when low gains are of interest, as in some squeezing experiments, the distinction can be significant.

using an appropriate impedance transforming circuit outside the JPA to modify the effective complex impedance Z [61, 62, 57].

It is sometimes desirable to keep κ_{ext} small, for example when the goal is to produce squeezed noise at one frequency but not at other nearby frequencies. A natural means of weakening the coupling to the transmission line is to introduce a capacitance C_{coup} (Fig. 2.2, green), increasing the effective impedance Z. (For $C_{\text{coup}} \ll C$, we have $\omega_0 \approx (L(C + C_{\text{coup}}))^{-1/2}$). However, reducing κ_{ext} has the side effect of decreasing dynamic range. To compensate for this effect, one can introduce a geometric inductance L_{geom} in series with L_{J}, reducing the voltage drop across the nonlinear elements and thus increasing the characteristic energy scale of the device. However, making L_{geom} too large also introduces the same instability as when κ_{ext} is too large. If we define the participation ratio $p_J = L_{\text{J}}/(L_{\text{J}} + L_{\text{geom}})$, a rough rule of thumb is to keep $Qp_J \gtrsim 5 - 10$ [63, 58]. This trend of instability is demonstrated by the rudimentary numerical simulations shown in Fig. 2.5. A simple way to estimate L_{geom} in a JPA design is to simulate the design with a variable lumped element inductance L_{J} in place of the SQUIDs for several values of L_{J}, then fit the results to the expression $\omega_0 = ((L_{\text{geom}} + L_{\text{J}})C)^{-1/2}$, modeling the geometric inductance as being in series with the SQUID inductance. This procedure can be performed efficiently using, for example, AWR's Microwave Office software, where the finite-element analysis need be performed only once and L_{J} can be subsequently varied instantly as a tunable parameter.

A few more subtleties should be considered before deliberately adding geometric inductance. Since tuning the JPA in frequency changes L_{J}, typically Qp_J can be optimized only over some range within the tunable band. Moreover, in the limit of large L_{geom}, tuning the JPA frequency requires making Φ_{app} very close to half a flux-quantum, which has produced instability in some devices, possibly due to the increased sensitivity to flux noise or to saturation of the JPA. Section 2.6 discusses an alternative method of increasing dynamic range using SQUID arrays.

Addition of a second port with mutual inductance to the JPA SQUID loop(s), as in Fig. 2.2, enables flux pumping of the JPA. The port shown uses shorted coplanar waveguide, but many line geometries are possible [52, 64, 65]. The flux pump is typically set to twice the JPA resonance frequency, advantageously keeping the pump spectrally separate from most experimental resonances and moreover making it possible to block the pump with a low pass filter[5]. This spectral separation comes at the cost of JPA tunability. In order for a meaningful amount of power to be transduced from the flux pump to the cavity mode via parametric modulation of ω_0, the modulation amplitude approximated as $\Phi_{\text{fp}} \frac{d\omega_0}{d\Phi_{\text{app}}}$ must be made on the order of κ, where Φ_{fp} is the amplitude of the flux put through the SQUID by the pump, and the derivative is computed using Eq. 2.1. Heating effects often constrain the achievable Φ_{fp}, even with fast pulsing of the pump and with light attenuation on the pump input line, so a

---

[5]Such filtration is often necessary after the JPA due to the large pump-powers and non-zero leakage of power from the pump port to the signal port. Without a filter or cancellation scheme, the transmitted pump can, for example, disrupt the amplification process in a broadband Josephson traveling wave parametric amplifier (JTWPA) downstream, or populate a higher mode of a 3D-transmon cavity. See the wiring diagrams in Appendix A.
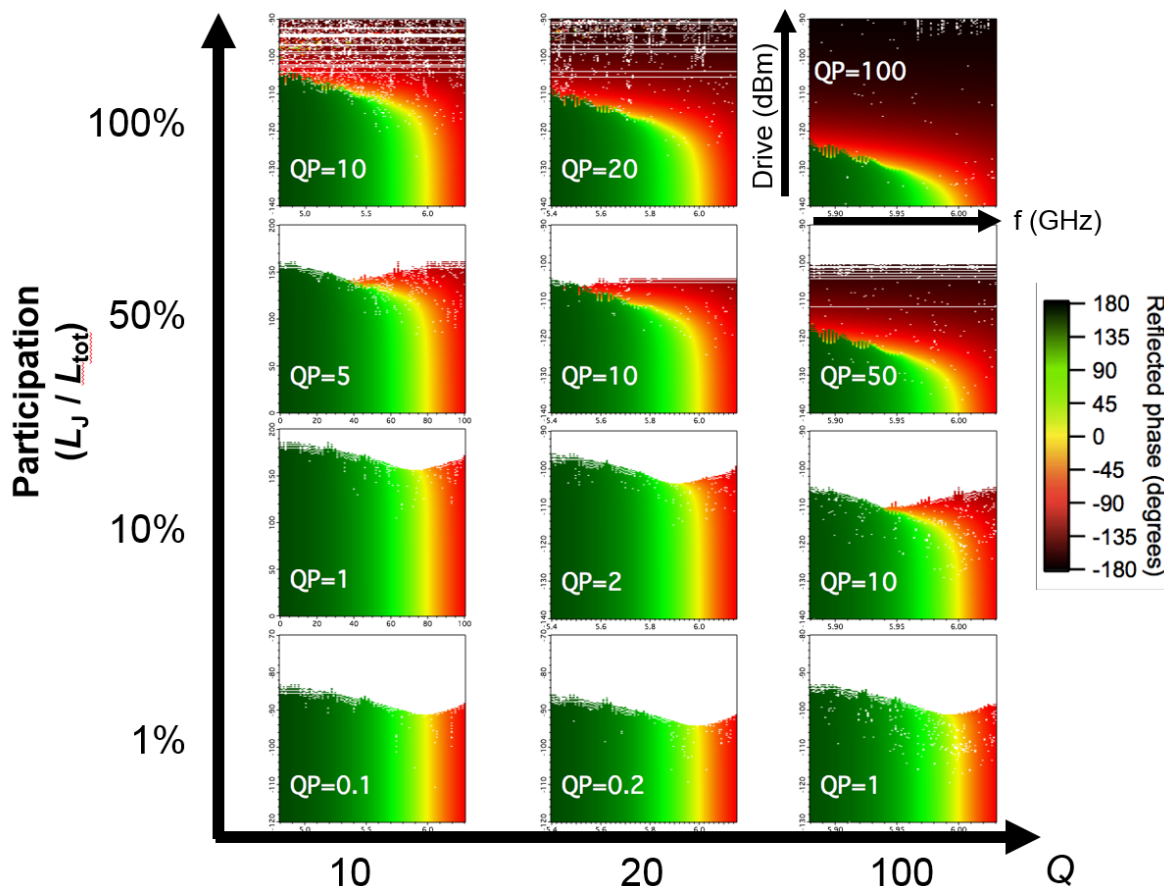
Figure 2.5: Numerical simulations indicating JPA stability at low junction participation. Each subplot corresponds to a simulated circuit with a particular value of p_J (macro vertical axis) and of Q (macro horizontal axis). Within each subplot, the color-scale indicates the phase accumulated by a microwave tone reflecting off the JPA with no other drives applied, as a function of the power (vertical axis, log scale) and frequency (horizontal axis) of that tone. At low powers (bottom region of a subplot), the JPA response is approximately linear, and a 360-degree phase-shift is accrued sweeping from far-below to far-above resonance, with resonance indicated in yellow. At higher drive powers, the JPA nonlinearity becomes significant, causing the resonance (yellow) to shift downwards in frequency and then bifurcate. This region of leftward-curvature also corresponds to the regime of parametric gain for a current-pumped JPA. As a crude proxy for unstable dynamics, settings for which the numerical simulator (Mathematica's NDSolve) raised a warning or error were colored white; as the value of Qp_J is lowered, the instability regime moves closer to, then obliterates the parametric-gain regime. Note that while the vertical axis extends for 50 dB on each subplot, the vertical range on each subplot has been shifted independently to include the gain and instability regimes.
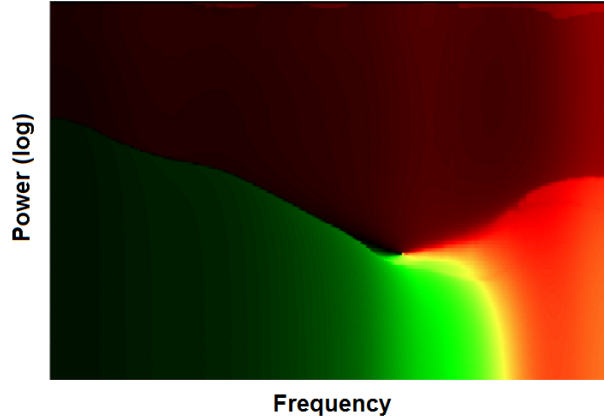
Figure 2.6: Measured phase response of a JPA with low Qp_J. Axes and color-scale are as in Fig. 2.5. Background features have been divided out by repeating measurements with the JPA tuned away. These data are incomplete, missing the values on the axes, but are provided as a qualitative example of the response of a JPA with a low value of Qp_J. Comparison with Fig. 2.5 suggests $Qp_J \sim 5$ for this device. Notably, no clear bifurcation regime appears, and an extra resonance feature extends upwards and to the right from the vicinity of the expected critical point. Compare to the clean behavior of the narrowband JPAs measured in Fig. 2.11. Despite these anomalies, this device could be pumped for over 20 dB gain with an estimated 12 dB of steady-state SNR improvement in a test setup. Other devices with significantly lower estimated values of Qp_J did not show gain, or exhibited limited gain.

sufficiently large static flux bias must be applied to transduce enough pump power to realize appreciable gain. For example, the maximum operating frequencies at which the squeezing devices used in this thesis could achieve useful gain were $\sim 100 - 200$ MHz below their $\Phi = 0$ frequencies. At the same time, the minimum operating frequency may be raised when the devices contain significant L_{geom} due to stability issues mentioned above. The flux-pumped devices in this thesis were thus designed with very specific operating frequencies in mind.

Even in current-pumped devices, where tunability is less constrained, tuning by an octave requires, generously assuming $L_{\mathrm{geom}} \ll L_{\mathrm{J}}(\Phi_{\mathrm{app}})$, decreasing $I_c(\Phi_{\mathrm{app}})$ by a factor of 4, expected to reduce the saturation power of the device by a factor of roughly ~ 16. Thus increasing saturation power can also increase the usable tunable range for some applications.

2.4 Examples of JPA circuits

Here we present several JPA designs we developed for projects unrelated to the published works covered in later chapters.

Three JPAs designed to operate in the 4-8 GHz band (C-band) commonly used for circuit QED experiments are shown in Fig. 2.7. The circuit in the upper-left panel is a single-
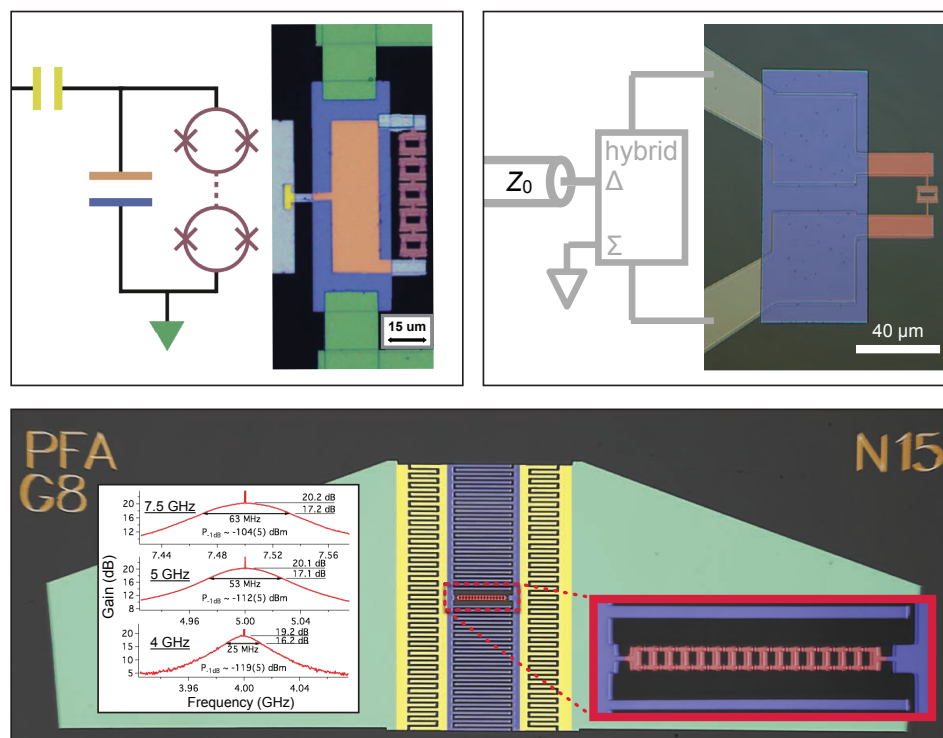
Figure 2.7: False-colored photomicrographs of three C-band (4-8 GHz) JPAs showcasing different design possibilities.

ended JPA. The schematic is coded to match the false-coloring of the photomicrograph. As usual we have a nonlinear LC resonator, here consisting of a parallel plate capacitor (blue and orange rectangles) in parallel with a series array of SQUIDs (red) providing Josephson inductance L_J. The ~ 3.3 pF capacitor consists of two layers of aluminum sandwiching 16 nm of evaporated alumina (aluminum oxide) with an effective dielectric constant of ≈ 5.4 inferred from the empirical specific capacitance. The Josephson junctions of the SQUIDs were deposited by standard resist-bridge double-angle evaporation techniques, such that each SQUID has a critical current of approximately 5 μA. Here all features were defined with electron-beam lithography, and all materials deposited with electron-beam evaporation. The upper plate of the capacitor is connected to ground and to one end of the SQUID array using additional aluminum rectangles deposited separately after ion milling to ensure good electrical connectivity. This device is unusual in that it was intentionally made narrowband by introducing a coupling capacitor (yellow) between the resonator and transmission line. In hindsight, this design employing a coupling capacitor would benefit from addition of geometric meander inductance to increase dynamic range by bringing Qp_J closer to $\sim 5-10$.

The circuit in the upper-right panel has a differential geometry, and is connected to the

transmission line via a microwave hybrid that rejects common-mode or ground noise. In the device shown, the capacitor is again an alumina parallel plate capacitor, though here for simplicity of fabrication the capacitance consists of two capacitors in series.

The bottom panel in Fig. 2.7 shows a JPA employing an interdigitated finger capacitor (IDC) instead of a parallel plate capacitor, which reduces loss and simplifies the fabrication process from three or four steps (1: alignment marks, 2: SQUIDs and bottom of capacitor, 3: dielectric and top of capacitor, 4: ion milling and shorts to connect to top of capacitor if needed) to one step (1: make the JPA). We necessarily increase L_{geom} as we make the capacitor larger; from finite-element simulations, we estimate that we cannot make C larger than ~ 0.5 pF without making L_{geom} too large for stable amplifier performance. This is significantly smaller than the value of C we use in standard parallel plate designs, which if uncorrected will change ω_0 and Q from their desired values. To restore $Q = \omega_0 C Z$, we introduce coupling capacitors (yellow) to increase the effective value of Z. To restore ω_0, we increase the total inductance, achieved here with a series array of 15 SQUIDs. Using many SQUIDs also increases the amplifier saturation power as discussed below. This device was cooled once and demonstrated excellent bandwidth and compression powers, as indicated in the inset gain profiles at three operating frequencies. However, on subsequent cooldowns in other experimental setups the device performed poorly for reasons not understood, providing limited gain and with reduced bandwidth. While it is not unheard of for devices to fail in between cooldowns, further study would be needed to determine if this failure was a coincidental event or due to some inherent vulnerability of the design, perhaps related to inhomogeneous aging of the junctions in the array while exposed to atmosphere or due to a different magnetic environment. We can say with more confidence that devices with only ~ 5 SQUIDs, such as that in the upper left panel, showed consistent performance across multiple cooldowns.

Figure 2.8 shows two JPAs developed for projects not involving superconducting qubits. The Axion Dark Matter Experiment (ADMX) based at the University of Washington hopes to detect microwave radiation produced by decays of the hypothesized axion dark matter particle. To do so, they have developed a tunable microwave cavity which they place in a large dc magnetic field. The magnetic field is predicted to stimulate the decay of axions into microwave photons, and this process is enhanced when the cavity mode is resonant with the energy of the emitted photon. However, the average power due to this process is in the ballpark of -200 dBm, such that detection requires very long averaging times. Thus superconducting amplifiers are poised to greatly facilitate this search. Towards this end, we developed and characterized single-ended JPAs operating over the 1-2 GHz band of primary interest to ADMX. The amplifier and example gain profiles are shown at left in Fig. 2.8. In our measurement setup, turning on the JPA produced 10-13 dB of SNR improvement at room temperature for small signals (the relevant limit for axion radiation power). The device was delivered to ADMX.

We used a similar design to develop an even lower frequency JPA for use in measurements of quantum dot qubits. The device is shown at right in Fig. 2.8. This device operated a full order of magnitude below the usual 4-8 GHz band of circuit QED, so some reduction in the
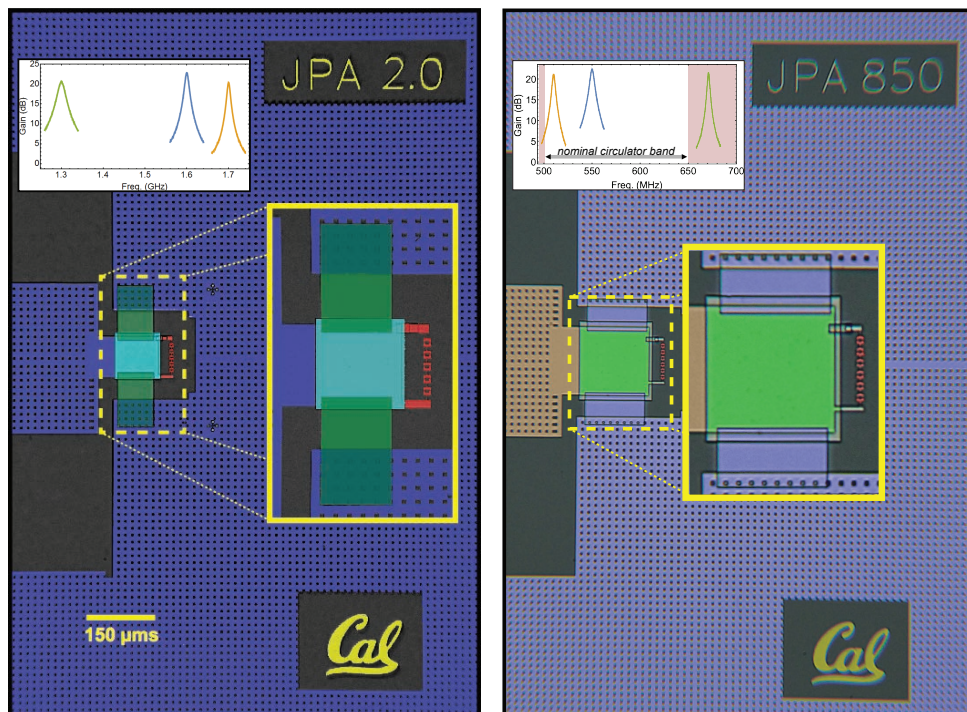
Figure 2.8: False-colored photomicrographs of two JPAs, one developed to work over the
1-2 GHz band (left) for ADMX, the other developed for quantum-dot state readout below 1
GHz. Inset plots (upper left) show gain profiles acquired at several operating frequencies to
demonstrate tunability.

energy scale of the device and bandwidth were expected *ab initio*. Multiple SQUIDs were
used to try to increase the dynamic range of the device as discussed later in this chapter,
but even so the input P_{1dB} of a measured device was estimated to be only ~ -140 dBm. For
small signals we still observed over 13 dB SNR improvement in our test setup. Increasing the
signal size resulted in compression of the JPA gain but still appreciable SNR improvement.

We suggest a modification on these designs to anyone looking to imitate them. As shown,
a complete loop of superconducting aluminum encircles the array of SQUIDs. Starting in
the top capacitor layer, the loop goes up the plane of the page to ground (purple), down to
the right of the SQUIDs, then back up to the top capacitor pad. While evidently tolerable
for aluminum devices, similar superconducting loops in niobium JPAs (not shown) provided
sufficient magnetic shielding to prevent the off-chip coil from passing flux through the SQUID
loops, preventing tunability. Using an ion mill to create a break in the ground plane on one
niobium JPA solved this problem: before ion milling the JPA did not respond to applied
flux, and after ion milling the JPA tuned readily. This problem does not obviously manifest
in aluminum devices, but in all recent designs we leave a gap in the ground plane as a

precaution against flux-blocking ground loops.

2.5 JPA cryopackaging

The fabricated JPA chip needs to be packaged in some kind of housing that connects the JPA to one or more microwave lines while isolating the circuit from other, disruptive environmental elements. The chip is typically connected to a microwave circuitboard using aluminum wirebonds, and the circuitboard is connected via an SMA adapter to the coaxial microwave line. We used circuitboard substrate TMM6 from Rogers Corporation for the thermal stability of its dielectric material, though future designs may benefit from a lower loss substrate[6]. As usual with microwave design, shorter trace lengths are preferable, though the minimum board size is sometimes limited by wirebonding accessibility. The chip is affixed to oxygen-free high conductivity (OFHC) copper using a thin layer of GE varnish, chosen for its desirable mechanical and thermal properties at cryogenic temperatures. A small pedestal in the OFHC copper bracket keeps the top surface of the chip approximately coplanar with that of the circuit board to minimize wirebond lengths. The chip is positioned such that the JPA SQUID loops are approximately centered above a superconducting coil to allow for application of a static flux-bias (Φ_{dc}). Coil currents of 1 to 10 mA are typical, with up to at least ~ 50 mA possible with no indication of resistive heating. Shielding from other environmental magnetic fields, such as that of the Earth or of nearby microwave circulators, is achieved by enclosing the circuit board and copper bracket within an aluminum box. To ensure that no enviromental magnetic flux is trapped as the aluminum device and box are cooled through their critical transition temperature (1K), the aluminum box is in turn mounted inside of a cryoperm layer which provides magnetic shielding for $T \geq 1$K. Nonmagnetic or less-magnetic materials were used inside the magnetic shields (for screws, connectors, etc) when convenient, though good JPA performance was commonly observed even when e.g. stainless-steel SMA connectors were used. As superconductors have low thermal conductivity, an OFHC copper strap is routed through a small, high aspect-ratio hole in each box to enable thermalization of the chip and circuitboard to the cold stage of the dilution refrigerator.

Figure 2.9 shows several examples of JPA housing. The top photo is housing for a JPA requiring a differential excitation ("double ended"), while the bottom two photos are different views of housing for a JPA requiring an excitation with respect to ground ("single ended"). The differential design isolates the JPA from electrical ground, improving device stability in the presence of an imperfect or noisy ground inside the dilution refrigerator[7]. The downside of using a differential design is the need for a 180° hybrid (or some equivalent

---

[6]When choosing a circuitboard dielectric, it may make sense to choose a dielectric constant near that of the chip itself (~ 10 for silicon), but mind that greater dielectrics tend to lower the frequency of the first parasitic environmental modes. Problems with such modes can often be solved using vias and finite-element simulation of the board and enclosure as necessary.

[7]Grounding problems sufficient to disrupt superconducting circuits arise easily and can be very difficult to track down. A contributing factor seems to be the grounding scheme of the widely used LNF HEMT
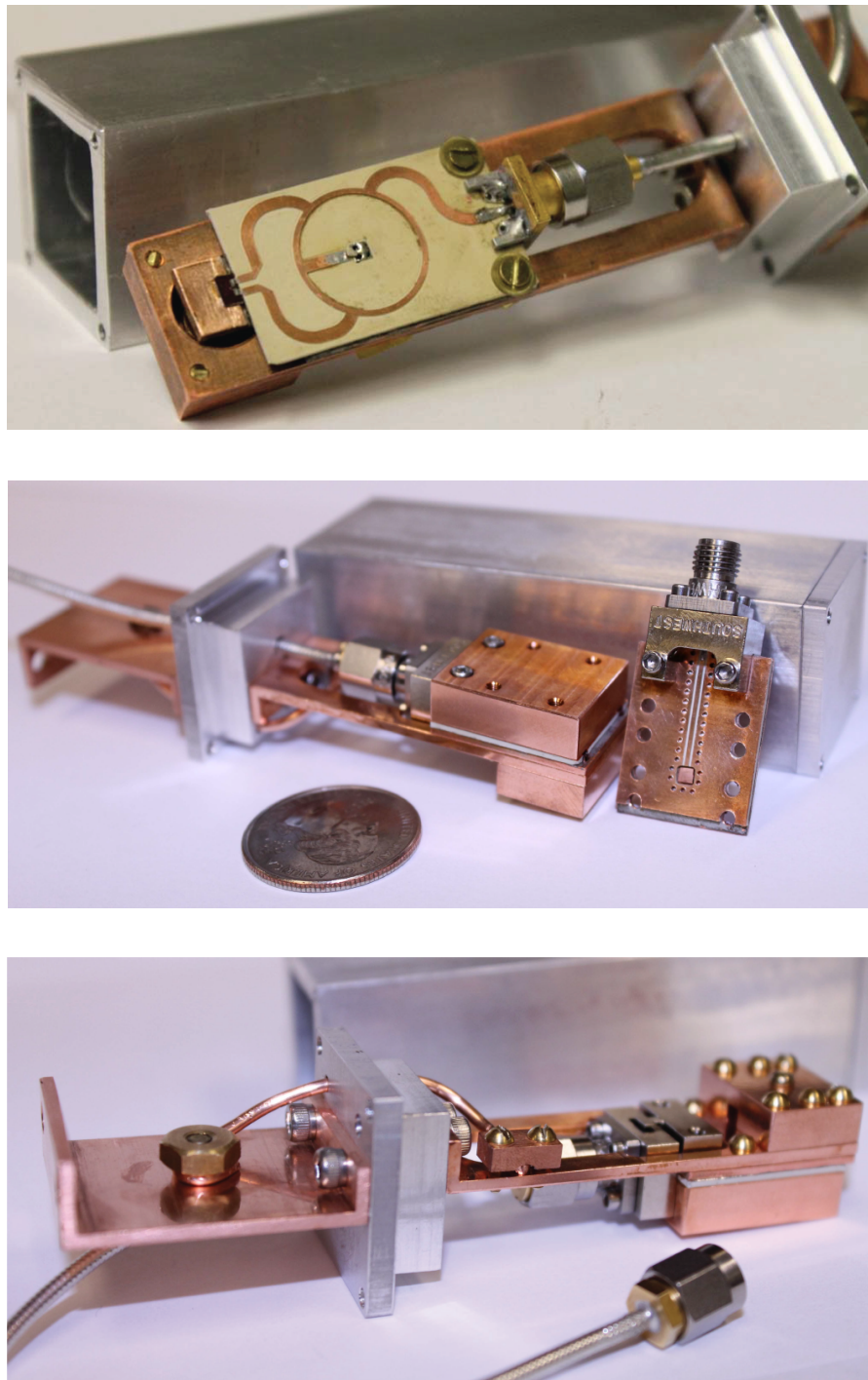
Figure 2.9: Examples of JPA cryopackaging.
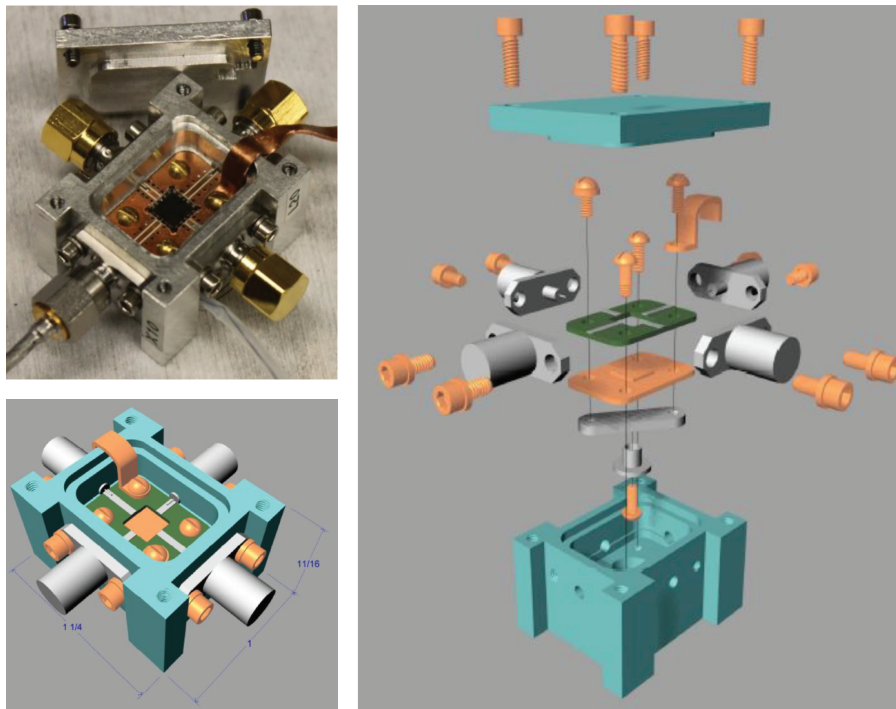
Figure 2.10: A more compact JPA cryopackage, also produced in a 1" cube single-port version not shown. Design credit to D. Wright and R. Lolowang.

balun) to convert between common mode and differential excitations; these circuit boards take up space, introduces some loss, and can constrain the frequency band over which the JPA functions optimally. Single-ended designs eliminate the need for a hybrid, allowing for more compact cryopackages, as in Fig. 2.10 which allows for testing 4 JPAs patterned on a chip, or for testing two JPAs each with a flux-pump connection. The larger aluminum boxes in Fig. 2.9 suffer from sparse but inconvenient electromagnetic box modes; these were suppressed by lining the box with RF absorber, but using a more compact geometry as in Fig. 2.10 is a preferable solution when possible.

amplifiers, as the amplifier chassis is internally connected to the ground of the power source for the device, often a wall outlet, such that noise on the outlet ground or picked up by the ground loop contaminates the otherwise clean fridge ground. A workaround is to use an isolation transformer in a configuration isolating the wall ground from the fridge ground. This technique enabled the use of a JTWPA (highly sensitive to ground noise) in a fridge where it previously would not provide gain. Another plausible approach is to electrically isolate the chassis of the HEMT from the fridge using GE-varnish coated cigarette paper, nylon screws, and inner/outer dc blocks.

2.6 Multi-SQUID JPAs

Beyond optimizing the value of Qp_J, further increases in dynamic range, roughly the maximum signal power the JPA can amplify, are possible by utilizing SQUID arrays [59]. We quantify dynamic range in terms of the compression power $P_{\text{-1dB}}$, here defined as the input signal power at which the JPA gain decreases 1 dB from its small-signal value. In this section we motivate why using multiple SQUIDs is expected to increase $P_{\text{-1dB}}$, then present an experimental comparison of several devices characterizing this enhancement.

One generic model for amplifier compression is pump-depletion. In typical JPA operation, a large pump tone biases the JPA into a nonlinear regime in which gain occurs. The addition of a much smaller signal tone perturbs these nonlinear dynamics such that power is transferred from the pump to the signal as desired. Because the pump is so much larger, the overall JPA dynamics, and thus also the gain, are approximately independent of the signal. This ideal small-signal condition is sometimes referred to as the stiff-pump regime, characterized by $GP_{\text{sig}} \ll P_{\text{pump}}$. As the size of the signal is increased, the perturbative approximation breaks down, and a non-negligible amount of power must be drained from the pump in order to amplify the signal. This depletion of the pump power suppresses the nonlinear dynamics providing gain, and compression of the output field occurs. See e.g. [54] for a recent experimental investigation of the effect of pump-depletion on JPA squeezing.

For definiteness we now restrict our discussion to the case of a current-pumped JPA. The pump-depletion model suggests that increasing the available pump power should increase $P_{\text{-1dB}}$. However, for a given circuit only a narrow range of pump powers can be used; gain occurs at pump powers slightly below a critical bifurcation power P_{bif}, and above P_{bif} the JPA response stops being single-valued and no parametric gain occurs. To realize greater dynamic range, we can modify the JPA circuit to increase P_{bif}. As the energy scale of this nonlinear process is proportional to the square of the SQUID critical current I_{SQUID}^2, replacing the single SQUID of critical current $I_{\text{SQUID}} = I_c$ by a series array of N SQUIDs each of critical current $I_{\text{SQUID}} = NI_c$ leaves the cumulative low-power inductance L_{J} unchanged but increases P_{bif} and thus $P_{\text{-1dB}}$.

To investigate this scaling experimentally, we fabricated JPAs with varying numbers of SQUIDs $N = 1$, 2, and 5 to compare their performance. An $N = 5$ device is shown in the upper-left panel of Fig. 2.7. The widths of the Josephson junctions in each device were scaled by N, such that the total Josephson inductance $L_{\text{J}} \propto (NI_{\text{SQUID}})^{-1} = (N\frac{2I_0}{N})^{-1} = (2I_0)^{-1}$ was kept approximately constant across the devices, where I_0 is the critical current of a junction in the $N = 1$ device. Geometric inductance was kept approximately constant across all arrays by including straight sections of electrical leads as placeholders in devices of lower N; from finite element simulations we estimate the geometric inductances to be 82, 79, and 70 pH for the 1, 2, and 5 SQUID JPAs. An input coupling capacitor was used to reduce the JPA bandwidth ($Q_{\text{ext}} \approx 150$) to reduce deviations from theoretical behavior produced by slight impedance variations of connecting microwave circuitry. We measured the devices on three consecutive cooldowns with the same cryopackaging, cables, and microwave test instruments.
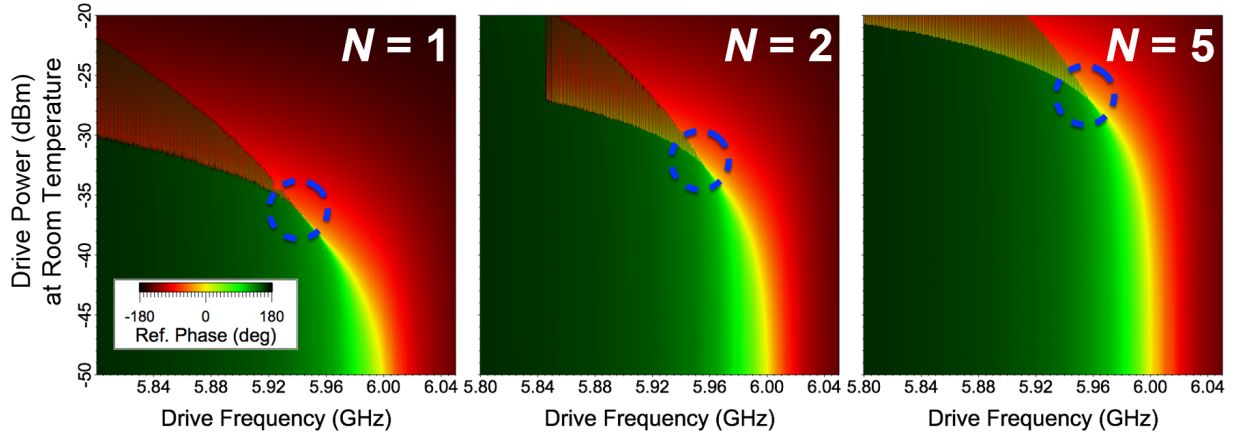
Figure 2.11: Measured phase responses of JPAs with 1, 2, and 5 SQUIDs as a function of drive frequency and power. The color scale encodes the phase of a single tone reflected from the device. Each JPA has been flux-tuned to resonate at 6 GHz for low drive powers. As the power is increased, the Kerr nonlinearity of the device becomes significant and the resonance shifts downwards in frequency and narrows. Above a critical power P_{bif} (circled) the response becomes bistable. The bistable regime appears as the striped region in the plot, produced by alternately sweeping the power up and down to latch into the low- and high-amplitude responses. A resonant drive applied to the JPA (i.e. somewhere on the yellow stripe, approximately) with a power slightly below P_{bif} acts as a pump producing parametric amplification. Comparing the plots, we see P_{bif} increases with the number of SQUIDs, N.

Figure 2.11 shows the response of each device to a single tone as a function of frequency and power. At low drive powers, the oscillator's response is that of a linear resonator. At greater drive powers, the JPA nonlinearity becomes significant, causing the resonance to narrow and to shift downward in frequency. At a critical power set by this nonlinearity, the JPA response becomes bistable; interleaving upward and downward fixed-frequency power sweeps allows the bistable regime to be seen as a striped section in each data plot. We repeated these measurements to determine P_{bif} for three bias frequencies, producing Fig. 2.13. These data show a clear increase in bifurcation power as the number of SQUIDs is increased. Relative to the $N = 1$ bifurcation power, the $N = 2$ and $N = 5$ bifurcations occurred at powers on average 4 dB and 9 dB higher, respectively (averaged on a linear scale). These increases fall short of the expected N^2 scaling, but still imply a significant increase in available pump power in the paramp regime.

To probe $P_{\text{-1dB}}$ directly, a signal was coupled into the JPA along with the pump to measure amplifier saturation at several JPA operating points from 4.8 to 6.4 GHz. The signal was detuned from the pump by an amount much smaller than the bandwidth of the JPA at each point (detuning ~ 50 kHz). Figure 2.13 plots JPA gain as a function of signal power at
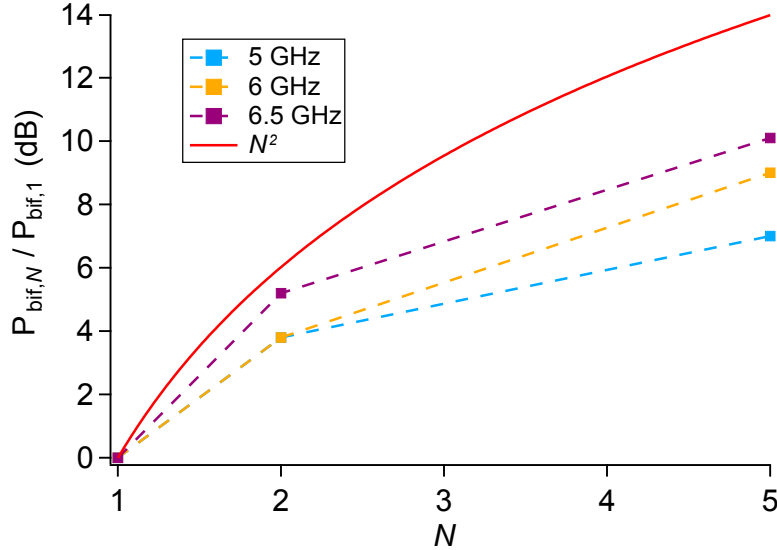
Figure 2.12: Relative critical powers at which bifurcation occurs in JPAs of 1, 2, and 5
SQUIDs. Here all devices are current pumped for gain at 6 GHz.

6 GHz; as the signal power is increased, the amplifier saturates and the gain rolls off. We
identify the 1-dB compression point as the incident signal power at which the amplifier gain
drops 1 dB from its small-signal value. The data from the 2 and 5 SQUID devices exhibit
compression powers several dB greater than that of the single-SQUID device. These values
are comparable to the increases in the respective devices' bifurcation powers, consistent with
the expectation that the diluted nonlinearity increases dynamic range by extending the upper
limit of the stiff-pump approximation.

While the sub-N^2 scaling was not fully understood—perhaps relating to junction inho-
mogeneity, inhomogeneity of magnetic flux coupling to the SQUIDs, or to dielectric losses in
the alumina capacitors—these measurements still confirmed the expectation that increasing
N increases $P_{\text{-1dB}}$, motivating our development of multi-SQUID JPAs such as those in Figs.
2.7 and 2.8. This approach to weakening the JPA nonlinearity has also been theoretically
predicted to improve the ability of the JPA to produce electromagnetic squeezing [2], and
indeed the greatest squeezing produced to date was generated in a "Josephson parametric
dimer" consisting of two coupled JPAs each with $N = 30$ [28]. The generation of squeezed
microwaves is further discussed in the next chapter.
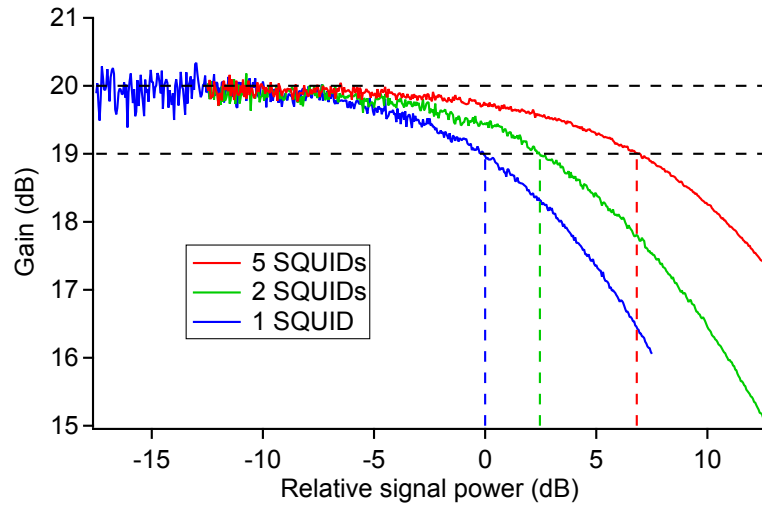
Figure 2.13: Gain as a function of relative incident signal power for JPAs with 1, 2, and 5 SQUIDs operating at 6 GHz. The horizontal axis indicates input signal power normalized to $P_{\text{-1dB}}$ of the $N = 1$ device.
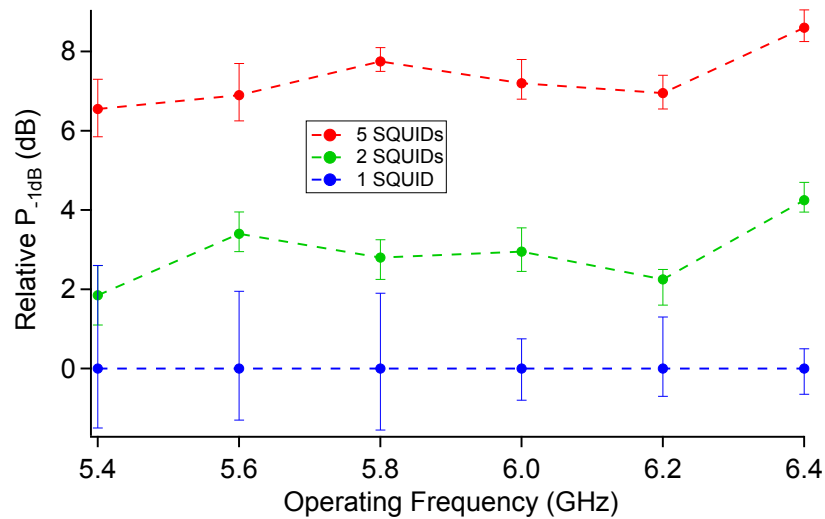
Figure 2.14: Relative compression powers of multi-SQUID JPAs as a function of frequency.

Chapter 3

Quantum Amplification and Squeezing with the JPA

3.1 Electromagnetic squeezed states

We begin with a discussion of what electromagnetic squeezed states are and the common notations for describing them quantitatively, then discuss the quantum dynamics by which a parametric amplifier produces squeezing. We focus on the case, relevant to the experiments in later chapters, of squeezed states of a single-mode of the electromagnetic field, though much of the discussion applies to the two-mode case as well with modest modification. A classical electromagnetic field mode oscillating sinusoidally at ω can be represented as an arrow in phase space, or a phasor. In the "lab frame" or dc-frame, the phasor rotates counter-clockwise with angular velocity ω. Typically we transform to the frame co-rotating at ω such that the arrow is stationary, with static quadrature components sometimes referred to as X_1 and X_2 (alternative names include I and Q, or X and P). Quantum mechanics stipulates that these two conjugate variables cannot both possess exact values simultaneously; there must be some uncertainty, or noise, satisfying the Heisenberg uncertainty relation $\sigma_{X_1}\sigma_{X_2} \geq 1/4$. For the common case of a Gaussian noise distribution, we can represent the noise by an ellipse in phase space as in Fig. 3.1. The projection of the ellipse onto X_1 or X_2 by integrating over the orthogonal axis describes the standard deviation in that quadrature, and the orientation of the ellipse is determined by the covariance. More generally, we can uniquely represent any state of the light field by its complete Wigner function[1] in phase space; drawing a contour on a Gaussian Wigner function at the 1σ level produces an ellipse. For example, the vacuum-state Wigner function is a circular (isotropic) bivariate Gaussian in phase space, defining the circular contour in Fig. 3.1(a) with variance $1/4$ in every direction.

---

[1]The Wigner function is similar to the classical joint probability distribution of two variables, with the additional twist that the Wigner function can have negative values at some regions in phase space. These negative values never lead to negative probabilities for possible measurement outcomes, as the projection of the Wigner function onto any phase-space axis (by integrating, or marginalizing, over the orthogonal axis)

(a) X_2

$2\sigma = 1$

(b) X_2

$2\sigma(\varphi) = \sqrt{1+2(N+M)}$

φ

X_1

$2\sigma(\varphi+\pi/2) = \sqrt{1+2(N-M)}$

(c) X_2

Φ

φ_c

X_1
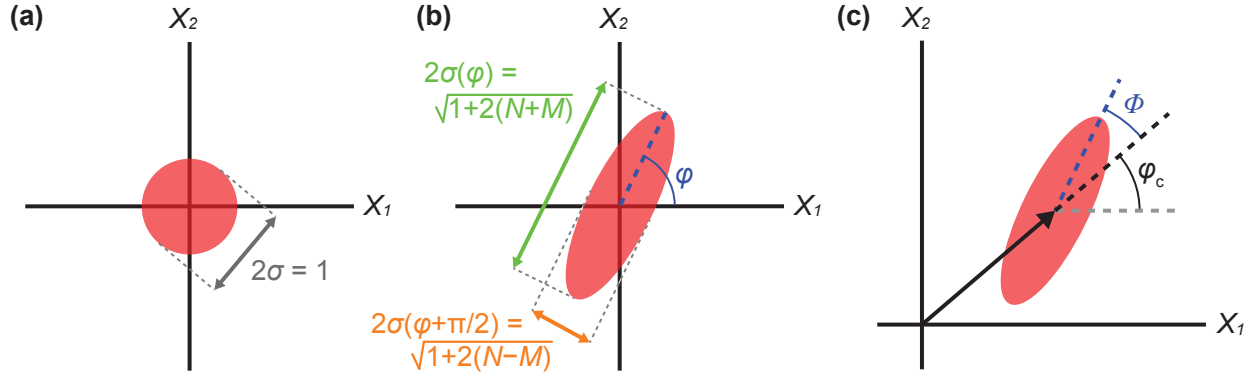
Figure 3.1: Phase-space representations of squeezed states. Shaded ellipses represent contours of the Gaussian Wigner functions drawn at one standard deviation. (a) The electromagnetic vacuum appears as a circle in phase space normalized to have diameter 1, implying a variance $\sigma^2 = 1/4$. (b) Squeezed vacuum has an increased variance along the angle φ, $\sigma(\varphi)^2 = (1/2 + N + M)/2$, and reduced variance along the orthogonal angle, $\sigma(\varphi + \pi/2)^2 = (1/2 + N - M)/2$. The variance along an arbitrary axis is given by $\sigma(\theta)^2 = (1/2 + N + M\cos(2\theta - 2\varphi))/2$, geometrically the projection (marginalization) of the distribution onto that axis. (c) Squeezed vacuum can be combined with a coherent state to make a displaced squeezed state.

The single defining feature of a squeezed state is a variance along one axis that is less than this vacuum variance, $\sigma_-^2 < 1/4$, as in Fig. 3.1(b). Thus a squeezed state need not be Gaussian, nor explicitly contain pairs of photons[56], though in practice squeezed states often meet both these conditions. The Heisenberg uncertainty relation implies that the noise in the orthogonal quadrature must increase proportionally, $\sigma_+ \geq \frac{1/4}{\sigma_-}$. For an ideal squeezed state, the equality is saturated, and we can characterize both quadratures by a single squeezing parameter r, with $\sigma_\pm = (1/2)e^{\pm r}$, such that $r = 0$ for no squeezing.

Experimentally, transmission losses often result in squeezed states that are still Gaussian but for which the above equality is not saturated, i.e. $\sigma_+\sigma_- > 1/4$. Such states contain thermal (classical) noise in addition to the intrinsic quantum noise, and thus are classified as mixed states rather than pure states. Since σ_+, σ_- are independent for this class of states, we need two squeezing parameters to define a state. A convenient choice is to use N and M, defined such that $\sigma_\pm^2 = (1/2 + N \pm M)/2$, similar to the conventions in [66, 67]. Graphically, increasing N increases the size of the ellipse in all directions, while increasing M increases the asymmetry of the ellipse. Heuristically, we consider N to be the effective number of noise photons, while M is loosely akin to the effective number of photons that are each correlated with another photon such that their noise fluctuations tend to cancel in

---

will always be positive valued.

one quadrature; a more rigorous definition appears below. For the case of ideal squeezing saturating the Heisenberg equality, one obtains $M = \sqrt{N(N+1)}$. This parameterization is convenient in part because transmission of a squeezed state through some channel with power loss $1 - \epsilon$, where $\epsilon = 1$ implies no loss, simply changes the squeezed state by the mapping $(N, M) \to (\epsilon N, \epsilon M)$. This mapping agrees with our heuristic picture, as we expect all subsets of the photon population to experience the same attenuation regardless of whether they possess photon-photon correlations.
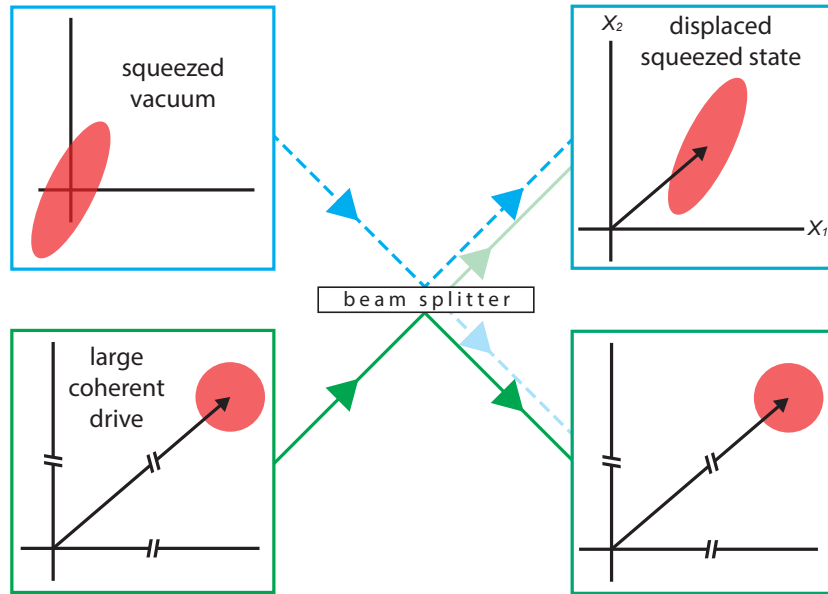
Figure 3.2: Creation of a displaced squeezed state. Here the beam splitter is assumed to be highly reflective. The two modes (blue/dashed and green/solid) are taken to be spatially separated but otherwise identical. For simplicity we assume zero phase shifts. In the microwave regime, one might use a directional coupler instead of a beam splitter. Later chapters discuss experiments where intra-cavity squeezed vacuum is displaced via a coherent drive applied to a weakly-coupled cavity port.

We introduce a third parameter, φ, to specify the orientation of the squeezing ellipse in phase space with respect to X_1 and X_2 (Fig. 3.1(b)). This angle specifies the correlation of the noise in X_1 and X_2 such that the variance along an arbitrary phase-space axis making an angle θ with X_1 is $\sigma(\theta)^2 = (1/2 + N + M\cos(2\theta - 2\varphi))/2$.

Finally, we generalize to the case of a displaced squeezed state as depicted in Fig. 3.1(c). Such states can be readily produced by using an unequal beam-splitter or equivalent to combine a coherent state (sinusoidal drive) and a squeezed state. Fig. 3.2 diagrams this process. If the beam splitter is made very reflective and the coherent drive amplitude made

proportionally very large, a finite displacement is coupled into the mode containing squeezed vacuum, yet vanishingly little squeezing leaks out from this mode ($N, M \to \epsilon N, \epsilon M$ and $\epsilon \approx 1$). Since the displacement has an amplitude and phase, we need a total of 5 real parameters to specify a displaced squeezed state: N, M, Φ, α, and φ_c, where α and φ_c specify the amplitude and phase of the displacement and where we have chosen to use $\Phi = \varphi - \varphi_c$ instead of φ to specify the orientation of the squeezing ellipse (see Fig. 3.1(c)). With this definition of Φ, the cases $\Phi = 0$ and $\Phi = \pi/2$ respectively correspond to squeezing of phase noise and amplitude noise. In Chapter 4 we measure how atomic fluorescence is modified under phase- or amplitude-squeezing of the drive.

3.2 Quantum derivation of JPA dynamics

The presentation here largely follows that in Ref. [2] (a similar derivation also appears in Ref. [68]), though for simplicity we will drop higher-order corrections considered in that work, restrict ourselves to the immediately relevant case of squeezing with a flux-pumped JPA, and sprinkle the discussion with additional pedagogical commentary. Many other excellent descriptions of JPA dynamics exist in the literature, such as [58, 69, 60]. In considering the JPA, we will encounter quantum limits on noise performance that in fact generalize to all amplifiers, as derived in [70, 71].

A basic JPA circuit can be described by the Hamiltonian

$$\hat{H}_{\mathrm{JPA}} = \frac{\hat{Q}^2}{2C} - E_J \cos(\frac{\hat{\phi}}{\varphi_0}), \tag{3.1}$$

where C is the capacitance, $E_J = \varphi_0 I_c$ the Josephson energy, $\varphi_0 = \hbar/2e$ the reduced flux quantum, $\hat{Q} \propto (\hat{a} + \hat{a}^\dagger)$ the charge operator, and $\hat{\phi} \propto i(\hat{a} - \hat{a}^\dagger)$ the generalized flux operator, with $[\hat{\phi}, \hat{Q}] = i\hbar$. Applying magnetic flux $\Phi_{\mathrm{app}} = \Phi_{\mathrm{dc}} + \Phi_{\mathrm{fp}} = 2\varphi_0(F + \delta f \cos \omega_p t)$ through the squid loop modulates the Josephson energy according to

$$E_J \to E_J \cos(\frac{\Phi_{\mathrm{app}}}{2\varphi_0}) = E_J \cos(F + \delta f \cos \omega_p t). \tag{3.2}$$

If we choose the pump frequency to be $\omega_p \approx 2\omega_0$, this modulation of E_J ultimately produces parametric amplification and squeezing. Now we are going to take a battery of sensible approximations to make the squeezing operator become manifest. Fourier expansion of this expression for E_J gives

$$E_J \cos(F + \delta f \cos \omega_p t) = \sum_n E_J^{(n)} \cos(n \omega_p t) \tag{3.3}$$

where the coefficients $E_J^{(n)}$ are found via the Jacobi-Anger formula. These coefficients include Bessel functions which can in turn be truncated to leading order in δf with the assumption that $\delta f \ll 1$ (i.e. that the modulation depth is small). After additionally taking the rotating

wave approximation (in the phase-space frame rotating at $\omega_p/2$) and setting $\hbar \to 1$, one can rewrite the JPA Hamiltonian as

$$\hat{H}_{\mathrm{JPA}} = \Delta_{\mathrm{f}}\hat{a}^{\dagger}\hat{a} + \frac{i\lambda}{2}(\hat{a}^{\dagger 2} + \hat{a}^2) + \hat{O}(\hat{a}^4), \qquad (3.4)$$

where we have $\Delta_{\mathrm{f}} \approx \omega_0 - \omega_p/2$ and $\lambda = \frac{E_J^{(1)}\Phi_{\mathrm{zpf}}^2}{2} \approx \frac{-E_j\delta f \sin(F)e^2}{\omega_0 C}$. Here we have chosen λ to be real which effectively fixes the phase of the JPA pump tone; a more general expression would allow λ to be complex [2]. If we choose to pump resonantly, $\Delta_{\mathrm{f}} = 0$, then our chosen phase-space frame co-rotates with the cavity field per the Hamiltonian

$$\hat{H}_{\mathrm{JPA}} = \frac{i\lambda}{2}(\hat{a}^{\dagger 2} + \hat{a}^2) + \hat{O}(\hat{a}^4). \qquad (3.5)$$

Thus when the flux-pump is off ($\lambda = 0$), for example, the cavity Wigner function appears stationary. The $\hat{a}^{\dagger 2}$ term indicates that turning on the flux-pump produces pairs of photons at the cavity mode, so we conclude the dynamics include a type of three-wave mixing in which pump photons are being downconverted into pairs of cavity photons. In fact, this form of Hamiltonian is characteristic of almost all (perhaps all) parametric amplifiers, such that the remaining leading-order discussion applies to all pumping schemes and in part even to optical devices. We can identify Eq. 3.5 as a generator of the standard single-mode squeezing operator,

$$S(r, \varphi) = \exp\left(\frac{r}{2}(e^{-i\varphi}\hat{a}^{\dagger 2} + e^{i\varphi}\hat{a}^2)\right). \qquad (3.6)$$

Naively exponentiating Eq. 3.5 gives a time evolution operator equal to a squeezing operator with $r = \lambda t$. If Eq. 3.5 were the whole story, we might infer that turning on the pump even a tiny amount would continuously cause exponential squeezing and amplification of noise power in the two field quadratures, respectively, at a rate λ, causing the mean photon number in the JPA to grow unbounded until some other higher-order nonlinear effect became significant and stopped the process. In reality this runaway behavior does not occur for arbitrarily small λ because of dissipation out the JPA port.

We now account for this decay of energy out of the JPA into a transmission line at rate κ. (Here we assume no dielectric or radiative loss occurs inside the JPA, such that $\kappa_{\mathrm{ext}} = \kappa$ and $\kappa_{\mathrm{int}} = 0$). This connection to the transmission line also implies the coupling of the incoming field, often unsqueezed vacuum noise, into the cavity at the same rate. The equation of motion is thus

$$\dot{\hat{a}} = i\left[\hat{H}_{\mathrm{JPA}}, \hat{a}\right] - \frac{\kappa}{2}\hat{a} + \sqrt{\kappa}\hat{a}_{\mathrm{in}} \qquad (3.7)$$

subject to the input-output boundary condition $\sqrt{\kappa}\hat{a} = \hat{a}_{\mathrm{in}} + \hat{a}_{\mathrm{out}}$, where as usual the presence of $\sqrt{\kappa}$ makes sense given that the units of $\hat{a}$ are related to $\sqrt{\mathrm{energy}}$, while those of $\hat{a}_{\mathrm{in/out}}$ are related to $\sqrt{\mathrm{power}}$. Evaluating the commutator gives

$$\dot{\hat{a}} = -i\lambda\hat{a}^{\dagger} - \frac{\kappa}{2}\hat{a} + \sqrt{\kappa}\hat{a}_{\mathrm{in}}, \qquad (3.8)$$

which must be solved simultaneous with its Hermitian conjugate equation. Taking the Fourier transform

$$\bar{a}[\omega] = \int_{-\infty}^{\infty} \mathrm{d}t \ e^{i\omega t} \hat{a}(t) \tag{3.9}$$

allows us to replace the time-derivative operator acting on $\hat{a}$ with multiplication by $-i\omega$, leading to the relation

$$\bar{a}[\omega] = \sqrt{\kappa} \left(\frac{(\kappa/2 - i\omega)\bar{a}_{\mathrm{in}}[\omega] - i\lambda \bar{a}_{\mathrm{in}}^{\dagger}[-\omega]}{(\kappa/2 - i\omega)^2 - \lambda^2} \right). \tag{3.10}$$

Finally, we apply the input-output boundary condition to determine the output field spectrum,

$$\bar{a}_{\mathrm{out}}[\omega] = \left(\kappa \frac{\kappa/2 - i\omega}{(\kappa/2 - i\omega)^2 - \lambda^2} - 1 \right) \bar{a}_{\mathrm{in}}[\omega] + \left(\frac{-i\kappa\lambda}{(\kappa/2 - i\omega)^2 - \lambda^2} \right) \bar{a}_{\mathrm{in}}^{\dagger}[-\omega] \tag{3.11}$$

$$= g_{\mathrm{sig},\omega} \bar{a}_{\mathrm{in}}[\omega] + g_{\mathrm{idl},\omega} \bar{a}_{\mathrm{in}}^{\dagger}[-\omega],$$

where we have identified the signal and idler amplitude gains as functions of the measured output frequency ω, which is defined such that $\omega = 0$ when the output field is measured at the JPA resonance frequency.

It is informative to consider the consequences of Eq. 3.11 for various values of λ. When $\lambda = 0$, a tone input at ω_{sig} leaves the JPA at the same frequency and with the same amplitude. As λ is increased, up to half the power of the incident tone is converted from ω_{sig} to $\omega_{\mathrm{idl}} = -\omega_{\mathrm{sig}}$, creating an output "idler" tone on the other side of the JPA resonance frequency, as in Fig. 3.3(a). In contrast, the noise power at ω_{sig} does not decrease, as it is replenished by noise converted from ω_{idl}. In the large gain limit, the signal-to-noise power ratio (SNR) at ω is thus lower than that of the input field by a factor of 2, as alluded to back in Fig. 2.4.

When $\lambda > \kappa/2$, then at very short times after the pump is switched on, the exponential growth driven by amplification is expected to outpace the exponential decay due to leakage out the JPA port. Approaching this critical value of λ, our simple model predicts the steady-state photon number will diverge; a more nuanced model or numerical simulation reveals a bifurcation of the JPA dynamics, and experimentally we observe the amplifier stops providing parametric gain.

Ideal squeezing performance requires that the higher-order terms in Eq. 3.5 remain negligible. In the limit of small flux-pump strength δf, the leading correction is $\Lambda J_0(\delta f) \cos F$, where $\Lambda = -E_J \Phi_{\mathrm{zpf}}^4/4 = -E_C/2$ is the Kerr nonlinearity of the resonator. While the Kerr nonlinearity is the mechanism used to produce parametric amplification when current-pumping the JPA, when flux-pumping the term is purely parasitic, leading only to dynamics that corrupt the squeezing. For both pumping schemes, reducing the ratio Λ/κ suppresses parasitic higher-order nonlinear effects, improving squeezing performance. This reduction

can be achieved by diluting the nonlinearity through the use of arrays of multiple SQUIDs, as in Section 2.6, which divides Λ by the square of the number of SQUIDs.

3.3 Interlude: Phase-sensitive amplification and squeezing

Equation 3.11 specifies the signal and idler gains, which together determine the output field component $\bar{a}_{\text{out}}[\omega]$ in terms of the input field components at $\pm\omega$, but how does this relate to phase-sensitive amplification and squeezing? The essential ingredient is the conjugation of the input field component $\bar{a}_{\text{in}}[-\omega]$ in that equation. Adding a complex number to its conjugate doubles the real-part and cancels the imaginary part; likewise, if we detect the output field in a way that sums $\bar{a}_{\text{in}}[\omega]$ and $\bar{a}_{\text{in}}^{\dagger}[\omega]$, then for large gain that field component is doubled (amplified) along X_1 and zeroed (squeezed) along X_2. However, in the output field these two pieces we want to sum may be at different frequencies: $\bar{a}_{\text{in}}[\omega]$ is part of $\bar{a}_{\text{out}}[\omega]$, while $\bar{a}_{\text{in}}^{\dagger}[\omega]$ is part of $\bar{a}_{\text{out}}[-\omega]$, spectrally positioned on opposite sides of ω_{JPA}. This implies that whether phase-sensitive or phase-preserving amplification is observed largely depends on whether the detector captures output-field frequency components on both sides of ω_{JPA} or only on one side, and thus depends on the spectral arrangement of the signal, amplifier, and detector. To understand this dependence, we first consider two common limiting cases relevant to experiments in later chapters. For simplicity we suppose the JPA bandwidth is very large in all cases.

First, we suppose that the detector (perhaps consisting of demodulation in a mixer followed by digital sampling) is slow compared to its detuning from the JPA, with a narrow bandwidth $\kappa_{\text{det}} < |\omega_{\text{sig}} - \omega_{\text{JPA}}|$ centered at ω_{sig}, as in Fig. 3.3(b). The response time of the detector ($\sim 1/\kappa_{\text{det}}$) is so long that by comparison the coherent output-field component at ω_{idl} is rapidly rotating in phase-space, such that its contribution to the integrated field value averages to zero and is not detected, as suggested by the gray shaded region in the figure. The detected noise includes contributions from the input-field components $\bar{a}_{\text{in}}[\omega_{\text{sig}}]$ and $\bar{a}_{\text{in}}[\omega_{\text{idl}}]$ per Eq. 3.11; since these two noise sources are uncorrelated, there is no phase-sensitive cancellation, and their sum is still isotropic (circular) in phase-space. This scenario in which only output-field components on one side or the other of ω_{JPA} are detected is an example of phase-preserving amplification. In this picture of phase-preserving amplification, we see that the usual 3 dB reduction in power SNR may be interpreted as information transferred to signal-idler correlations which are never detected.

In contrast, we now consider the limit of small signal-JPA detuning, and also center the detector at ω_{JPA}, as in Fig. 3.3(c). In the phase-space picture, the vanishingly-small detuning of the signal and idler components means they do not rotate appreciably within acquisition of a sample ($\sim 1/\kappa_{\text{det}}$) or from sample to sample, allowing them to add constructively or destructively in a phase-sensitive manner. Squeezing of the noise occurs because (for large gain) the frequency conversion process results in two almost identical copies of the same
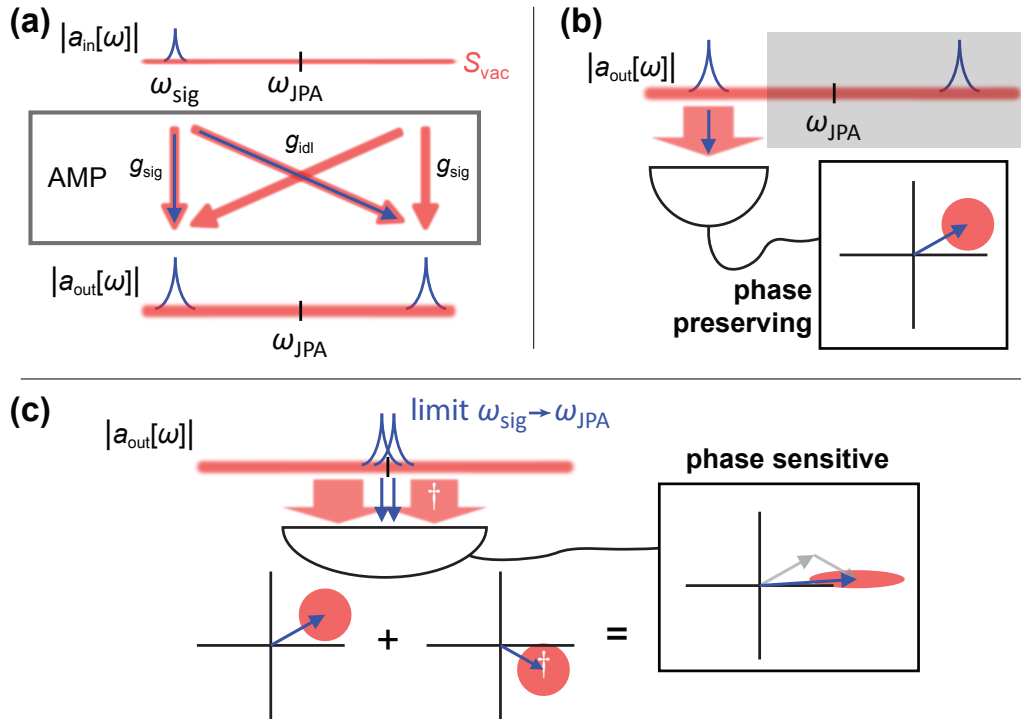
Figure 3.3: Phase-sensitive and phase-preserving detection. (a) The operation of a JPA is represented in frequency space. The JPA amplifies but also mixes the input signal and idler modes. Coherent (classical) components of the field are represented in blue, while noise is indicated in red. The diagonal arrows include both a scaling and conjugation of the input field component. Figure inspired by [72]. (b) Phase-preserving amplification is observed e.g. when the signal is captured by a detector with $\kappa_{\text{det}} \ll |\omega_{\text{sig}} - \omega_{\text{JPA}}|$. Here the mixing operation lowers the signal-to-noise power ratio of $a_{\text{out}}[\omega_{\text{sig}}]$ relative to that of $a_{\text{in}}[\omega_{\text{sig}}]$ by up to a factor of 2. (c) With increasing gain, the spectrum (signal and noise) above ω_{JPA} approaches a conjugated copy of the noise below ω_{JPA}. A detector centered at ω_{JPA} thus samples a field consisting of the sum of two mirror-image copies in phase-space, which add along the mirror axis and cancel along the orthogonal axis, leading to observation of phase-sensitive amplification and squeezing. The additional condition that $\omega_{\text{sig}} = \omega_{\text{JPA}}$ ensures that the amplification phase does not drift from sample to sample acquired by the detector. Experimentally this condition is often ensured by sourcing the signal and JPA pump from the same generator (though multi-channel direct digital synthesis may be preferable if available).
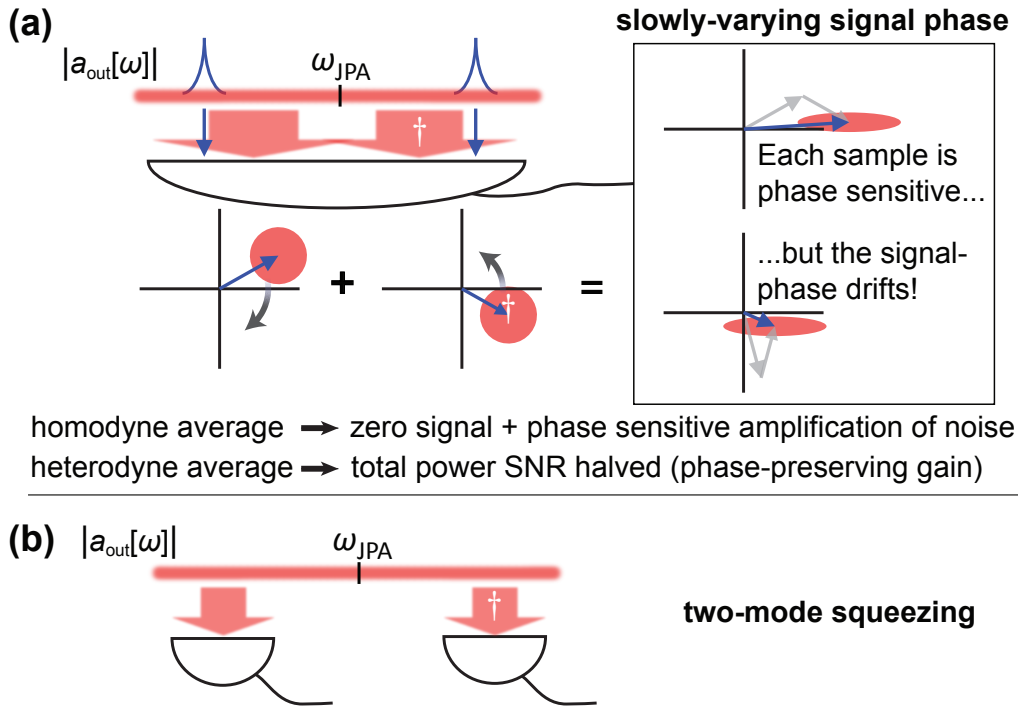
Figure 3.4: Two more detection schemes for consideration. (a) The detector centered at ω_{JPA} has sufficient bandwidth to detect coherent signal and idler tones which are appreciably detuned from ω_{JPA}. In the frame of the detector center frequency, the signal and idler are counter rotating, such that they drift between constructive and destructive interference (beating). As expected, the average power SNR has been reduced 3 dB compared to the SNR of the input field. (b) Two detectors symmetric about ω_{JPA} can be used to study two-mode squeezing.

noise fluctuations at frequencies symmetrically above and below ω_{JPA}, but with one copy reflected over an axis in phase space by the conjugation operation in Eq. 3.11. These two copies, represented by the broad red arrows and red circles, interfere constructively along the phase-space axis of reflection, producing phase-sensitive amplification, and destructively orthogonal to the axis, producing squeezing. The same reasoning applies to interference of the coherent parts of the signal and idler output fields. The signal can be aligned with the amplification axis by adjusting the relative phase of the signal and pump, producing constructive interference of the signal and idler that yields up to 6 dB more power gain perceived at the detector than occurs at the same pump strength for phase-preserving detection. However, the usual Heisenberg rules still apply: we can amplify without immediately losing any SNR in either quadrature, but the noise necessarily added by the remainder of the measurement chain ensures that we ultimately learn about only the amplified quadrature. As

we amplify one quadrature out of the quantum regime into the observable classical regime, we necessarily make the orthogonal quadrature increasingly inaccessible.

Can we capture the information encoded in the signal-idler correlations even for large detuning of ω_{sig}? The answer depends on precisely what we are trying to do. The Heisenberg uncertainty relations guarantee that, if we are trying to measure both quadratures of the field at ω_{JPA}, we inevitably will suffer 3 dB SNR reduction [70], irrespective of whether the idler mode is detected. On its own, the idler mode carries no information not already robustly encoded in the highly-amplified signal mode, assuming ideal high-gain JPA performance. Figure 3.4(a) shows that if we try to use a broadband detector to capture both signal and idler, the two drift in- and out-of-phase, averaging over the phase-sensitive amplification and deamplification conditions such that the average SNR has still been reduced by 3 dB. However, it is possible to split the output and capture the positive and negative frequency bands with separate detectors; the correlations thus observed, considered an example of two-mode squeezing, can exhibit phase-sensitive variances below the vacuum level [73, 74], though the topic is outside the scope of this thesis.

3.4 JPA gain and squeezing parameters

Finally, we can determine the definitions of several experimentally measurable quantities from Eq. 3.11. The phase-preserving power gain, which we call $G_{\text{JPA}}[\omega]$, is

$$G_{\text{JPA}}[\omega] = |g_{\text{sig},\omega}|^2 = \frac{((\kappa/2)^2 + \lambda^2 + \omega^2)^2}{((\kappa/2)^2 - \lambda^2 - \omega^2)^2 + \kappa^2\omega^2}. \tag{3.12}$$

In contrast, in phase-sensitive mode, greater power gain is observed for the optimal choice of pump phase. Taking the common case where $\omega_{\text{sig}} = \omega_{\text{idl}} = 0$, the power gain at this optimal phase condition (i.e. along the amplified phase-space axis) is

$$G_{\text{JPA,PS}} = (|g_{\text{sig}}| + |g_{\text{idl}}|)^2 = \left(\frac{\kappa/2 + \lambda}{\kappa/2 - \lambda}\right)^2. \tag{3.13}$$

The output-field squeezing parameters can also be calculated as functions of frequency [2, 75],

$$\begin{aligned}\bar{N}_{\text{out}}[\omega] &= \int d\omega' \, \langle \bar{a}^\dagger_{\text{out}}[\omega']\bar{a}_{\text{out}}[\omega]\rangle/2\pi \\ &= \frac{\lambda^2\kappa^2}{((\kappa/2)^2 - \omega^2 - \lambda^2)^2 + \kappa^2\omega^2},\end{aligned} \tag{3.14}$$

and

$$\begin{aligned}\bar{M}_{\text{out}}[\omega] &= \int d\omega' \, \langle \bar{a}_{\text{out}}[\omega']\bar{a}_{\text{out}}[\omega]\rangle/2\pi \\ &= \frac{\kappa\lambda\left((\kappa/2)^2 + \omega^2 + \lambda^2\right)}{((\kappa/2)^2 - \omega^2 - \lambda^2)^2 + \kappa^2\omega^2}.\end{aligned} \tag{3.15}$$

What does it mean to talk about squeezing as a function of frequency? The squeezing bandwidth describes the frequency span over which noise fluctuations above and below ω_{JPA} are correlated. If the squeezing is narrowband compared to κ_{det}, much of the noise spectrum sampled by the detector will be uncorrelated such that the detector sees minimal squeezing. In the time domain, we imagine the signal wave as a noisy time-series, and the idler wave as an approximate copy of that time-series that has been complex-conjugated[2]. Detecting the sum of these two, we thus observe destructive interference and squeezing in one field quadrature. However, if for example the idler wave were significantly delayed on its way to the detector, the two waves would be out of step, and we would no longer observe any cancellation. To see squeezing within each sample acquired, the delay must be less than $\sim 1/\kappa_{\mathrm{det}}$. This artificial example illustrates a more general rule that a large squeezing bandwidth is equivalent to noise fluctuations in $\bar{a}_{\mathrm{out}}[\omega_{\mathrm{sig}}]$ occurring close in time to the conjugated fluctuations in $\bar{a}_{\mathrm{out}}[\omega_{\mathrm{idl}}]$. Thus squeezing is often characterized in terms of time-dependent correlation functions of the field, such as can be made explicit by Fourier transforming Eqs. 3.14 and 3.15; for an extensive discussion of output-field correlations in the time domain see e.g. [76].

A convenient heuristic picture comes from considering signal and idler photons, mainly because they are arguably easier to visualize and talk about than noise fluctuations. Each pump photon creates a pair of correlated photons inside the JPA, one at ω_{sig} and one at ω_{idl}, and we suppose that both photons must arrive at the detector within the integration time of the detector in order for the noise cancellation to manifest. In this heuristic picture, the photons bounce around inside the JPA until they randomly exit to the transmission line, with the probability of exiting the JPA per unit time set by the bandwidth in terms of κ and λ. If this effective JPA bandwidth is very large, both photons leave the JPA very quickly, and thus are more likely to both arrive at the detector within the detector's integration time, indicating broadband squeezing.

If we operate in the regime where amplification and squeezing processes are broadband compared to all relevant experimental bandwidths, we can approximate the ideal gain and squeezing parameters by their $\omega = 0$ values, summarized here:

$$G_{\mathrm{JPA}} = \left(\frac{(\kappa/2)^2 + \lambda^2}{(\kappa/2)^2 - \lambda^2} \right)^2, \tag{3.16}$$

$$\lambda = \frac{\kappa}{2} \sqrt{\frac{\sqrt{G_{\mathrm{JPA}}} - 1}{\sqrt{G_{\mathrm{JPA}}} + 1}}, \tag{3.17}$$

$$G_{\mathrm{JPA,PS}} = \left(\frac{\kappa/2 + \lambda}{\kappa/2 - \lambda} \right)^2 = (\sqrt{G_{\mathrm{JPA}}} + \sqrt{G_{\mathrm{JPA}} - 1})^2, \tag{3.18}$$

$$N_{\mathrm{out}} = \frac{\kappa^2 \lambda^2}{((\kappa/2)^2 - \lambda^2)^2} = G_{\mathrm{JPA}} - 1, \tag{3.19}$$

---

[2]If we insist on working in non-rotating phase-space (lab-frame) and discussing only the real part of the wave, the complex-conjugation implies the idler wave oscillates between having the same sign as the signal wave (say, at times $t\omega = 0, \pi, ...$) or the opposite sign ($t\omega = \pi/2, 3\pi/2, ...$).

$$M_{\text{out}} = \frac{\kappa\lambda\left((\kappa/2)^2 + \lambda^2\right)}{((\kappa/2)^2 - \lambda^2)^2} = \sqrt{G_{\text{JPA}}(G_{\text{JPA}} - 1)}, \tag{3.20}$$

and

$$\text{amount of squeezing} = \frac{\sigma_{\text{vac}}^2}{\sigma_-^2} = \left(2(1/2 + N - M)\right)^{-1}, \tag{3.21}$$

where the amount of squeezing is usually reported in dB. Note that these equations are not independent, but are listed individually as a convenient reference. Equations 3.19 and 3.20 satisfy the condition for optimal squeezing, $M = \sqrt{N(N+1)}$. More general forms of several of these expressions are given in [2], allowing for nonzero pump detuning, nonzero loss inside the JPA, and arbitrary pump phase (amplification axis)[3]; these complications were neglected here for pedagogical simplicity.

3.5   Example: Cascaded attenuation and amplification of a squeezed state

We consider the cascaded configuration of amplifiers shown in Fig. 3.5, which is similar to experimental configurations used in later chapters. Unsqueezed vacuum, perhaps from a cold resistive termination, arrives at the first JPA, producing a squeezed state in the JPA output field. This squeezed state travels through loss $1 - \epsilon_{\text{in}}$ before being amplified by the second JPA and then experiencing additional loss $1 - \epsilon_{\text{out}}$. Separate measurements using a vector network analyzer determine the phase-preserving gain of the first JPA, G_{SQZ}, and of the second JPA, G_{AMP}. What are the squeezing parameters describing the field at each node in the circuit?
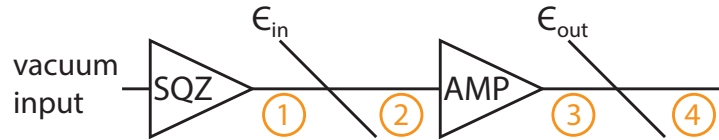
Figure 3.5: A cascaded system of amplifiers with loss before and after the second amplifier. The diagonal lines indicate beam splitters modeling the power losses $1 - \epsilon$. The fourth port on each beam splitter is assumed to couple in unsqueezed vacuum fluctuations such that the loss decreases N and M but leaves the $1/2$ term in each variance unchanged. We find the squeezing parameters N_i and M_i at each node $i = 1...4$ indicated in orange.

The squeezing parameters at the output of the first JPA can be read off of Eqs. 3.19 and 3.20, giving $N_1 = G_{\text{SQZ}} - 1$ and $M_1 = \sqrt{G_{\text{SQZ}}(G_{\text{SQZ}} - 1)}$. The loss attenuates these

---

[3]See the arXiv version for even more equations. Note that the expression for $\bar{M}_{\text{out}}[\omega]$ in that paper currently seems to be missing a factor of $1/2$ in a numerator term—check that $M = \sqrt{N(N+1)}$ for the case of no internal loss.

parameters such that $N_2 = \epsilon_{\text{in}}(G_{\text{SQZ}} - 1)$ and $M_2 = \epsilon_{\text{in}}\sqrt{G_{\text{SQZ}}(G_{\text{SQZ}} - 1)}$. We now consider three possible configurations of the second JPA: (a) phase-sensitive amplification aligned with the first JPA, (b) phase-sensitive amplification orthogonal to the first JPA, and (c) phase-preserving amplification. While more rigorous quantum derivations are possible, it is valid and often practical to simply scale the variances of the initial Gaussian Wigner functions by the relevant gain factors and then read off the resulting variances.

(a) In the first case, the quadrature variances after the second JPA are

$$\sigma_{\pm,3}^2 = (G_{\text{AMP,PS}})^{\pm 1}\sigma_{\pm,2}^2 = (G_{\text{AMP,PS}})^{\pm 1}(1/2 + N_2 \pm M_2)/2. \tag{3.22}$$

Since it is also true that $\sigma_{\pm,3}^2 = (1/2 + N_3 \pm M_3)/2$, we can solve for N_3 and M_3, yielding

$$N_3 = G_{\text{AMP,PS}}\sigma_{+,2}^2 + \frac{\sigma_{-,2}^2}{G_{\text{AMP,PS}}} - 1/2 \tag{3.23}$$

$$M_3 = G_{\text{AMP,PS}}\sigma_{+,2}^2 - \frac{\sigma_{-,2}^2}{G_{\text{AMP,PS}}}. \tag{3.24}$$

(b) The second case, where the amplification axis of the second JPA has been rotated $\pi/2$ in phase-space, is equivalent to (a) with the mapping $G_{\text{AMP,PS}} \to 1/G_{\text{AMP,PS}}$, yielding

$$N_3 = G_{\text{AMP,PS}}\sigma_{-,2}^2 + \frac{\sigma_{+,2}^2}{G_{\text{AMP,PS}}} - 1/2 \tag{3.25}$$

$$M_3 = G_{\text{AMP,PS}}\sigma_{-,2}^2 - \frac{\sigma_{+,2}^2}{G_{\text{AMP,PS}}}. \tag{3.26}$$

Note that here the value of M_3 may be negative, as in e.g. the case of $G_{\text{AMP}} > G_{\text{SQZ}}$ with $\epsilon_{\text{in}} = 1$ where the quadrature initially containing amplified noise ends up as the squeezed quadrature.

(c) If the second amplifier is operated in phase-preserving mode, phase-space is scaled isotropically by $\sqrt{G_{\text{AMP}}}$, so the output variances are

$$\sigma_{\pm,3}^2 = G_{\text{AMP}}\sigma_{\pm,2}^2 = G_{\text{AMP}}(1/2 + N_2 \pm M_2)/2 \tag{3.27}$$

from which we can solve for N_3 and M_3 to find

$$N_3 = G_{\text{AMP}}(1/2 + N_2) - 1/2 \tag{3.28}$$

and

$$M_3 = G_{\text{AMP}}M_2. \tag{3.29}$$

In the limit of large G_{AMP}, this gives $N_3/G_{\text{AMP}} = 1/2 + N_2$. It is perhaps notable that although the present calculations are equivalent to graphically stretching phase-space ellipses, and thus are simple enough to be simulated in MS Paint, they capture the subtle effect that

the large-gain limit of phase-preserving amplification necessarily adds half a noise photon referenced to the amplifier input as alternately depicted in Fig. 3.3(a).

Finally, for cases (a), (b), and (c), we find the final state at the end of our system by multiplying by the final power transmission factor, $N_4 = \epsilon_{\text{out}} N_3$ and $M_4 = \epsilon_{\text{out}} M_3$, which can be readily rewritten in terms of the known quantities. We emphasize that all calculations in this section are independent of any mean coherent displacement α, so the results also describe the noise properties of a displaced squeezed state (granted the usual assumption that corrections to Eq. 3.5 remain small). We employ variants of this general calculation to determine the effects of squeezing in the experimental systems in the following chapters.

3.6 Squeezing degradation due to higher-order effects of the JPA nonlinearity

Here we briefly present an intuition for a leading limitation on JPA squeezing. This simple pictorial guide is designed to give experimentalists a working, directionally-correct intuition; for a far more complete mathematical treatment see [2].
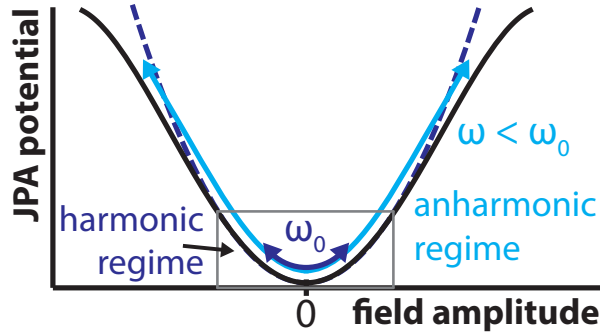
Figure 3.6: Anharmonic potential of a JPA (cartoon). The potential is well described by a parabola near the minimum. In this harmonic regime (gray box), small-amplitude oscillations occur with frequency ω_0. At greater field amplitudes, the potential is broadened compared to a parabolic potential, such that the oscillation frequency is decreased. This follows from Eq. 1.6, which indicates that a larger oscillating current in the JPA increases the Josephson inductance, lowering the effective JPA frequency.

The nonlinearity of the Josephson inductance defines an effective anharmonic potential, as represented in Fig. 3.6. For now we do not apply any JPA pump. Small-amplitude oscillations of the JPA field stay near the bottom of the potential, which is well described by a parabola, and thus oscillate at a frequency we call $\omega_{\text{JPA},0}$. Accordingly, if we represent the JPA field in the phase-space frame also rotating at $\omega_{\text{JPA},0}$, the Wigner function representing the field appears stationary. Now suppose we increase the amplitude of the field oscillations

by squeezing as in Fig. 3.7. These large fluctuations sample the potential outside of its parabolic regime; on average, the potential experienced by the field is broader than the harmonic potential, so the oscillation frequency of the field is lower. If we stay in the phase-space frame rotating at $\omega_{\mathrm{JPA},0}$, then these large-amplitude fluctuations appear to be rotating backwards (clockwise). Supposing the JPA field is initialized in a highly squeezed state centered at the phase-space origin, we thus expect (neglecting dissipation) the ends of the squeezing ellipse to be sheared in the direction of negative phase, producing an S-shape. These distortions increase the variance in the squeezed quadrature[4], reducing the amount of squeezing realized. The situation can be even worse if the JPA field is initialized in a displaced squeezed state as in the lower panel of Fig. 3.7. We expect one end of the ellipse to be more heavily sheared than the other end, which depending on the squeezing angle may produce a comma-like shape (sometimes referred to as an "avocado" by Californians). Moreover, because the squeezed state is already displaced, the amount of squeezing will be degraded even for small amounts of initial squeezing. One implication is that pumping the JPA with a resonant current pump, which necessarily produces a mean displacement of the JPA field, is expected to provide inferior squeezing performance compared to flux-pumping or sideband current-pumping. More generally, greater squeezing becomes possible by extending the harmonic regime, i.e. by weakening the JPA nonlinearity, which can be achieved using multiple SQUIDs [59]. Speculating further, it seems plausible that squeezing performance might also be improved by incorporating recently developed Josephson elements hard-wired to suppress undesired nonlinear processes [77] into future amplifier designs.

---

[4]And actually change which quadrature has the smallest variance.

squeezed vacuum:

displaced squeezed state:
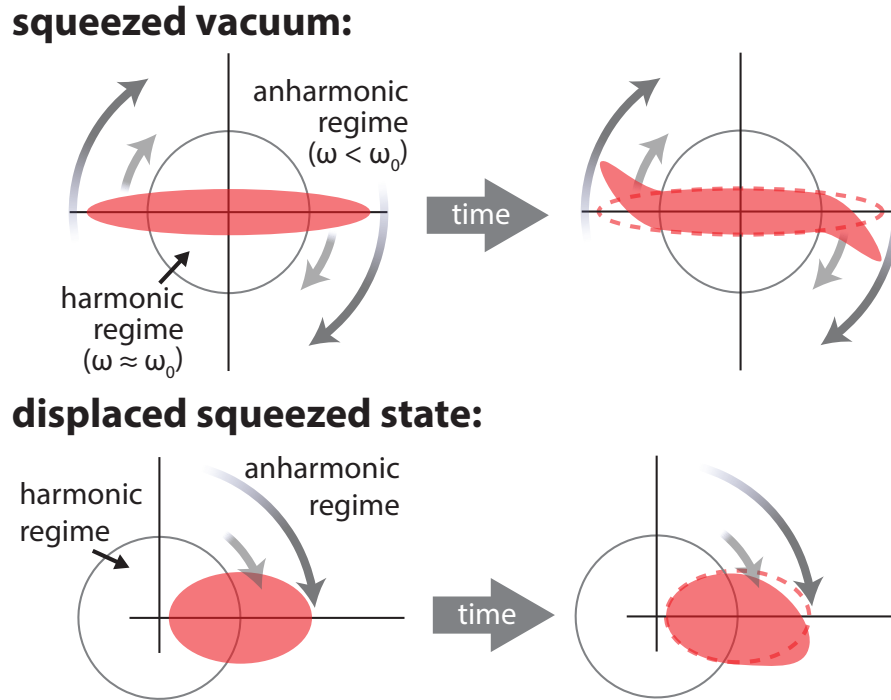
Figure 3.7: We approximately partition phase-space into a harmonic regime (inside the solid gray circle) in which the field oscillates at ω_0, and an anharmonic regime (outside) at which the field oscillates slower than ω_0, with greater radii corresponding to lower frequencies. The shown phase-space frame rotates at ω_0, such that the anharmonic regime appears to be sheared clockwise over time. For a highly-squeezed state centered at the origin, this can produce an S-shape distortion. Because displaced squeezed states are not centered at the origin, a different shape is produced by the shearing effect, and the shearing effect can be significant even for little or no squeezing. Figures are not to scale; see Ref. [2] for numerical simulations of JPA output fields considering the full JPA nonlinearity for various conditions.

Chapter 4

Resonance Fluorescence with a Squeezed Drive

4.1   Introduction

Fluorescence spectra provide a powerful means of probing atomic systems and their electromagnetic environments. Spectra such as the Mollow triplet [78] have been observed as signatures of coherent coupling of radiation to artificial atoms based on quantum dots [79] and superconducting qubits [80, 81]. The centrality of electromagnetic fluctuations to relaxation processes motivates an investigation into how electromagnetic squeezing modifies an atomic system's fluorescence. The simplest case was first treated theoretically by Gardiner [66], followed shortly by a paper by Carmichael, Lane, and Walls generalizing to the case of a Rabi-driven qubit [82, 83]. Their results implied that under certain conditions any resonant Gaussian drive field, including ideal squeezed states, could be fully characterized from the positions and linewidths of the fluorescence spectrum. A two-level system then realizes a nearly ideal detector of squeezed radiation, mapping the statistical correlations of the squeezed noise field onto properties which can be read from a spectrum analyzer directly. A multitude of theoretical predictions for various atomic interactions with squeezed light followed [84, 85], but experimental progress did not keep apace, in part because coupling an atom predominantly to a squeezed optical field proved challenging [86]. The central theoretical predictions for squeezed light-matter interactions remained unrealized for nearly three decades. The development of circuit quantum electrodynamics provided a naturally low dimensional environment in which efficient coupling to a single electromagnetic mode is possible [87], enabling observation of the effect of squeezing on radiative dipole decay rates of a superconducting qubit [34]. The work discussed in this chapter extends the circuit QED toolset to measure directly the effect of electromagnetic squeezing on resonance fluorescence [1].
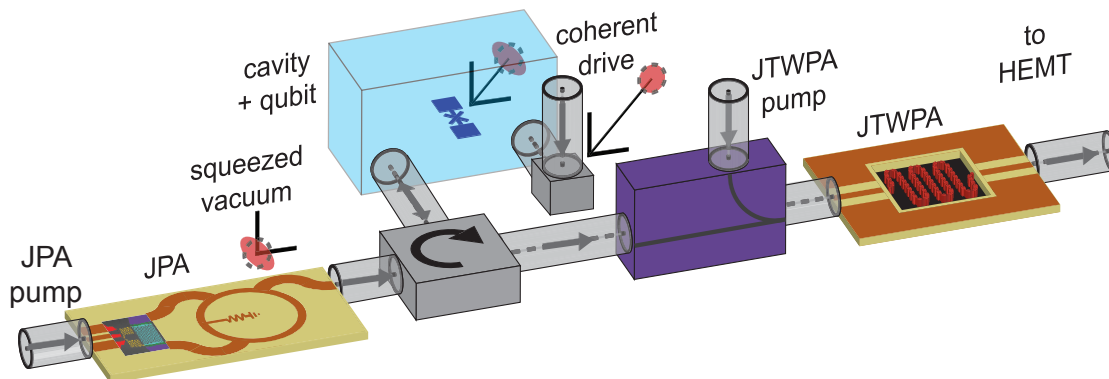
Figure 4.1: Simplified experimental setup for measurements of resonance fluorescence in squeezed vacuum. A flux-pump tone (left) modulates the resonance frequency of a JPA, producing squeezed vacuum which travels from the JPA to a superconducting cavity resonantly coupled to a transmon qubit. The qubit-cavity system is optionally Rabi driven via a second, weakly-coupled cavity port. The resulting fluorescence exits via the first cavity port and is amplified by a Josephson traveling wave parametric amplifier (JTWPA) before subsequent stages of amplification. Figure adapted from [1].

4.2   Experimental overview

We engineered the squeezed light-matter interaction using the experimental setup represented in Fig. 4.1. The JPA shined squeezed microwaves on a transmon-style qubit residing in a 3D aluminum waveguide cavity [43] inside a light-tight copper enclosure as in [3]. The qubit and cavity were made to be nearly resonant and were strongly coupled, such that the two-level system fluorescing in this experiment, the effective qubit, consisted of two levels of the hybridized qubit-cavity level structure. The predictions in [66, 82] for fluorescence from a true two-level system still apply for this effective qubit provided no other transitions are excited by the drives [88]. To meet this condition, we deliberately made the JPA narrowband, such that squeezing at the transition frequency of interest did not also generate significant noise power at neighboring transitions. A second cavity port allowed for application of a resonant Rabi drive to induce fluorescence; keeping this port weakly coupled compared to the first cavity port prevented unsqueezed vacuum incident to this second port from significantly diluting the intracavity squeezing. Fluorescence resulting from the squeezed drive exited the cavity via the strongly-coupled port and was amplified by a Josephson Traveling Wave Parametric Amplifier (JTWPA), another type of superconducting parametric amplifier with large bandwidth and compression power compared to a JPA [89]. After additional stages of amplification, the fluorescence was detected by a microwave spectrum analyzer. For a detailed wiring diagram and additional hardware-related commentary, see Appendix A.1.

4.3   Squeezing induced fluorescence

We first investigated the fluorescence produced by driving the qubit with squeezed vacuum only – that is, without any coherent drive applied to the weakly-coupled port. This process was described theoretically by Gardiner [66], who considered the case of a two-level atom resonantly driven by broadband squeezed noise, with no coupling to any unsqueezed vacuum modes. Assuming all fluorescence exits via a single channel, one can use the quantum regression theorem to calculate the correlation function of the resulting output fluorescence field,

$$\langle a_{\text{out}}^{\dagger}(t)a_{\text{out}}(0)\rangle = N\delta(t) + \frac{\gamma M}{2(2N+1)}\left(\exp(-\gamma_y|t|) - \exp(-\gamma_x|t|)\right),\qquad(4.1)$$

the Fourier transform of which gives the power spectral density,

$$2\pi S(\omega) = N + \frac{\gamma M}{2N+1}\left[\left(\frac{\gamma_y}{\gamma_y^2 + \omega^2}\right) - \left(\frac{\gamma_x}{\gamma_x^2 + \omega^2}\right)\right],\qquad(4.2)$$

where ω is defined to be zero at the atomic resonance. This fluorescence spectrum consists of three terms. The first corresponds to the broadband noise power of the input squeezed field, set by the effective number of noise photons N, and thus depends neither on properties of the qubit resonance (apart from the assumption that all input power is ultimately scattered to the one output channel) nor on the squeezing parameter M. The other two terms comprise a broad negative Lorentzian of width γ_x and a narrow positive Lorentzian of width γ_y. The negative Lorentzian can be understood as absorption by the qubit of photon pairs from the squeezed field, while the positive Lorentzian corresponds to the resonant reemission of that power by the qubit, realizing the four-wave mixing process depicted in Fig. 4.2. Barring any additional loss mechanisms, energy conservation requires the spectral weights of the emission and absorption Lorentzians be equal, and indeed both are set by the common prefactor. We see that without any correlated photons ($M = 0$) the Lorentzians vanish. In the absence of a coherent drive, any fluorescence from the qubit thus indicates $M \neq 0$, indicative of a squeezed state if the thermal component of the field is small ($N < M$). Since the Lorentzian linewidths are simply the product of the quadrature variances of the drive field multiplied by the natural qubit linewidth γ, by measuring the spectrum one can fully determine the parameters N and M provided γ is known.

Pumping the JPA for gain at the frequency of our effective qubit produced squeezed vacuum, which in turn drove fluorescence. For these measurements, the weakly coupled port was not used as we did not apply any coherent drive to the qubit. With the JPA pump power chosen to produce 1.4 dB of phase-preserving gain, we observed the spectrum shown in Fig. 4.3(a). As expected, the spectrum consists of a broad dip superposed with a narrow peak. Because the coupling of the second cavity port was not completely negligible, we modified Eq. 4.2 as follows

$$2\pi S(\omega) = \frac{N}{\eta_c} + \gamma\left[\frac{M - (1-\eta_c)N}{2N+1}\left(\frac{\gamma_y}{\gamma_y^2 + \omega^2}\right) - \frac{M + (1-\eta_c)N}{2N+1}\left(\frac{\gamma_x}{\gamma_x^2 + \omega^2}\right)\right],\qquad(4.3)$$
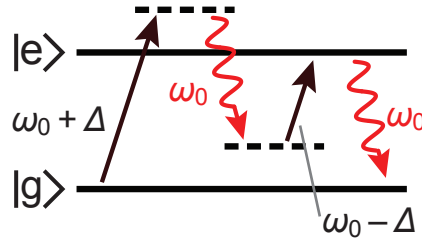
Figure 4.2: The squeezed vacuum incident to the qubit contains pairs of photons (black arrows) symmetrically detuned from the qubit center frequency. The simultaneous arrival of a given pair of photons at the qubit drives the two-photon absorption process depicted here. The absorption of noise power symmetrically above and below resonance produces the broad negative Lorentzian in Eq. 4.2, while the resonant reemission of this power produces the narrow positive Lorentzian.

where η_c represents coupling of the qubit-cavity resonance to unsqueezed electromagnetic modes, with Eq. 4.2 recovered when $\eta_c = 1$. Using a vector network analyzer to probe the effective qubit resonance in reflection geometry (S_{11} of the strongly-coupled cavity port), we independently determined the external and internal quality factors (in this case representing coupling to squeezed and unsqueezed modes, respectively) from which we calculated $\eta_c = Q_{\text{int}}/(Q_{\text{ext}} + Q_{\text{int}}) = 0.81$. Combining this number and a separately measured value of the radiative linewidth in ordinary vacuum, $\gamma = 304$ kHz, we observe that the observed spectrum is well described by a fit of Eq. 4.3. For example, from the fit of the spectrum shown in Fig. 4.3(a), we infer that $M - N = 0.21(1)$ at the qubit, corresponding to 2.4 dB of squeezing at the qubit for this JPA pump power.

To further understand how the fluorescence depends on the squeezed nature of the drive field, we repeated this measurement while slightly detuning the JPA pump tone above and below the resonance condition. The results are shown in Fig. 4.3(b). Here the color scale encodes the fluorescence power, with red indicating fluorescence and blue indicating absorption. The slice indicated by the white dashed line corresponds to the data in Fig. 4.3(a). Measurements above (below) the white dashed line were taken with the input squeezing central frequency (vertical axis) detuned above (below) the effective qubit resonance condition. All pump detunings shown here are small compared to the JPA bandwidth, such that the power incident to the qubit within the displayed span is approximately constant. However, the statistics of the fluctuations of the incident field in the frame of the qubit do change. Graphically, detuning the squeezing causes the squeezing ellipse to rotate in phae-space with respect to the qubit frequency; when this rotation is fast compared to the qubit lifetime, the qubit responds as if driven by a thermal field (circular in the IQ plane), and fluorescence is suppressed. In the language of Chapter 3, the qubit acts as a detector with $\kappa_{\text{det}} = \gamma$. Thus we see a sharp decrease in fluorescence intensity when the squeezing is detuned by an amount $\sim \gamma$, even though this detuning is much smaller than the squeezing bandwidth.
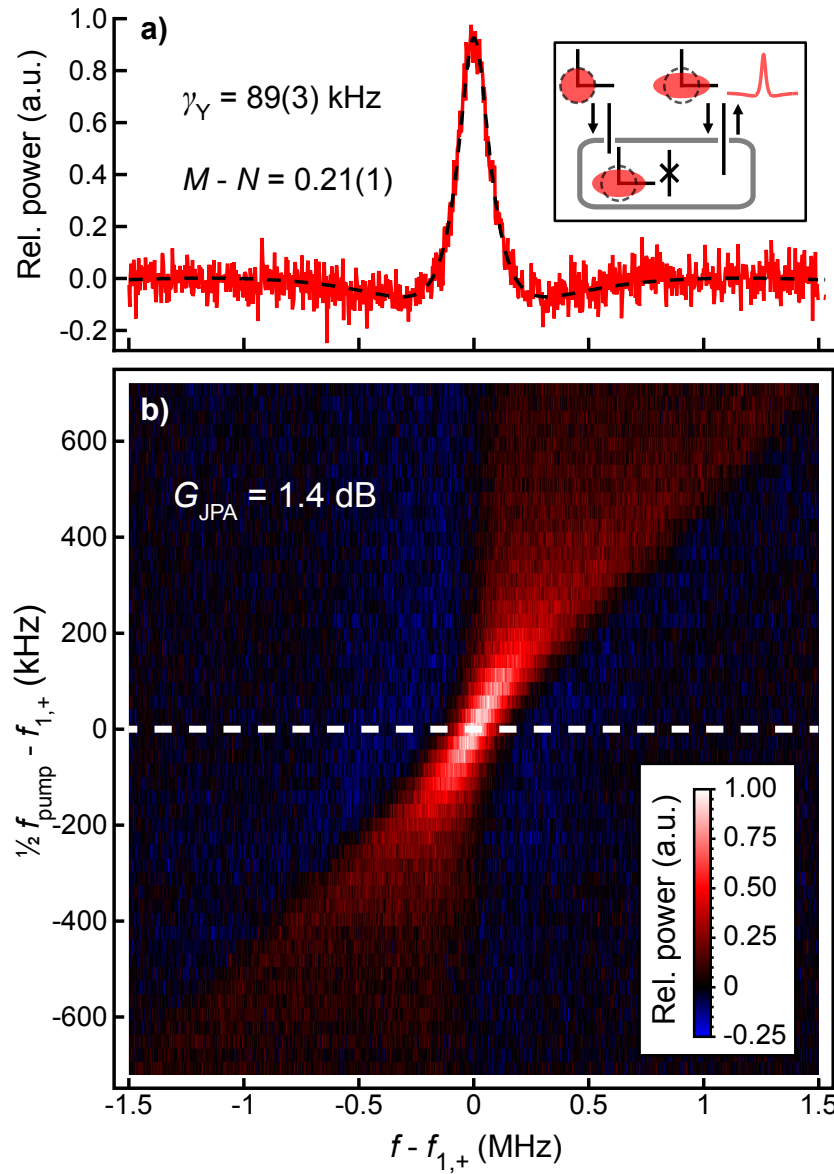
Figure 4.3: Fluorescence induced by injected squeezing. The spectrum in (a) is produced by injecting squeezed vacuum centered at the resonance frequency of the effective qubit. The photon correlations of the squeezed field drive a four-wave mixing process in which power is absorbed symmetrically above and below the resonance, then resonantly emitted, producing a broad negative Lorentzian dip (absorption) and a narrow Lorentzian peak (emission). In the ideal case the areas of these Lorentzians are equal per conservation of energy, while the widths of the two Lorentzians are proportional to the variances of the squeezed and antisqueezed field quadratures. The subnatural linewidth of the positive Lorentzian, γ_Y, is a hallmark of squeezing. Panel (b) shows that detuning the pump breaks the symmetry of photon correlations about the resonance, suppressing the fluorescence mechanism. The white dashed line corresponds to the data in (a). Figure adapted from [1].

4.4 The Mollow triplet

The fluorescence spectrum of a qubit in the presence of a strong coherent Rabi drive with no squeezing was first derived by the eponymous Mollow [78] and first reported experimentally five years later [90]. In the limit of a weak Rabi drive, the qubit incoherently scatters some of the incident light, producing a single fluorescence peak with a full-width γ determined by the qubit lifetime. For a strong Rabi drive such that the Rabi frequency $\Omega_R \gg \gamma$, the AC Stark interaction of the Rabi drive splits each of the qubit levels into a doublet with separation Ω_R, producing three distinct transition frequencies. The resulting "Mollow triplet" spectrum consists of three Lorentzian peaks, one centered at the qubit resonance and two sidebands detuned by $\pm\Omega_R$, in addition to the elastically-scattered part of the drive field modeled as a δ-function at ω_0. These three fluorescence frequencies are indicated on the level structure for our experiment by the red, green, and blue arrows in Fig. 4.4. Applying a Rabi drive to the weakly-coupled cavity port produced the spectrum shown in the second panel of Fig. 4.4. As expected the spectrum contains three fluorescence peaks, with a greater amplitude for the central peak as it includes fluorescence from two transitions. The peak separation is equal to the Rabi frequency, $\Omega_R/2\pi$, which is set by the amplitude of the coherent drive. Fig. 4.5 shows the expected linear dependence of the peak separation on the drive amplitude. For the measurements below, we choose our drive such that $\Omega_R/2\pi \approx 1$ MHz, which is large enough to resolve the sideband peaks but small enough to keep the entire fluorescence spectrum well within the bandwidth of the squeezer, a key assumption of the theoretical treatment given in [82].

4.5 Fluorescence with a squeezed Rabi drive

Carmichael et al. [82] showed that squeezing the fluctuations of a resonant Rabi drive, such that the drive is a displaced squeezed state (Fig. 3.1) instead of a coherent state, modifies the resulting fluorescence spectrum in a phase-sensitive manner. Introducing a resonant Rabi drive thus enables detection not only of the field quadrature variances set by N and M, but also of the squeezing phase. The spectrum still consists of three Lorentzians (for $\Omega_R \gg \gamma$), but the full-widths of the central peak and sidebands in the presence of squeezing become

$$\gamma_{\text{central}} = \gamma \frac{\sigma_{\text{amplitude}}^2}{\sigma_{\text{vacuum}}^2} = 2\gamma(1/2 + N + M\cos 2\Phi) \tag{4.4}$$

$$\gamma_{\text{sideband}} = \gamma \frac{1/2 + N + \sigma_{\text{phase}}^2}{2\sigma_{\text{vacuum}}^2} = \gamma(3/2 + 3N - M\cos 2\Phi), \tag{4.5}$$

where $\sigma_{\text{amplitude}}^2$ and σ_{phase}^2 are the field variances parallel and perpendicular to the mean-field displacement. Squeezing the amplitude fluctuations of the drive narrows the linewidth of the central peak below the natural linewidth and broadens the sidebands, while squeezing the phase fluctuations broadens the central peak linewidth and leaves the sideband linewidths
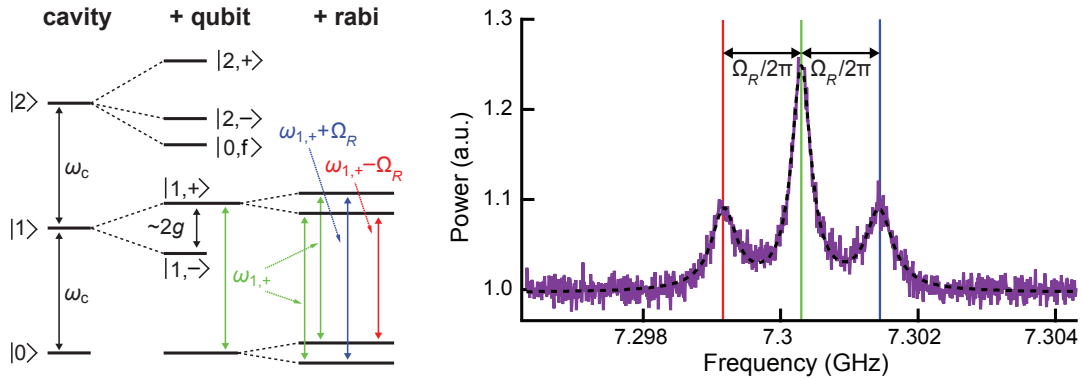
Figure 4.4: Mollow triplet level structure and spectrum. The cavity states (first column) are modified by strong coupling with the qubit, producing polariton states (second column). We chose the levels $|0\rangle$, $|1, +\rangle$ to define the two levels of our effective qubit (the $|0\rangle$, $|1, -\rangle$ transition was not chosen as it resided in the small frequency window where the dispersion feature of the JTWPA suppressed gain). Care was taken in designing the system to avoid driving transitions to any other states shown in the second column of the figure. Applying a resonant Rabi drive produces the dressed states shown in the third column, defining three distinct transition frequencies corresponding to the three peaks of the observed fluorescence spectrum shown at right. Figure adapted from [1].

unchanged. By fitting spectra taken at several phases of the squeezer pump (or Rabi drive), one determines not only the squeezing parameters N and M at the qubit, but also Φ, the phase of the squeezing relative to the Rabi drive. Figure 4.6 shows example spectra with (a) unsqueezed, (b) amplitude-squeezed, and (c) phase-squeezed Rabi drives. To further quantify the dependence of linewidths on squeezing angle, we step the squeezing angle more finely and fit each spectrum to an approximate model of three Lorentzian peaks, producing the inferred linewidths plotted in (d). As expected, the linewidths exhibit a sinusoidal dependence on Φ, with the central and sideband linewidths oscillating out-of-phase. These observations verify the predictions of [82], and provide a tool for characterizing microwave squeezed states as discussed further in the next section.

4.6 Squeezing characterization

The fluorescence measurements with or without a Rabi drive can be used to determine the variances of the squeezed and antisqueezed quadratures of the field experienced by the qubit for a range of JPA gains. Experimentally, we set the JPA gain by adjusting the JPA pump power and measured the gain using a vector network analyzer (VNA). For each gain setting, we measured the fluorescence spectrum with and without a Rabi drive.
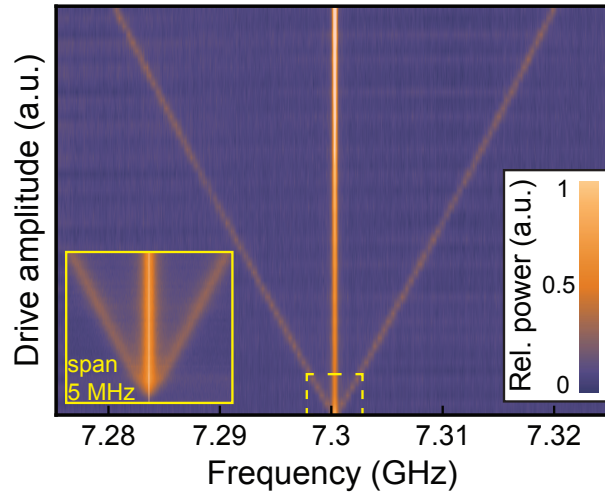
Figure 4.5: Mollow triplet spectrum vs Rabi drive amplitude. Color scale indicates fluorescence power produced by a Rabi drive applied to the weakly coupled cavity port. The Josephson Traveling Wave Parametric Amplifier (JTWPA) enables broadband detection of the spectrum over the 50 MHz span with approximately uniform gain. The spectra are normalized to the background level with no Rabi drive applied. The signal amplitude is varied by stepping the dc voltage applied to the IF port of a microwave mixer at room temperature. Figure adapted from [1].

Analysis of the spectra with a Rabi drive was challenging because due to bandwidth constraints the relation $\Omega_{\mathrm{R}} \gg \gamma$ was not fully saturated in our system, yet this relation is an assumption of the theory presented in [82]. To resolve this complication, our theory collaborators in the Blais group at U. Sherbrooke extended the analytical theory to the experimental regime, including for values of $\Phi \neq 0, \pi/2$ (Appendix B of [1]). This analytical model was verified by comparison to numerical simulation of the full cascaded master equation for our system. In contrast, spectra observed with no Rabi drive could be fit directly with the two-Lorentzian model of Eq. 4.3, with the amount of squeezing seen by the qubit determined from the width of the narrow positive peak.

The results of these two sets of measurements are displayed in Fig. 4.7. As expected, the amount of squeezing (right vertical axis) increases with greater JPA gain. The amounts of squeezing inferred via the two methods show reasonably good agreement with one another over the range of gains. As inferring the squeezing without a Rabi drive was simpler in execution and analysis, and was also less sensitive to small spectral background features, we believe that method to be more accurate and precise, as reflected in the smaller scatter of the blue triangles in the plot. Measurements with a Rabi drive may be of use when determining the squeezing phase Φ is also desired. We fit the results of this method to the expected
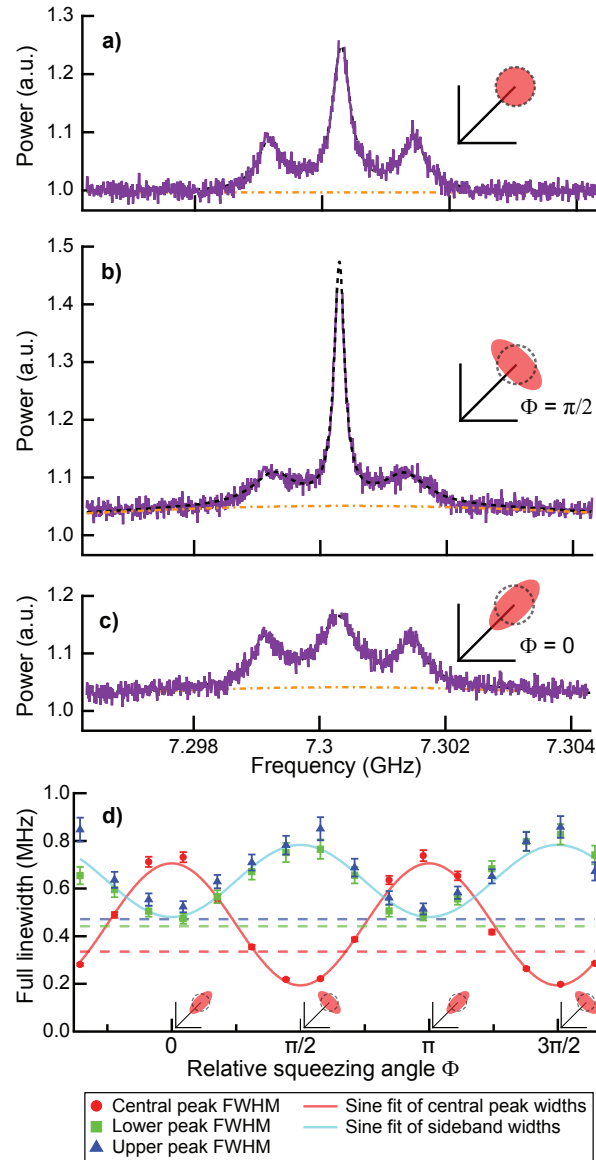
Figure 4.6: Fluorescence induced by a squeezed Rabi drive. Panels (a-c) show spectra produced by an unsqueezed, amplitude-squeezed, or phase-squeezed Rabi drive. The fits (black, dashed) consist of three Lorentzians plus a broad parabolic background (orange, dot-dashed). The background curvature is due to the finite bandwidth of the JPA. Spectra were acquired for a range of Φ values; the inferred linewidths are shown in (d) for the central (red) and sideband (blue, green) peaks. Horizontal lines indicate linewidths without squeezing. Curves are sinusoidal fits of the data. The Lorentzian model is illustrative but only approximate as the condition $\Omega_R \gg \gamma$ is not saturated; a more complete numerical model is used to determine squeezing levels reported in the next section. Figure adapted from [1].

amount of squeezing produced by an ideal JPA (Eq. 3.21) followed by loss $1 - \eta$,

$$(1 + 2N - 2M))^{-1} = (1 + 2\eta(N' - M'))^{-1} = \left(1 + 2\eta(G_{\text{JPA}} - 1 + \sqrt{G_{\text{JPA}}(G_{\text{JPA}} - 1)})\right)^{-1}. \tag{4.6}$$

Here N and M are the squeezing parameters of the field in the cavity, N' and M' are the squeezing parameters at the output of the JPA, and G_{JPA} is the phase-preserving power gain of the JPA as measured on the VNA. The single free parameter of this model is the efficiency $\eta = 0.55$ with which squeezing was transferred from the JPA to the qubit, where η includes both the microwave loss between the JPA and cavity and the effect of η_{c}.

We performed an additional measurement to close a loophole in the above measurements of squeezing. The measurements above demonstrate a reduction of the noise in one quadrature of the field at the qubit when the JPA is turned on. However, this inference implies squeezing only if the field is also known to be sufficiently close to the vacuum state when the squeezer is off. As the temperature of the plate on which the experiment was mounted was measured to be < 30 mK during the experiment, we did expect the 7.3 GHz qubit-cavity resonance to meet this condition, but thermalization of the qubit-cavity system to the plate could not be taken for granted, especially given the low thermal conductivity of the superconducting cavity. To close this loophole, we bounded the population in the excited state of our effective qubit with no squeezing applied, following the procedure in [91] (cf. Fig. 3 therein). These Rabi measurements bounded the excited state population below 1.2%, corresponding to a thermal population of the field $N_{\text{th}} < 0.01$, which has a negligible impact on the inferred squeezing levels shown in 4.7.

4.7 Outlook

Both generating and characterizing microwave squeezing in the electromagnetic environment of a qubit are central to proposed schemes for enhancing qubit measurement via applied squeezing. The methods presented here achieve this in a resource-efficient way, with the two-level system acting as a passive[1] black box that maps squeezing parameters onto spectra which can be detected without the need for time-domain qubit control. When it is not necessary to determine the phase of the squeezed state, a single-port cavity may be used, improving precision by making $\eta_{\text{c}} \approx 1$. This technique can be readily extended to confirm theory predictions for fluorescence under two-mode squeezed vacuum [92], under narrow-band squeezing which realizes a non-Markovian reservoir [93], or in parameter regimes expected to realize exotic spectral features [94]. The present experiment provided a straightforward characterizion of the squeezing performance of our JPA, and in the next chapter we turn to applying squeezing to qubit measurement.

---

[1]For measurements without a Rabi drive.
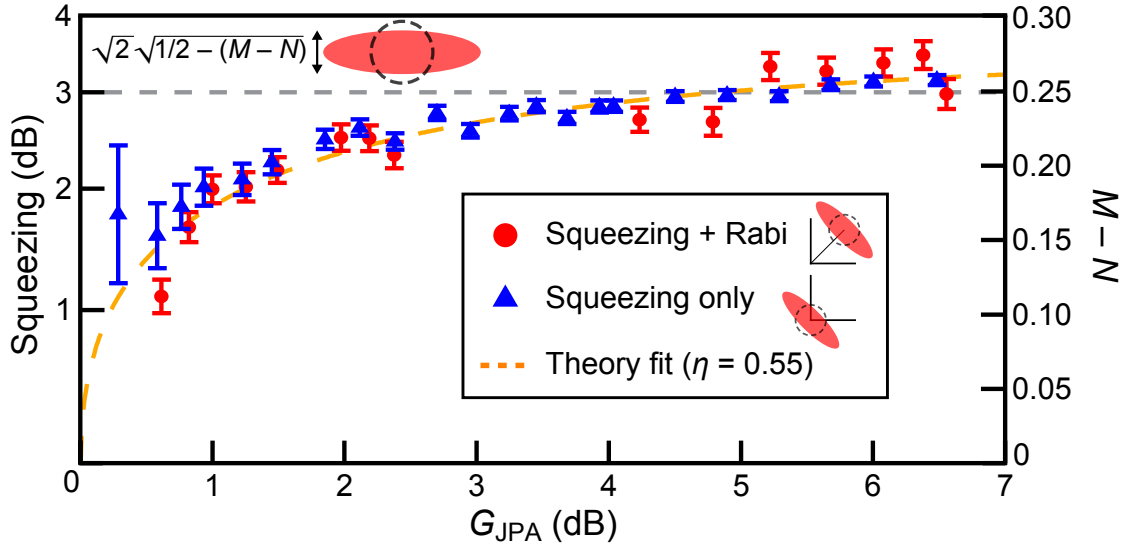
Figure 4.7: Inferred squeezing levels as a function of JPA gain. Squeezing levels were inferred by analyzing fluorescence spectra with (red circles) and without (blue triangles) a Rabi drive applied to the weakly-coupled cavity port. The horizontal axis indicates the gain G_{JPA} used to produce the squeezed field. This gain is the phase-preserving power gain as measured with a slightly detuned VNA probe tone, which is related to but distinct from the quadrature gain (compare eqs. 3.16 and 3.18). The left vertical axis indicates the inferred amount of squeezing at the qubit in dB, while the right axis indicates $M - N$, the combination of squeezing parameters which determines the squeezed quadrature variance as indicated on the inset in the upper left (the written expression is 2σ). The orange dashed curve is a one-parameter theory fit to the blue triangles. Figure adapted from [1].

Chapter 5

Stroboscopic Qubit Measurement with Squeezed Microwaves

5.1   Proposed utility of squeezed measurement fields

A major research focus of circuit QED has been the fast readout of the state of a superconducting qubit. The primary means of achieving this goal have been optimization of the cavity-mediated dispersive coupling of the qubit to a coherent measurement pulse, and the amplification of that pulse such that it can be efficiently detected at room temperature. Successes on these fronts have enabled qubit measurements with over 99% fidelity in less than 100 nanoseconds [18], and for the realization of error-correction with sufficiently low latency to extend the lifetime of a qubit [24]. Moreover, enhancements to the bandwidths and dynamic ranges of superconducting amplifiers [89, 28, 61] have made feasible frequency-multiplexed readout of many qubits simultaneously. However, as a practical universal quantum computer will require increasing system size and algorithmic complexity several orders of magnitude, improvements in measurement speed are expected to remain beneficial for facilitating error-correction and final state readout.

Here we perform what is to our knowledge the first experimental demonstration of using squeezed microwaves to speed up the measurement of a superconducting qubit. Squeezing the noise in the measurement field provides a means of increasing the signal-to-noise ratio (SNR) of the pulse leaving the readout cavity, or equivalently increasing the rate at which qubit state information is encoded in the field via interaction with the qubit. Naively, increasing the amplitude of the input readout pulse may appear to be a much simpler means of increasing SNR than is the delicate business of squeezing vacuum noise. However, the dispersive qubit-cavity coupling widely employed for readout intrinsically limits the usable pulse amplitude, defining a critical photon number $n_{\mathrm{crit}} = \Delta^2/(4g^2)$ on the order of which appreciable state-mixing and thus errors occur [1] [95, 96], where Δ is the qubit-cavity detuning

---

[1]A back-of-the-envelope derivation, albeit one not capturing the factor of 1/4, is to compare the energies of $|n, g\rangle$ and $|n-1, e\rangle$. Noting the Stark shift decreases the qubit frequency by $\sim \chi n$, these two levels become

and g is their coupling. This bound on photon number motivates asking whether more information can be transmitted by each photon. In general, the best possible scaling of SNR, known as Heisenberg scaling, is $\sqrt{\text{SNR}} \sim \bar{n}$, where we take the square-root following the convention that SNR is quoted with respect to power (field power / variance, as opposed to field amplitude / standard deviation). Without squeezing, $\sqrt{\text{SNR}}$ is proportional to the field amplitude divided by the vacuum standard deviation, and thus exhibits the more familiar scaling, $\sqrt{\text{SNR}} \sim \sqrt{\bar{n}}$. Thus squeezing in principle raises the ceiling on the speed with which a measurement can be performed, motivating investigation of whether practical implementation of squeezed readout is possible.

Squeezed fields are also of interest as a means of suppressing certain types of unwanted parasitic measurements. Just as squeezing can be used to speed up a measurement by making two output states more distinguishable, antisqueezing, i.e. squeezing of the orthogonal quadrature, can make the two states less distinguishable, slowing the measurement and reducing backaction on the qubit. It has been proposed that squeezing can be used in this way to increase the fidelity of multi-qubit gate operations [97]. Our experimental work includes the first demonstration of using squeezed microwaves to slow backaction of an applied measurement, providing a clean demonstration of the relation between continuous measurement backaction and SNR.

Additional details on the experiment described in this chapter may be found in [4].

5.2 Squeezing compatibility

A major obstacle to squeezed-readout implementation is that the dispersive coupling central to standard readout techniques rotates squeezing out of, and antisqueezing into, the signal quadrature, which severely limits the possible SNR improvement due to squeezing [98], especially in the common parameter regime where $\chi \sim \kappa$. Figure 5.1 illustrates this predicament. The dispersive qubit-cavity interaction Hamiltonian, $\hat{H} = \chi \hat{\sigma}_z a^\dagger a$, produces the readout signal as a qubit-state dependent phase-space rotation of the output field. In a conventional measurement, injecting a coherent state resonant with the cavity thus produces an output coherent state with one of two distinct phases (Fig. 5.1(left)). In standard homodyne measurement we choose to detect one quadrature of the output field; after projecting the phase-space distribution onto this axis (marginalizing the orthogonal quadrature), we define the SNR in terms of the resulting one-dimensional probability distributions as SNR $= 2(\langle V_e \rangle - \langle V_g \rangle)^2 / (\sigma_e^2 + \sigma_g^2)$, equal to the mean separation of the two coherent states divided by the mean variance (some definitions of SNR differ by a factor of 2). Ideally, we would like to apply squeezing such that the noise is reduced along the signal quadrature, as in the utopian scenario of Fig. 5.1(middle). However, if we simply perform the measurement by injecting a displaced squeezed state rather than a coherent state, the dispersive interaction rotates not only the mean value of the field but also the noise ellipse. Since the rotation is in opposing directions for the ground and excited states of the qubit, it is impossible

---

resonant when $n = \delta/\chi \approx \Delta^2/g^2$, enabling the measurement field to flip the state of the qubit.
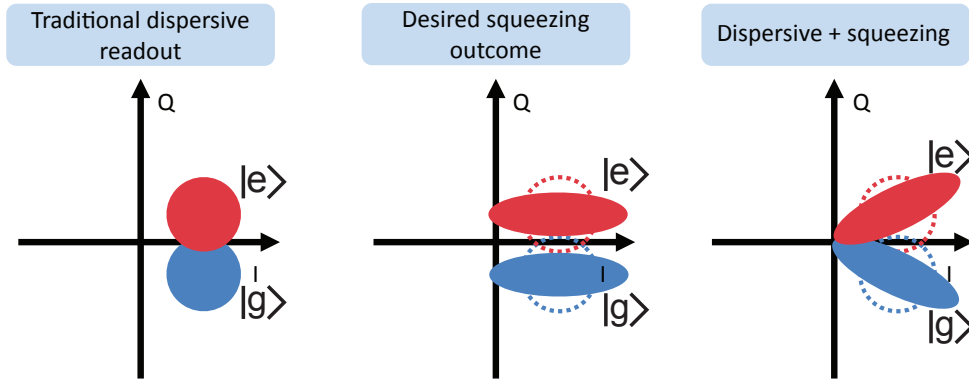
Figure 5.1: In traditional dispersive readout, the qubit-field interaction produces a qubit-state dependent readout of the output field. We would like to apply squeezing such that the noise is reduced along the signal quadrature, that is, along the axis connecting the mean values of the $|g\rangle$ and $|e\rangle$ field distributions. However, if we simply perform dispersive readout with injected squeezing, the dispersive interaction produces a rotation of the noise ellipses in opposite directions, rotating amplified (antisqueezed) noise into the signal quadrature.

to align the squeezed axes of both ellipses with the signal quadrature simultaneously (Fig. 5.1(right)). Modest SNR improvement is still possible for small amounts of squeezing and/or small dispersive rotations ($\chi \ll \kappa$), but with increased squeezing the antisqueezed variance quickly becomes large such that even a small rotation pollutes the signal quadrature with a large amount of noise.

While proposals to better exploit squeezing for qubit measurement have been suggested, they require more complex circuit architectures involving multiple readout modes [99, 100] or a fundamentally different "longitudinal" coupling of the qubit to a cavity quadrature ($\hat{\sigma}_z(a + a^\dagger)$) instead of to the photon number ($\hat{\sigma}_z a^\dagger a$) [101]. With a longitudinal coupling, the qubit signal manifests as a displacement rather than a rotation of the output field, eliminating the problem of squeezing misalignment. Rather than modify the circuit as proposed in [101], here we dynamically induce a synthetic longitudinal coupling, as demonstrated in [102], compatible with standard qubit designs. This approach utilizes a stroboscopic technique similar to those used with "backaction evading" optomechanical systems [103, 104, 105], though these techniques have not previously been combined with injected squeezing. The next section describes the stroboscopic technique in the context of our experimental hardware.

Figure 5.2: (a) Simplified experimental setup for stroboscopic measurement with squeezing. A first JPA ("SQZ") produces squeezed microwave vacuum, which is routed by circulators to the strongly-coupled cavit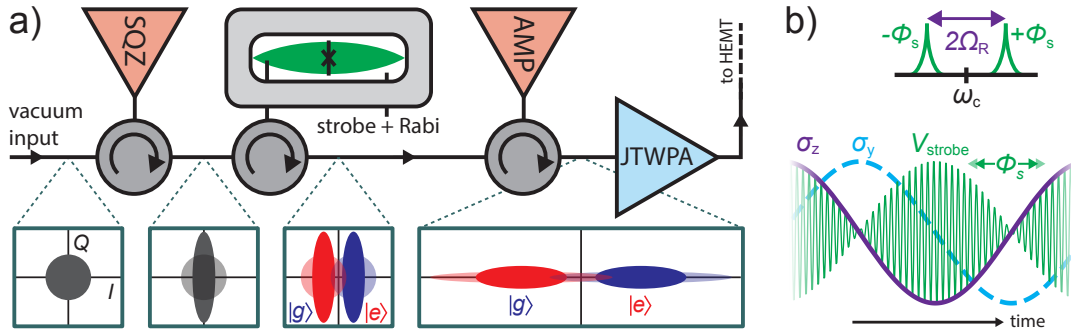y port, producing an intra-cavity squeezed vacuum state. A Rabi drive at ω_q and strobe tones near ω_c are injected simultaneously into the weakly coupled cavity port, producing a stroboscopic measurement interaction yielding a qubit-state dependent displacement of the cavity output field by $\pm 2\bar{a}_0 \chi/\kappa$. Squeezing increases the distinguishability (solid ellipses) of the two pointer states compared to the same measurement performed without squeezing (faded ellipses). (b) Varying the relative phase ϕ_S of the strobe tones shifts the resultant modulation envelope in time relative to the Rabi oscillations, allowing an effective measurement of any combination of $\hat{\sigma}_z$ and $\hat{\sigma}_y$ of the qubit in the Rabi-driven frame. For all measurements presented here, we choose to measure $\hat{\sigma}_z$. Figure adapted from [4].

5.3   Experimental setup and stroboscopic protocol

A schematic of our setup appears in Figure 5.2. The hardware is similar to that used in the resonance fluorescence measurements of Chapter 4. Once again, we have a JPA, labeled "SQZ", flux-pumped to produce squeezed microwaves which travel into the strongly-coupled port of a superconducting cavity containing a 3D-transmon style qubit [43], and we use superconducting amplifiers downstream to detect the cavity output field. Unlike in Chapter 4, the qubit ($\omega_q/2\pi = 3.898$ GHz) is far from resonance with the cavity ($\omega_c/2\pi = 6.694$ GHz) as in a typical dispersive measurement configuration, such that the qubit-cavity interaction absent any drives is described by the dispersive coupling $\chi/2\pi = 0.73$ MHz. We use the weakly-coupled cavity port to inject three tones that produce the stroboscopic measurement: a tone at ω_q that drives Rabi oscillations with a frequency Ω_R, and a pair of sideband tones symmetrically detuned by Ω_R above and below the cavity frequency (Fig. 5.2(b)). The two sidebands beat against one another, such that their sum equals a tone at the cavity frequency whose envelope is modulated at twice the Rabi frequency. This modulated drive stroboscopically probes a single Pauli component of the qubit state in the plane of the qubit's Rabi oscillations around the Bloch sphere. Adjusting the relative phase of the sidebands ϕ_s

shifts this envelope in time relative to the Rabi oscillations, varying which particular Pauli component is probed.

To get a heuristic picture of and intuition for this measurement, consider the cavity field in the phase-space frame rotating at the cavity frequency $\omega_{\rm c}$. If no qubit were present, the stroboscopic drive would cause the mean-field phasor to oscillate about the origin along a phase space axis, say the vertical axis Q. Now consider a toy model in which we crudely discretize the time evolution of the system such that the stroboscopic drive and the dispersive qubit interaction take turns, as in Fig. 5.3. (A caveat: the model as shown here does not accurately capture all system dynamics; the point of this model is to make it seem plausible that the time-averaged field drifts to the right if the qubit starts in the excited state, and to the left if the qubit starts in the ground state). First, the strobe drive displaces the mean cavity field to a maximum vertical position indicated by the faded phasor in (1). Next, also in (1), we briefly evolve the cavity field in time; if we assume the qubit starts in the excited state, the cavity field evolves at a slightly lower frequency due to the dispersive shift, and thus appears to rotate clockwise in our phase-space frame by a small amount (not shown to scale). Moving on to (2), the strobe drive displaces the cavity field in the opposite direction, indicated by the faded blue arrows. By this time the qubit has been Rabi driven into the ground state (purple curve), causing the cavity field to rotate clockwise in our chosen frame. We see that because $\hat{\sigma}_{\rm z}$ and Q have both changed sign, the net result of steps (1) and (2) has been to start monotonically increasing the I-component of the field while Q remains rapidly oscillating about zero at $\Omega_{\rm R}$. Had the qubit started in the ground state with $\hat{\sigma}_{\rm z} = -1$ instead, the direction of the dispersive rotation steps would be reversed, causing the time-averaged field to drift to negative I values, enabling state discrimination.

More precisely—and accurately—the interaction-picture Hamiltonian is $\hat{H}_{\rm I} = \chi\hat{\sigma}_{\rm z}a^\dagger a + \frac{\Omega_{\rm R}}{2}\hat{\sigma}_{\rm x} + \hat{H}_{\rm sb}$, where $\hat{H}_{\rm sb}$ describes the sideband drives. We write the cavity field as the sum of its mean-field and quantum fluctuations, $\hat{a} \to 2\bar{a}_0\cos(\Omega_{\rm R}t) + \hat{d}$, and transform to the Rabi-driven frame to find

$$\hat{H}_{\rm I} = \chi\bar{a}_0\hat{\sigma}_{\rm z}^{\rm R}(\hat{d} + \hat{d}^\dagger) + (e^{i\Omega_{\rm R}t}\hat{A} + e^{i2\Omega_{\rm R}t}\hat{B} + {\rm H.c.}). \tag{5.1}$$

The first term describes a longitudinal coupling between the cavity field and the measured observable $\hat{\sigma}_{\rm z}^{\rm R}$. This observable has an explicit time dependence in the original interaction picture, which with the right choice of $\phi_{\rm s}$ can be written as $\hat{\sigma}_{\rm z}^{\rm R} \leftrightarrow \cos(\Omega_{\rm R}t)\hat{\sigma}_{\rm z} - \sin(\Omega_{\rm R}t)\hat{\sigma}_{\rm y}$, such that the measurement of $\hat{\sigma}_{\rm z}^{\rm R}$ ideally provides the same information about the initial ($t = 0$) qubit state as would a measurement of $\hat{\sigma}_{\rm z}$. This interaction displaces the cavity output field in phase space by $\pm 2\bar{a}_0\chi/\kappa$ [102], producing separation of the squeezed pointer states sans rotation of the squeezing ellipses, as indicated downstream of the qubit in Fig. 5.2(a). The other terms in equation 5.2 are parasitic terms causing deviations from the ideal QND coupling, derived explicitly in the supplemental material of [4]. These include terms which would rotate the squeezing ellipses in a standard dispersive measurement, but now are strongly suppressed for $\Omega_{\rm R} \gg \kappa, \chi$. With the qubit-dependent rotation eliminated, the minor axes of the squeezing ellipses can be aligned to the signal quadrature in a straightforward way by adjusting Φ via the phase of the flux-pump.
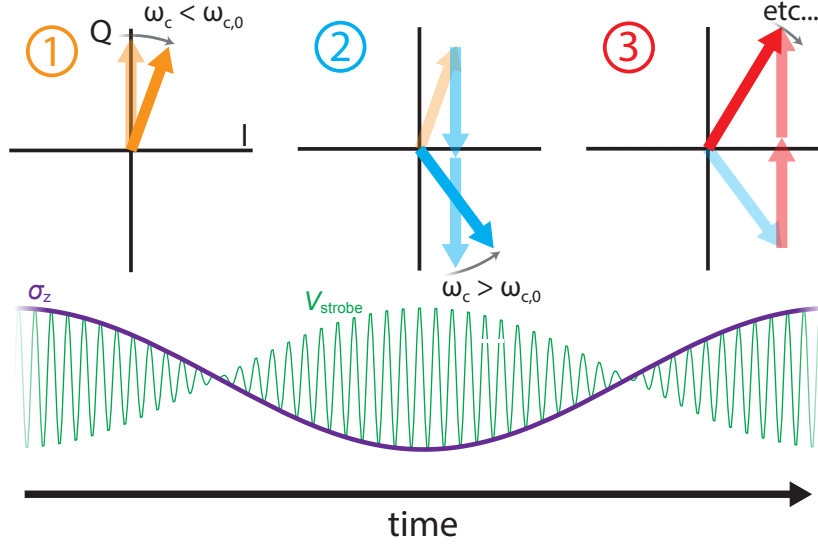
Figure 5.3: Toy model of the stroboscopic measurement scheme. We discretize time evolution into small steps; between each step, we apply a displacement along Q representing the stroboscopic drives, and also flip the sign of $\hat{\sigma}_z$ of the qubit to approximate the Rabi oscillations. By flipping the signs of Q and $\hat{\sigma}_z$ synchronously, we trick the dispersive interaction into providing a net displacement along I conditioned on the initial state of the qubit. See text for a step-by-step description of frames (1-3).

Even with optimal alignment of the squeezing to the signal quadrature, the field must be amplified with high efficiency η for the squeezing to have a measurable effect on the homodyne signal acquired at room temperature. Thus we amplify the output field not only with a JTWPA as in Chapter 4, but also with a JPA acting as a low-noise preamplifier ("AMP" in Fig. 5.2). The flux-pump of this second JPA is phase locked with the squeezer pump and measurement tones, producing phase-sensitive amplification of the signal. With even modest JPA gain, the effect of the half-photon of noise necessarily added during the phase-preserving amplification in the JTWPA can be mitigated, increasing η. Operating the JPA at low gain can be advantageous as it reduces deleterious higher-order effects of the device nonlinearity [2, 38].

Incidentally, this series configuration of phase-sensitive amplifiers resembles a single-mode "SU(1,1) interferometer" [106], a nonlinear system capable of using squeezing to achieve Heisenberg-limited sensitivity. Several recent experiments in the microwave domain not involving superconducting qubits have employed similar configurations of superconducting amplifiers [107, 74, 38]. The SU(1,1) interferometer gets its name from the natural representation of phase-sensitive amplification as a hyperbolic rotation, obeying the same mathe-

matics as a "boost" in the SU(1,1) geometry of special relativity[2]. In the canonical SU(1,1) system, the signal to be detected is a phase shift on one interferometer arm. Much like naive dispersive qubit readout with input squeezing, the interferometer can optimally exploit squeezing only in the limit of small phase shifts. In contrast, the stroboscopic light-matter coupling realized in our experiment in principle enables enhancement far outside these limits (appendix of [4]). Our scheme thus eliminates a central obstacle to practical application of squeezing to qubit measurement.

5.4 Squeezing measurement backaction

A circuit QED measurement can be divided into two parts: encoding qubit state information in component of the microwave field, and then amplification and detection of that field component. We characterize the first process, which occurs entirely inside the cavity, by determining the backaction on the qubit during the measurement, and characterize the second process in terms of the final room-temperature SNR. In this section we focus on the first process.

Measurement backaction is caused by fluctuations in the observable conjugate to that acquiring information about the system. For example, during a standard dispersive measurement, $\hat{\sigma}_z$ information is encoded in the phase of the cavity field, while backaction is exerted on the qubit by fluctuations in the amplitude of the cavity field, which induce dephasing via the AC Stark shift. Thus the Heisenberg uncertainty relations ensure that squeezing quantum noise to improve SNR will necessarily also produce greater measurement backaction due to the antisqueezed fluctuations in the conjugate variable, such that both measurement and dephasing speed up synchronously. Likewise, antisqueezing the noise in the signal quadrature slows the intracavity measurement process, reducing SNR while squeezing the amplitude fluctuations producing dephasing.

Absent any squeezing, stroboscopic measurement dephases the qubit at the rate $\Gamma_{\phi,\mathrm{vac}} = 8\bar{a}_0^2\chi^2/\kappa$ (note that our definition of $\bar{a}_0$ differs from that in [102] by a factor of 2). This expression includes a factor of $1/4$ corresponding to the variance of the intracavity field quadrature orthogonal to the signal, $\sigma_{\mathrm{BA}}^2 = 1/4$. Using a VNA we measure negligible loss inside the JPA, so we expect for modest gain the JPA outputs an ideal squeezed state characterized by N and $M = \sqrt{N(N+1)}$, which we infer from measurements of the squeezer gain and the relation $G_{\mathrm{SQZ}} = N + 1$ (eq. 3.19). Turning on the squeezer thus modifies σ_{BA}^2 according to $\sigma_{\mathrm{BA}}^2 = 1 + 2\epsilon_{\mathrm{in}}(N + M\cos 2\Phi)$, where the only unknown parameter is the input efficiency ϵ_{in}, which describes the the power loss $1 - \epsilon_{\mathrm{in}}$ between the squeezer output and the cavity.

Experimentally, we apply squeezing, Rabi drive, and strobe tones simultaneously, and choose the squeezer pump phase to align the squeezing angle Φ parallel ($\Phi = 0$) or perpen-

---

[2]The nomenclature is still applicable to, if perhaps overkill for, single-mode configurations similar to that used in our experiment. Yurke describes the single mode case as the limit of the more conventional two-mode case in which the interferometer arms are brought irresolvably close in space [106].
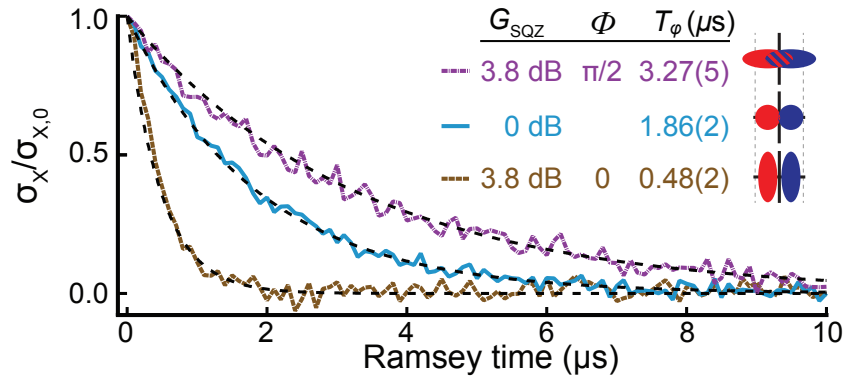
Figure 5.4: Ramsey decays during continuous measurements using injected squeezing. With no applied squeezing, the stroboscopic measurement dephases the qubit at a rate $\Gamma_\phi = 1/T_\phi = 0.54~\mu s^{-1}$. With the squeezer flux-pumped for 3.8 dB of phase-preserving gain as measured with a VNA, one choice of pump phase (brown, $\Phi = 0$) squeezes noise in the signal quadrature while amplifying the conjugate fluctuations which induce dephasing, increasing Γ_ϕ to 2.1 μs^{-1}. Choosing the orthogonal phase (purple, $\Phi = \pi/2$) has the opposite effect, slowing the intracavity measurement process and reducing Γ_ϕ to 0.31 μs^{-1}. For ease of comparison, each data trace has been normalized by its $t = 0$ value. Figure adapted from [4].

dicular ($\Phi = \pi/2$) to the signal, respectively speeding up or slowing down the production of qubit information in the cavity field. We form a Ramsey sequence by sandwiching this process between two $\pi/2$ qubit pulses followed by a projective dispersive readout pulse. The ensemble-averaged value of this readout as a function of the duration of the stroboscopic measurement is an exponential that decays at the dephasing rate Γ_ϕ. The three decays plotted in Fig. 5.4 respectively correspond to measurements performed with the same strobe drives and antisqueezed, unsqueezed, and squeezed noise along the signal quadrature. Fitting these decays, we infer that the antisqueezing reduces Γ_ϕ by a factor of 1.8 compared to its vacuum (unsqueezed) value.

We repeat these measurements for arbitrary squeezing angles Φ and at several values of G_{SQZ}, mapping out the dependence of measurement-induced dephasing on injected squeezing as shown in Fig. 5.5. The horizontal line indicates the dephasing rate with no squeezing applied, $\Gamma_{\phi,\text{vac}}$. We fit the data to the expression

$$
\begin{aligned}
\Gamma_\phi(\Phi) =& \Gamma_{\phi,\text{vac}} \frac{\sigma_{\text{BA}}^2}{1/4} = \Gamma_{\phi,\text{vac}}\left(1 + 2\epsilon_{\text{in}}(N + M\cos 2\Phi)\right) \\
=& \Gamma_{\phi,\text{vac}}\left(1 + 2\epsilon_{\text{in}}(G_{\text{SQZ}} - 1 + \sqrt{G_{\text{SQZ}}^2 - G_{\text{SQZ}}}\cos 2\Phi)\right),
\end{aligned}
\tag{5.2}
$$

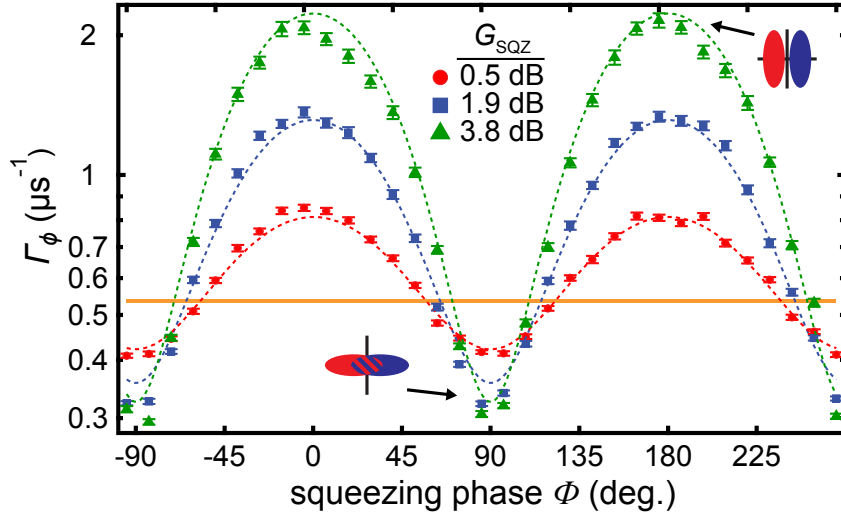from which we infer the input efficiency $\epsilon_{\text{in}} = 0.48$.

Figure 5.5: Measurement-induced dephasing rates as a function of input squeezing. The tan horizontal band indicates $\Gamma_{\phi,\text{vac}}$, the dephasing rate for a given stroboscopic measurement strength absent any applied squeezing. Increasing G_{SQZ} to with the measurement strength fixed causes Γ_ϕ to vary sinusoidally with the squeezing phase Φ. The data are fit to Eq. 5.2; the fit is performed jointly with the fit of the SNR phase-dependence data discussed in the next section. When $\Phi = n\pi$ with n an integer, the variance conjugate to the signal quadrature is amplified, increasing the dephasing rate and output field SNR. When $\Phi = (n + 1/2)\pi$, this backaction variance is minimized, and the dephasing rate and SNR are reduced. Figure adapted from [4].

5.5   Enhancing SNR

Speeding or slowing measurement-induced dephasing should respectively produce an increase or decrease in the SNR of the final measurement field digitized at room temperature. We determine the SNR by repeatedly preparing the qubit in either the ground or excited state and performing stroboscopic measurements. Each iteration of the measurement, we record the homodyne voltage for 2 μs, and then create ensemble histograms of the time-averaged homodyne voltages, which we use to generate the normalized plots in Fig. 5.6. The histograms are well described by Gaussian distributions, and exhibit reduced variance and overlap with applied squeezing. To determine the measurement rate Γ_{m}, we generate analogous histograms using variable-length subsets of the homodyne voltage records, and calculate the SNR $= (2(\bar{V}_e - \bar{V}_g)/(\sigma_e + \sigma_g))^2$ as a function of integration time. The representative examples shown in Fig. 5.7 are generated from the same data used to make Fig. 5.6. The linear model captures the time dependence reasonably well, though at long times there is some sub-linear behavior which is not fully understood and becomes more severe with

greater measurement strength. We calculate the measurement rate[3] from the slopes of these fits, $\Gamma_\mathrm{m} = \frac{1}{4}\mathrm{d}(\mathrm{SNR})/\mathrm{d}t$. Performing this analysis for data without squeezing determines the output efficiency $\epsilon_\mathrm{out} = \Gamma_\mathrm{m,vac}/2\Gamma_{\phi,\mathrm{vac}} = 0.38$.
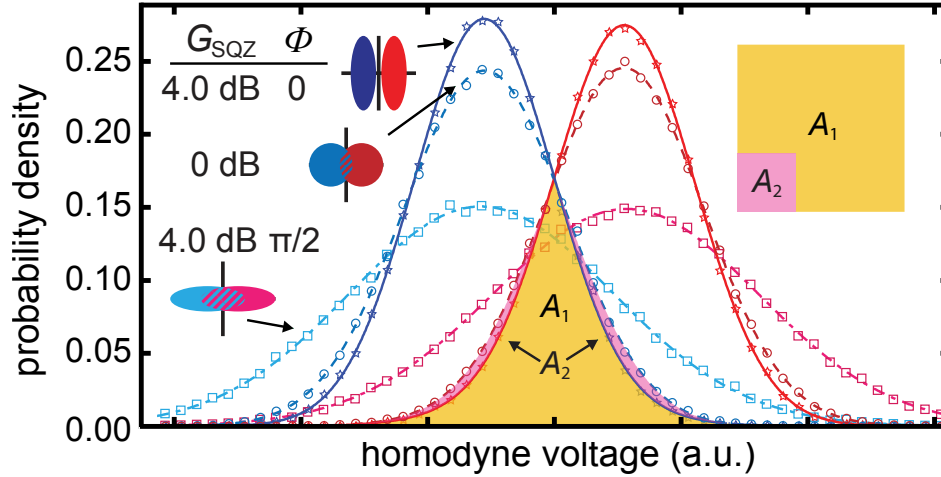
Figure 5.6: Measurement histograms with squeezing. The circles, squares, and stars indicate normalized histograms for measurements with unsqueezed, antisqueezed, and squeezed fields, with blues (left) indicating preparation in the ground state and reds (right) indicating preparation in the excited state. The curves are Gaussian fits; the histogram counts have been vertically scaled such that each fit integrates to 1. The squeezed Gaussians (solid) are narrower than the unsqueezed Gaussians (dashed). The area of overlap with squeezing (A_1, yellow) is reduced from that without squeezing ($A_1 + A_2$, yellow + pink). Figure adapted from [4].

As in the study of measurement backaction, we proceed to determine Γ_m under a range of input squeezing conditions for fixed stroboscopic drive strength, as plotted in Fig. 5.8. The data exhibit π-periodic variations with the squeezing angle Φ, with greater variation at higher values of G_SQZ. Near an optimal choice of Φ, we resolve a clear increase in Γ_m above the unsqueezed value, $\Gamma_\mathrm{m,vac}$, indicating a speed up of the measurement due to the applied squeezing. Varying the applied squeezing changes Γ_m by changing the variance of (noise in) the signal quadrature at the room-temperature detector, σ_m^2; we model this dependence as

$$\Gamma_\mathrm{m}(\Phi) = \Gamma_\mathrm{m,vac}\frac{1/4}{\sigma_\mathrm{m}^2} = \Gamma_\mathrm{m,vac}\Big(1 + 2\epsilon_\mathrm{in}\epsilon_\mathrm{out}(N - M\cos 2(\Phi + \delta))\Big)^{-1} \qquad (5.3)$$

---

[3]An alternate and perhaps more natural convention defines SNR, Γ_m, and η using different factors of 2, such that Γ_m is the decay rate of the histogram overlap region, and $\eta = \Gamma_\mathrm{m}/\Gamma_\phi$, which still ranges from 0 to 1 (see e.g. [108] and supplement).

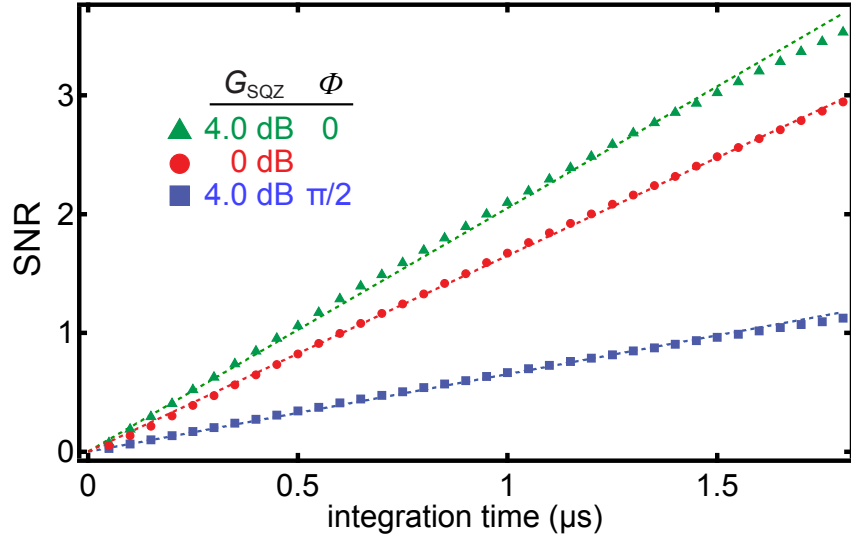Figure 5.7: Room-temperature ensemble-averaged SNR vs integration time for squeezed, unsqueezed, and antisqueezed stroboscopic measurements. Squeezing the noise in the signal quadrature causes the SNR to increase faster. Linear fits (dashed) estimate the measurement rate, $\Gamma_\mathrm{m} = \frac{1}{4}\mathrm{d}(\mathrm{SNR})/\mathrm{d}t$. With squeezing, Γ_m increases 24% from 0.41(1) to 0.51(1) $\mu\mathrm{s}^{-1}$. Figure adapted from [4].

In an ideal system, Γ_m and Γ_ϕ should both be maximal at the same value of Φ; however, we observe a small offset δ between the maxima. We attribute this offset to imperfect alignment of the stroboscopic signal quadrature to the amplification quadrature of the JPA downstream of the qubit, which shifts $\Gamma_\mathrm{m}(\Phi)$ but not $\Gamma_\phi(\Phi)$. We simultaneously fit Eqs. 5.2 and 5.3 to the results in Figs. 5.5 and 5.8, where the free parameters are $\epsilon_\mathrm{in} = 0.48$ as mentioned previously, a global phase, and the offset $\delta = 18°$.

5.6   Increasing measurement efficiency by squeezing

Comparing Γ_ϕ and Γ_m reveals that one can use input squeezing to trade off measurement speed to increase the overall measurement efficiency $\eta = \Gamma_\mathrm{m}/2\Gamma_\phi$, which ranges from 0 to 1. From one perspective, this is a surprising result, as squeezed states are notoriously susceptible to losses, such that using squeezing to make a signal more robust to losses seems counterintuitive. The result is made less surprising by noting that since the squeezed quadrature is more sensitive to loss, the antisqueezed quadrature should correspondingly be less sensitive to loss. Dividing $\Gamma_\mathrm{m}(\Phi)$ (Fig. 5.5) by $2\Gamma_\phi(\Phi)$ (Fig. 5.8) produces $\eta(\Phi)$, shown in Fig. 5.9. For a small amount of squeezing, a slight increase in $\eta(\Phi)$ is resolved above the value without squeezing, ϵ_out. This increase occurs near $\Phi = (n + 1/2)\pi$, corresponding to
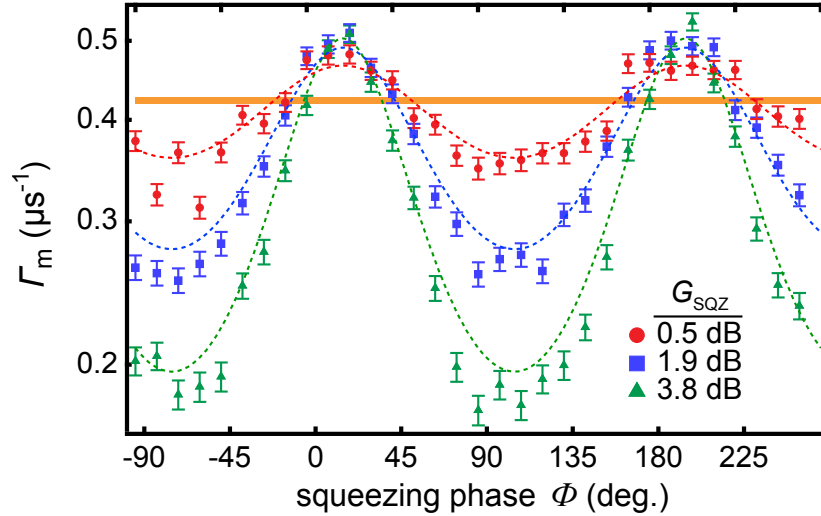
Figure 5.8: Measurement rate Γ_m as a function of input squeezing. This plot is the analog of
Fig. 5.5, but now the vertical axis is the measurement rate, related to the room-temperature
SNR, rather than the rate of on-chip backaction. The tan horizontal band indicates the
measurement rate with no injected squeezing, $\Gamma_{m,vac}$. For an optimal range of pump phases
near $\Phi = \delta \approx 0$ (see text), applying squeezing increases Γ_m above $\Gamma_{m,vac}$. The increase in
Γ_m saturates at modest values of G_{SQZ}, limited by the efficiencies ϵ_{in} and ϵ_{out}. Error bars,
including the width of the tan horizontal band, indicate statistical uncertainties in the values
of Γ_m determined by the linear fits of $SNR(t)$. The dashed curves result from a joint fit of
these estimates of $\Gamma_m(G_{SQZ}, \Phi)$ and those of $\Gamma_\phi(G_{SQZ}, \Phi)$ in Fig. 5.5 to Eqs. 5.3 and 5.2,
respectively. Figure adapted from [4].

injecting amplified fluctuations in the signal quadrature, slowing the measurement process,
indicating that η can be increased by sacrificing Γ_m. Likewise, using squeezing to increase Γ_m
tends to significantly decrease η. These trends can be understood by considering the effect of
loss on the signal and noise for unsqueezed, squeezed, and antisqueezed vacuum conditions.
In the unsqueezed case, when the field passes through an element with loss $1 - \epsilon_{out}$, the
signal power is reduced by a factor of $1 - \epsilon_{out}$ but the vacuum noise is unchanged before and
after the loss, reducing the SNR by the factor $1 - \epsilon_{out}$. In the case of antisqueezing along the
signal quadrature, the signal is reduced as before, but the noise is also attenuated, reducing
the drop in SNR such that $\eta > \epsilon_{out}$. In terms of squeezing parameters, and with $\epsilon_{in} = 1$ for
simplicity,

$$\eta = \frac{SNR'}{SNR} = \Big(\frac{(\langle V_g'\rangle - \langle V_e'\rangle)^2}{(\langle V_g\rangle - \langle V_e\rangle)^2}\Big)\Big(\frac{\sigma_m^2}{\sigma_m'^2}\Big) = \Big(\frac{\epsilon_{out}}{1}\Big)\Big(\frac{1/2 + N \pm M}{1/2 + \epsilon_{out}(N \pm M)}\Big), \qquad (5.4)$$

where primed quantities are downstream of the loss, and $\pm$ indicates antisqueezing or squeezing. In the limits of large antisqueezing ($N + M \to \infty$) or squeezing ($N - M \to -1/2$), $\eta \to 1$ or 0, respectively.

In essence, we have a glorified version of Friis's formula for the noise factor of cascaded amplifiers [109], here modified from the more standard microwave engineering expression to account for how losses at cryogenic temperatures couple vacuum noise into the channel, and allowing the first stage of noise amplification to occur upstream of the actual signal source. These modifications do not change the main implication: by raising the noise floor in a way that does not result in any lost information, here by injecting antisqueezed noise into the signal channel such that backaction is reduced proportionally, we reduce the effect of noise added downstream, increasing η. Similar effects have been realized previously, such as using squeezing to increase robustness of itinerant cat states [110] or to tap off power without degrading SNR [111, 112], though to our knowledge using input squeezing to increase superconducting qubit measurement efficiency has not been explicitly considered before. In the next chapter we revisit this idea but generate the antisqueezing inside the readout cavity such that $\epsilon_{\text{in}} \approx 1$, producing a more dramatic enhancement of η above ϵ_{out}.
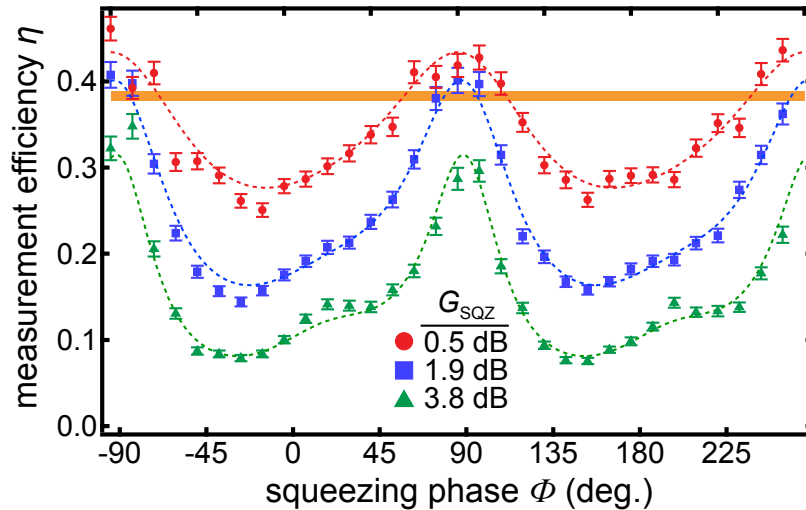

Figure 5.9: Measurement efficiency η as a function of input squeezing. Figure adapted from [4].

5.7 Conclusion and outlook

The results in this chapter demonstrate that squeezing can be used to improve the SNR of a qubit measurement and to slow dephasing induced by an applied measurement. Given the

challenges of working with squeezed fields and the corresponding scarcity of systems success-
fully measured with squeezing, plus the scientific importance of investigating the potential of
squeezing for developing superconducting quantum systems at scale, this work represents a
major accomplishment. However, significant improvements are needed before this approach
to squeezed readout can become competitive with standard dispersive techniques.

First, the measurement rates Γ_m demonstrated here ($\sim 0.5~\mu s^{-1}$) are much slower than
those that have been achieved with dispersive readout ($\sim 50~\mu s^{-1}$). This is not totally sur-
prising, as we designed the qubit-cavity system to study the effect of squeezing on dephasing
Γ_ϕ, only realizing *in medias res* that we might also be able to resolve an SNR improvement,
so the couplings χ and κ were not optimized for fast readout. Empirically, increasing the
stroboscopic drive strengths to try to increase Γ_m led to the appearance of population in
higher transmon energy levels, forfeiting the QND nature of the measurement. We suspect
this quantum demolition is driven by the parasitic terms of the measurement Hamiltonian
(Eq. 5.1), in which case the effect can be further suppressed by increasing Ω_R, enabling
faster measurement. Using large Ω_R may be facilitated by modern high-anharmonicity qubit
designs such as the C-shunt flux qubit [13]. However, greater Ω_R implies greater sideband
detuning, such that the input sideband amplitudes must be increased to appreciably drive
the cavity mode, which may be limited by heating of the input microwave line. Additional
work is needed to investigate the viability of this approach.

Second, losses must be reduced such that squeezing can have a worthwhile effect on Γ_m.
Currently, much more squeezing can be produced [28] than can be transported between
components. Even assuming perfect (infinite) squeezing inside the readout cavity, the mul-
tiplicative increase in Γ_m is bounded by $1/(1 - \epsilon_{out})$, here equal to 1.6. Superconducting
on-chip circulators or amplifiers [113, 114, 115, 116, 117, 118] are promising technologies
for significantly increasing ϵ_{in} and ϵ_{out}. In the following chapter we present an implementa-
tion of one such amplifier, the Qubit Parametric Amplifier (QPA), and investigate the new
measurement physics that arises when the qubit lives inside the squeezer.

Chapter 6

High-Efficiency Measurement of a Qubit Inside an Amplifier

6.1 Motivation

Recall that we can decompose the measurement process into two steps, the light-matter interaction which encodes qubit state information in the field of a microwave readout resonator, and the amplification of that information above the noise floor of our room temperature detector. In between these two steps, i.e. before the first stage of amplification, the itinerant information is extremely delicate, such that any multiplicative power loss L of the microwave field reduces the information content (SNR) by the same factor[1]. Modern efforts to reduce this pre-amplification loss by eliminating intermediary passive components typically plateau near $1 - L \approx 70\%$. Elimination of this information loss would increase qubit measurement rates (Γ_{m}) by 30%, facilitate experiments based on continuous-measurement dynamics including some quantum-feedback schemes, and improve the utility of measuring with a squeezed input field. Much of the loss can be attributed to the need for a microwave circulator, which is typically necessary between the qubit and the superconducting amplifier to protect the qubit from the high powers present at the amplifier. Inconveniently, the desired nonreciprocal behavior of a standard circulator derives from ferrite materials which also produce significant insertion loss. Circulators further draw the ire of experimentalists by taking up a lot of space, not only the size of the component but also a separation to prevent magnetic interaction of the ferrite with any superconducting devices[2]. Significant progress has been made recently in the development of lossless superconducting circulators and directional amplifiers [113, 114, 115, 116, 117, 118], though to our knowledge an improvement to qubit measurement efficiency, or simply any qubit measurement using such a circulator, is yet to be demonstrated. We also point out interesting work done recently investigating

---

[1]Or by more if measuring with a squeezed field.

[2]Magnetic interactions can be suppressed with proper shielding, though this too is often bulky, and also slow to cool at low temperatures.

possible operation without any circulators at all by briefly pulsing the cryogenic amplifier [119], though that work does indicate significant dephasing of the qubit state beyond that required by an ideal quantum measurement, and does not investigate measurement efficiency.

Here we develop a complementary technology, the integration of a standard JPA on-chip with the qubit, in which we perform the first stage of amplification on-chip, which eliminates virtually all pre-amplification loss. On-chip qubit-amplifier integration has been realized previously using several schemes such as [120, 121], in one case even including four multiplexed qubit-amplifier pairs on a single chip [122], yet to our knowledge none has demonstrated the near quantum-limited backaction required for high η_m. Similar experiments have characterized the backaction of a current-pumped amplifier on a qubit with no separate readout tone applied [123] or otherwise integrated the qubit to act as a probe of amplifier dynamics [124, 125]. JPAs have also been operated as magnetometers capable of providing on-chip gain [72, 126]. In this chapter we investigate theoretically and experimentally the measurement physics of a Qubit Parametric Amplifier (QPA), consisting of a JPA flux-pumped for parametric gain capacitively coupled to a qubit, and observe efficiencies of up to $\eta_m = 0.80$ with a clear direction for further improvement.

Due diligence: as of the time of writing, these results are somewhat recent and have yet to undergo peer-review; if by the time of reading a journal publication with these results has become available, it may provide a more complete or refined presentation.

6.2 QPA circuit overview

The QPA circuit is shown in Fig. 6.1, in which the photographs (b) have been false colored to match the schematic (a). The qubit (red) is dispersively coupled to a JPA (green) which acts as the readout cavity. A shorted section of coplanar waveguide (blue) is inductively coupled to a series array of two SQUIDs, allow flux-pumping of the JPA similar to the JPAs in previous chapters. With no pump applied, the system behaves identically to a standard cQED dispersive setup provided the intra-JPA field remains within the JPA harmonic region (Fig. 3.6). Flux-pumping amplifies the intra-cavity[3] field in a phase-sensitive manner.

The theory of QPA operation is the subject of Ben Levitan's masters thesis, [116], which is an excellent, very readable reference covering the subject in much greater detail than we can hope to in this chapter. A central result is that the total intra-cavity measurement process is the sum of two simultaneous processes, which we refer to as the beneficial measurement process and the parasitic measurement process. The beneficial process encodes $\hat{\sigma}_z$ information in the mean value of the cavity field via the usual dispersive interaction, modified somewhat by the phase-sensitive amplification. The parasitic process, on the other hand, encodes $\hat{\sigma}_z$ information in statistical properties of the output field noise fluctuations, primarily the orientation of the squeezing ellipse of the output field as determined by the covariance of the cavity-field quadratures. This process is parasitic as the information encoded in these noise fluctuations

---

[3]Here the generic term "cavity" is occasionally used in place of "QPA." In this context the two words are referring to the same resonator.
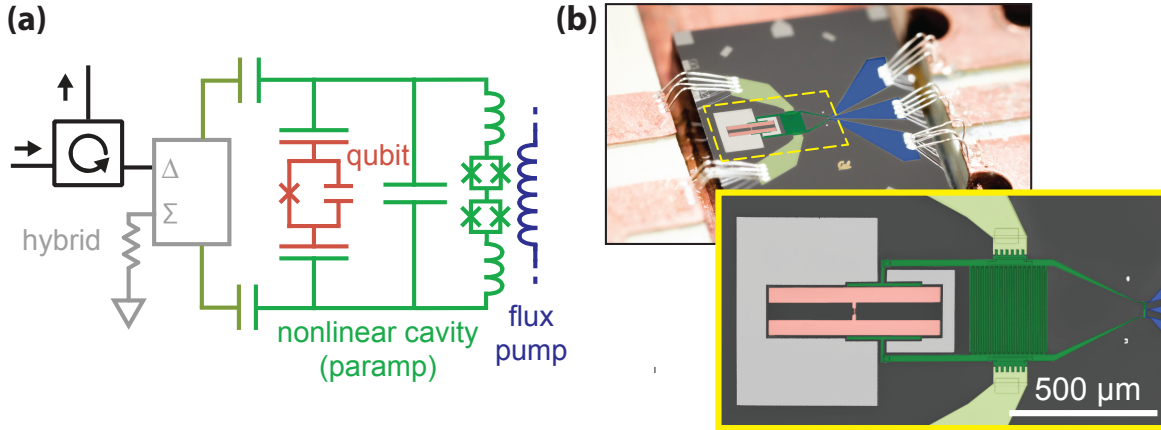
(a)

(b)

Figure 6.1: QPA circuit schematic and false-color photograph. The transmon qubit (red) is dispersively coupled to a differential JPA (green) connected to a transmission line via an off-chip 180° hybrid (gray in (a), not shown in (b)). With no pump applied, the JPA behaves like a linear readout resonator, permitting dispersive measurements using a readout pulse near the resonator frequency as in standard cQED. Applying a flux-pump via the coplanar waveguide (blue) at twice the readout frequency produces phase-sensitive amplification of the readout field. The circuit layout is designed to minimize direct crosstalk between the flux pump and qubit. A floating ground plane (gray in (b)) reduces dipole radiation of the qubit into uncontrolled environmental modes (T_1 increased from ~ 1 to $\sim 4 - 5$ μs).

is not readily detected by our measurement setup downstream, and thus increases qubit dephasing without contributing to the final SNR. Thus, for high $\eta_{\rm m}$, defined as in the previous chapter in terms of SNR ($\propto \Gamma_{\rm m}$) divided by backaction ($\propto \Gamma_\phi$), the parasitic backaction must be small compared to the total backaction, $\Gamma_{\phi,{\rm parasitic}} \ll \Gamma_\phi = \Gamma_{\phi,{\rm beneficial}} + \Gamma_{\phi,{\rm parasitic}}$. In the next two sections we will consider first the parasitic, then the beneficial measurement processes both theoretically and experimentally.

We characterize the QPA using the cryogenic setup shown schematically in Fig. 6.2. One port on the QPA connects the flux pump, while the other port allows for application of pulses for manipulating and measuring the qubit, respectively at $\omega_{\rm q}$ and $\omega_{\rm QPA}$. Measurement pulses reflect from the QPA and are amplified by the three amplifiers shown at right: a JPA in phase-sensitive mode, then a JTWPA, followed by a HEMT amplifier and additional amplification at room-temperature. As in the setup of the previous chapter, each amplifier ideally provides enough gain such that the noise added by the subsequent amplifier can be neglected. Though various operating conditions were explored, in a typical measurement the QPA is pumped for $G_{\rm QPA} \sim 3$ dB gain to mitigate the effect of losses before the JPA; the JPA is pumped for $G_{\rm JPA} \sim 6$–10 dB to overcome the half-photon of noise added by the phase-preserving JTWPA plus noise from additional inefficiency of the JTWPA; and the JTWPA
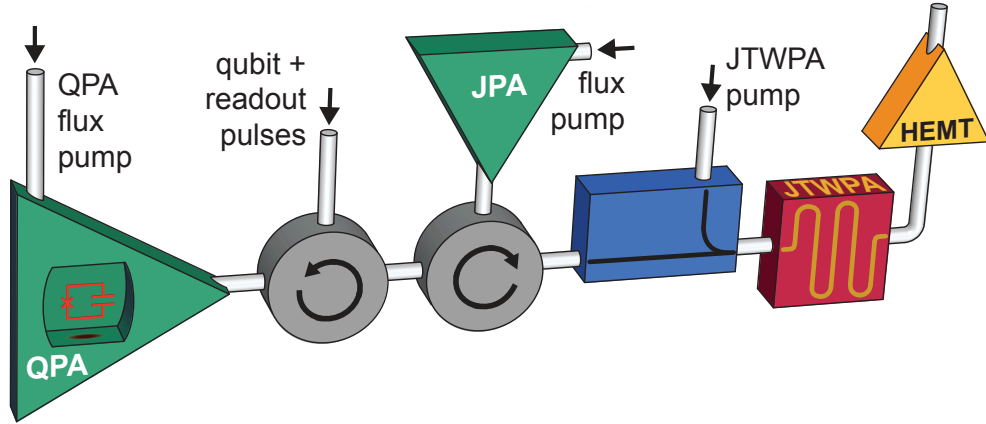
Figure 6.2: Simplified Qubit Parametric Amplifier (QPA) measurement setup. For most measurements involving on-chip gain, the QPA flux pump (left) is switched on several microseconds in advance, producing a squeezed field inside the QPA. Pulses for qubit control and readout are injected via the port indicated on the left circulator. The readout field reflects off the QPA, acquiring qubit state information while simultaneously undergoing phase-sensitive amplification. The QPA output field is further amplified by an off-chip JPA followed by a JTWPA and HEMT amplifier. Several passive components are omitted for simplicity; a more complete diagram appears in Appendix A.

was pumped for $G_{\mathrm{JTWPA}} \sim 15$ dB such that in total its output is above the noise-floor of the HEMT amplifier. Note that we follow the convention of previous chapters such that $G_{\mathrm{amplifier}}$ represents the phase-preserving gain as measured with a detuned vector network analyzer (VNA), so the actual signal-quadrature power gain of the JPA was closer to 10–16 dB. We found that about this much total gain was necessary to achieve high efficiency. This is roughly consistent with the results in [18], which included discussion that gains significantly greater than the 20 dB value commonly quoted in the cQED community were needed to make the noise added downstream truly negligible. A future setup would benefit from a higher dynamic range off-chip JPA, and probably one which is sideband current-pumped instead of flux-pumped to facilitate tunability, as these performance constraints indirectly ended up limiting the maximum efficiency achieved, as discussed further below.

6.3 Squeezing-induced dephasing

We first investigated the parasitic dephasing rate, $\Gamma_{\phi,\mathrm{parasitic}}$, as a function of on-chip gain. An effective heuristic model of the physics is that the phase-sensitive amplification produces squeezed vacuum inside the QPA at the readout frequency ω_{QPA}, and the interaction with the qubit rotates this squeezing in phase space depending on $\hat{\sigma}_{\mathrm{z}}$ per the standard disper-

sive interaction. This is an oversimplification, as in reality the amplification and rotation processes occur not in series but simultaneously, but it is a good working visualization for making qualitative predictions. The resulting rotation of the output squeezing ellipse carries qubit-state information away from the cavity, producing dephasing but not increasing the final SNR—hence the label parasitic.

A rigorous calculation shows the steady-state parasitic dephasing rate is

$$\Gamma_{\phi,\text{parasitic}} = \frac{1}{2}\,\text{Re}\left(\sqrt{D(-\lambda)} + \sqrt{D(\lambda)}\right) - \frac{\kappa}{2} + 1/T_2^*, \tag{6.1}$$

where $D(\lambda) = ((\kappa/2 + \lambda)^2 - \chi^2) + i\chi\kappa$, and where λ is the squeezing rate discussed following Eq. 3.5, related to the on-chip gain by Eq. 3.17, repeated here:

$$\lambda = \frac{\kappa}{2}\sqrt{\frac{\sqrt{G_{\text{QPA}}} - 1}{\sqrt{G_{\text{QPA}}} + 1}}. \tag{6.2}$$

Here T_2^* is an empirical parameter describing the dephasing of the qubit due to other environmental channels with neither pump nor measurement tones applied. The right-hand side of Eq. 6.1 goes to $1/T_2^*$ when $\lambda = 0$, and increases monotonically with λ.

The derivation of Eq. 6.1 is too involved to include here, but briefly it proceeds as follows. Starting from the Linblad master equation for the qubit-cavity system, including an applied coherent readout drive, one traces over the cavity to obtain the off-diagonal element representing the qubit coherence, calculates the time-derivative of that matrix element, then maps that differential equation onto phase-space (Wigner representation). The solution of this differential equation after this mapping is a Gaussian in phase-space, related to the overlap of the two possible output fields, which roughly represents the uncertainty of the total qubit state information that has left the cavity via the output field. Over time more information leaves via the output field and this uncertainty decreases; in the long-time limit[4], the exponential decay rate of this Gaussian (to conventional factors of 2) is given by Eq. 6.1, plus the effect of the applied readout drive ($\Gamma_{\phi,\text{beneficial}}$) discussed further below.

Significantly, Eq. 6.1 indicates that the parasitic dephasing is independent of the mean value of the cavity field; that is, $\Gamma_{\phi,\text{parasitic}}$ is the same whether or not the intra-cavity squeezed state is displaced. Thus we can determine $\Gamma_{\phi,\text{parasitic}}$ as a function of on-chip gain with no measurement tone applied, and expect it to be approximately unchanged when the measurement is turned on. We do this by observing Ramsey oscillations with the QPA pump on during the Ramsey evolution time[5]. Fig. 6.3(a-c) shows several example Ramsey traces for three values of G_{QPA}. The decay rate of one of these traces is $\Gamma_{\phi,\text{parasitic}}$ for that gain. Repeating this procedure for a range of gain values between 0 and 6 dB produces the dephasing rates shown in Fig. 6.3(d). The dashed curve is a plot of Eq. 6.1, to which we add

---

[4]The relevant timescale is $1/(\kappa - 2\sqrt{\lambda^2 - \chi^2})$; note this implies that transient ring-up effects can take longer to stabilize with on-chip gain.

[5]To allow the system to stabilize, we turn on the pump $\sim 1\,\mu$s in advance of the Ramsey sequence
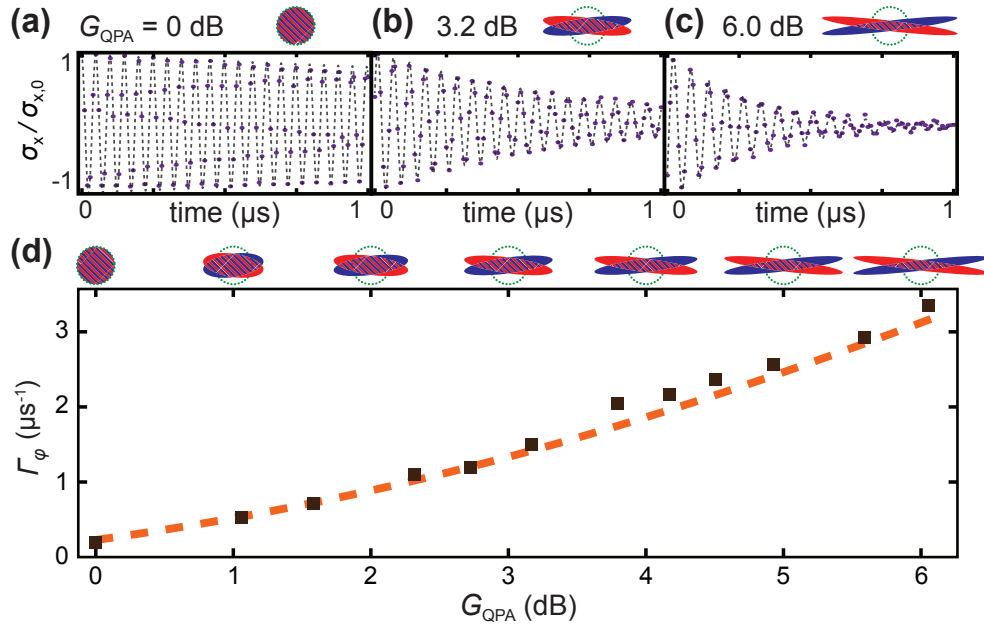
Figure 6.3: Qubit dephasing induced by locally-generated squeezed microwave vacuum. Ramsey decay traces are shown in (a-c) for varying amounts of on-chip gain, G_{QPA}. The QPA pump is turned on in advance such that on-chip gain occurs during the Ramsey evolution, though no coherent measurement drive is applied during that time. (a) With no on-chip gain, the output field is approximately independent of the state of the qubit (inset), and the qubit coherence decays at a rate $1/T_2^* = 0.23(7)$ μs^{-1}. (b) Increasing the on-chip gain to $G_{QPA} = 3.2$ dB produces a squeezed output field where the squeezing phase dependent on the qubit state (inset), and this parasitic measurement of the qubit causes faster dephasing. (c) Increasing the gain further reduces the overlap of the two possible output field ellipses (inset), corresponding to a stronger parasitic measurement and faster dephasing. (d) Repeated measurements exhibit good agreement with a zero free-parameter theory fit. All inset output fields are calculated from experimental parameters, though statistical moments beyond second order are not represented.

a small offset term capturing the dephasing rate of the qubit absent any applied squeezing, $1/T_2^*$. As χ, κ, G_{QPA}, and T_2^* are all readily determined using standard techniques, this curve includes no free parameters, yet still predicts the $\Gamma_{\phi,\text{parasitic}}$ values reasonably well, verifying the theoretical model for the device in this regime.

Moving back to the heuristic picture, we approximate the output field states conditioned on the ground or excited states of the qubit as two ellipses[6] that are both centered at the

---

[6]For convenience I will continue referencing and drawing ellipses, though the output field is actually not

origin but with different squeezing axes separated by an angle set by the standard dispersive rotation χ/κ. We analytically calculate the output field variances and covariance and use these to plot the squeezing-ellipses shown as insets to Fig. 6.3. Increasing λ stretches the Wigner functions away from the origin in different directions, reducing the area of overlap and thus increasing the dephasing.

Importantly, the values of $\Gamma_{\phi,\text{parasitic}}$ bound how quickly the coherent readout tone must measure the qubit in order to achieve high efficiency. For example, if $\Gamma_{\phi,\text{parasitic}} = 1 \ \mu\text{s}^{-1}$ at $G_{\text{QPA}} \approx 2$ dB, then if we apply a readout tone at this gain setting and observe a total dephasing rate $\Gamma_\phi = 10 \ \mu\text{s}^{-1}$, the efficiency will be limited at 90% even with zero noise added downstream of the QPA.

6.4 Measurement dephasing with on-chip gain

To verify the theory predictions for $\Gamma_{\phi,\text{beneficial}}$, described below, we next investigated the total backaction on the qubit produced by applying a readout tone simultaneous with on-chip gain. Because the readout tone is sourced by the same generator used to produce the QPA flux pump, the readout and pump are well phase-locked, and one can study how the measurement process depends on this relative phase. Mapping out this dependence of the measurement backaction on the pump-readout phase also provides a good means of aligning the on-chip amplification phase with the signal quadrature.

Three possible pumping conditions are shown in the three columns of Fig. 6.4. The applied readout power is kept constant across the three cases. The upper row depicts the approximate QPA output field calculated from equations in [116] using empirically determined parameters (non-Gaussian moments are not represented). In the first column, the QPA pump is left off ($G_{\text{QPA}} = 0$ dB), and the QPA behaves like a linear readout resonator in a standard cQED setup. The second column depicts "amplifier mode," in which the pump is turned on and the relative phase Φ chosen such that the signal quadrature Q is amplified while the I quadrature is deamplified. The third column depicts "squeezer mode," in which the orthogonal phase is chosen such that Q is deamplified and I amplified. In later sections we will focus on amplifier mode only, though it is informative and a useful diagnostic to probe the measurement backaction for both modes.

Below the output field cartoons are the corresponding Ramsey decays observed at these experimental conditions. Comparing amplifier and squeezer modes, we see that squeezer mode dephases the qubit faster. Since $\Gamma_{\phi,\text{parasitic}}$ does not depend on the relative pump-readout phase (Eq. 6.1), we conclude that $\Gamma_{\phi,\text{beneficial}}$ is greater in squeezer mode than in amplifier mode. This is consistent with the output field pictures: the red and blue pointer states are clearly better separated in squeezer mode, indicating a greater SNR at the output of the QPA and thus a faster dephasing of the qubit. In contrast, amplifier mode reduces the output-field SNR, resulting in slower dephasing than squeezer mode. For a sufficiently

---

quite Gaussian in this case, possessing non-zero kurtosis produced by the simultaneity of the amplification and rotation processes.
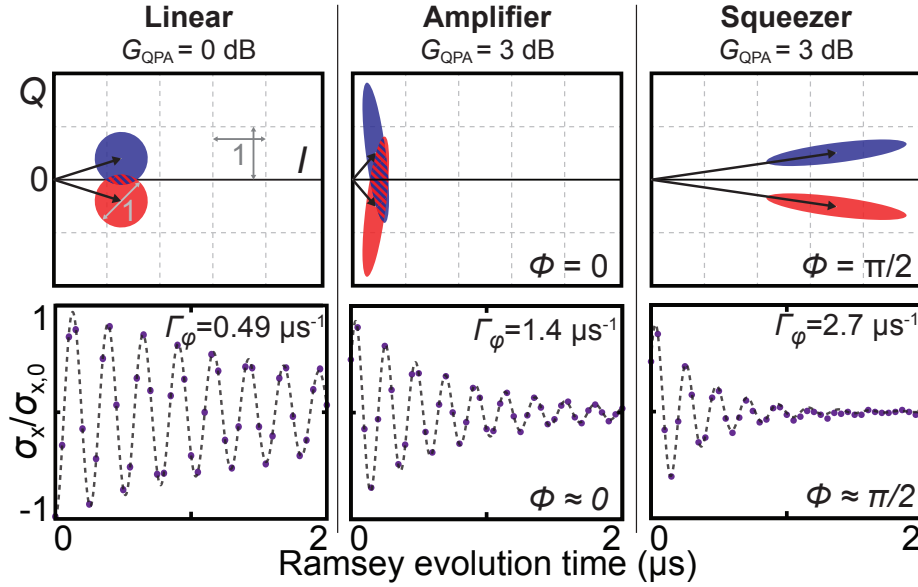
Figure 6.4: Qubit dephasing induced by an applied measurement tone concurrent with on-chip gain. The three columns represent operation with no pump applied (linear), a pump applied with the phase chosen such that the signal quadrature Q is amplified (amplifier mode), or a pump applied with the phase chosen such that Q is deamplified (squeezer mode). The power of the applied measurement tone P_{in} is fixed across the three columns (note this implies $\bar{n}$ is not fixed). The upper row indicates the analytically calculated output fields neglecting non-Gaussian features. The lower row displays Ramsey traces indicating dephasing rates for these approximate operating conditions.

strong measurement tone, such that $\Gamma_{\phi,\text{parasitic}}$ is relatively small, the dephasing in amplifier mode can also be slower than the dephasing with no pump applied.

There are at least two puzzling questions raised by Fig. 6.4 and the associated discussion: (1) Why is the output signal size the same in either squeezer mode or amplifier mode?, and (2) How can amplifier mode improve the overall efficiency if it decreases the output-field SNR?

Question (1) can be understood via the toy model presented in Fig. 6.5. In this simplified model we discretize the time dynamics into three steps: an amplification step, a qubit-measurement step, and another amplification step. Like the complete model, this toy model produces the same final signal size regardless of whether I or Q is the amplified quadrature. The takeaway is that in squeezer mode, the applied field drives the amplified quadrature, producing a very large displacement along I. Having this longer lever-arm cancels out the effect of deamplification along the signal quadrature Q. The reverse process happens
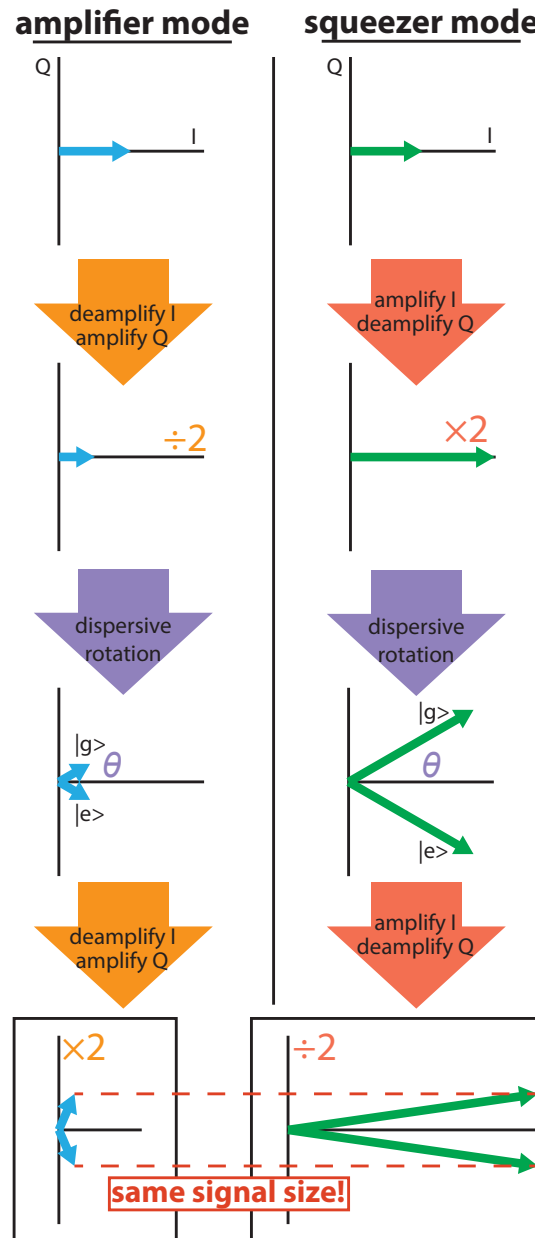
Figure 6.5: Toy model illustrating how the QPA signal gain can be the same in both amplifier and squeezer modes supposing a fixed input readout power. We artificially discretize the time dynamics into three steps: phase-sensitive amplification of the readout field that enters the QPA, rotation of this field per the dispersive qubit interaction, and then phase-sensitive amplification once more. This time discretization is artificial, since in the actual device the dispersive interaction and amplification processes occur simultaneously, but the complete theory still predicts equal signal gains for both squeezer and amplifier modes.

in amplifier mode, such that the net result is approximately unity[7] signal gain in both amplifier and squeezer modes. Bear in mind that, assuming no loss occurs in the QPA, the total efficiency of the measurement is independent of the signal size, depending only on the *change* in SNR between the QPA output and room temperature.

To answer question (2), we recall from the previous chapter that when we amplify the noise in the signal quadrature, we also squeeze the noise in the backaction quadrature, i.e. the amplitude fluctuations that produce dephasing via the Stark shift. Since $\eta_\mathrm{m} = \Gamma_\mathrm{m}/2\Gamma_\phi$, high η_m remains possible given a decreased output-field SNR provided the backaction on the qubit is decreased by the same factor. A central benefit of amplifier mode is that it increases the noise floor of the output signal quadrature; similar to the effect seen in Fig. 5.9, this makes the SNR insensitive to noise added downstream, increasing the overall efficiency. In contrast, squeezer mode lowers the noise floor of the QPA output signal quadrature, such that a larger fraction of the information content is lost due to the added noise, resulting in a lower efficiency.

Calculating the full measurement-induced dephasing rate for arbitrary pump-readout phase Φ gives [116]

$$\Gamma_\phi = \frac{2\chi^2\kappa^2 P_\mathrm{in}}{\hbar\omega_\mathrm{QPA}} \left(\frac{\cos^2\Phi}{|D(-\lambda)|^2} + \frac{\sin^2\Phi}{|D(\lambda)|^2} \right) + \Gamma_{\phi,\mathrm{parasitic}}, \tag{6.3}$$

where P_in is the power of the measurement tone incident to the QPA. The two Φ dependent terms are associated with $\hat{\sigma}_\mathrm{z}$ information being encoded in the amplified or deamplified field quadratures, respectively. Using a programmatic digital phase shifter (in combination with a spectrum analyzer to keep the power level), we record Ramsey decays for the full range of Φ values and for several values of on-chip gain, all at a fixed readout power P_in. The results are displayed in Fig. 6.6; this dataset includes the three Ramsey traces in 6.4. In order to compare these data to the predictions of Eq. 6.3, several additional measurements are performed to pin down parameters. Ramsey data taken with the QPA pump on but no applied readout tone determines $\Gamma_{\phi,\mathrm{parasitic}}$ for each gain used (colored horizontal dashed lines); Ramsey with the readout tone applied without any on-chip gain determines the incident readout power $P_\mathrm{in} = -141$ dBm; and Ramsey with no tones applied during the Ramsey evolution time determines T_2^* (black dashed line). Plotting Eq. 6.3 using these values produces the solid curves in the figure, exhibiting good agreement for most operating conditions. At larger G_QPA, modest disagreement is observed near $\Phi = \pm\pi/2$ corresponding to squeezer-mode; this is not terribly surprising, as the output-field depicted in Fig. 6.4 indicates that in squeezer mode the QPA field can become very large, and will eventually exceed the harmonic regime of the QPA (Fig. 3.6) and thus violate an assumption of the theoretical model. All subsequent measurements below are taken in amplifier mode ($\Phi = 0$), which permits the

---

[7]The prediction of unity signal gain is a slight inaccuracy of the toy model. In reality the amplification process is ongoing during the dispersive rotation, causing the signal size to be very slightly increased (essentially producing a small amount of phase preserving gain). This is visible if you closely study Fig. 6.4. This detail does not materially affect the discussions in this chapter.

use of much larger measurement powers P_{in} without violating this assumption of a harmonic potential[8].
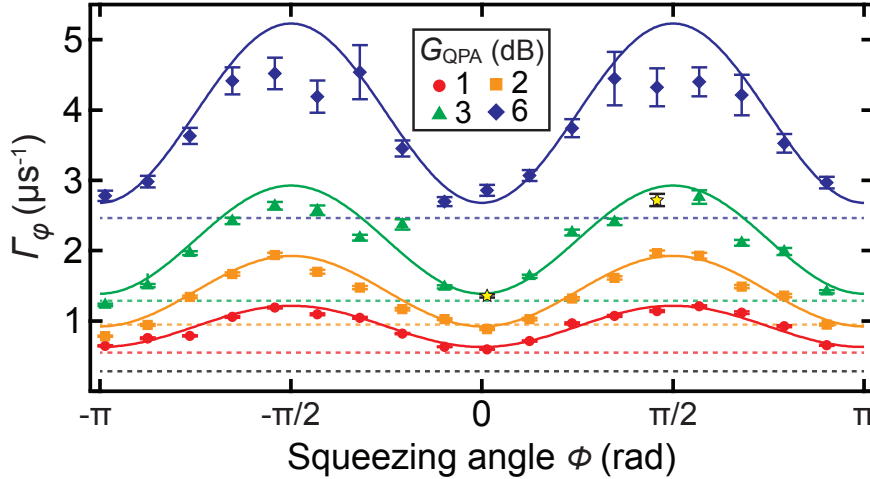

Figure 6.6: Measurement-induced dephasing of a qubit superposition inferred from Ramsey decay rates. The black horizontal dashed line indicates $\Gamma_\phi = 1/T_2^*$ with no measurement applied, while the color-coded dashed lines indicate $\Gamma_{\phi,\text{parasitic}}$ for the four G_{QPA} values. The data points indicate Γ_ϕ with a readout tone applied simultaneous with the on-chip gain. The two points marked with yellow stars correspond to the example Ramsey traces shown in Fig. 6.4, with amplifier mode occurring near $\Phi = 0$ and squeezer mode near $\Phi = \pi/2$. The data exhibit the expected π-periodicity, and agree well with the predictions of Eq. 6.3 for a range of operating conditions.

6.5 Measurement efficiency

Recall that, in the context of experiments utilizing continuous measurements (and given our chosen factor-of-two convention), a reasonable definition of the efficiency of a single-quadrature measurement is $\eta_{\text{m}} = \Gamma_{\text{m}}/2\Gamma_\phi$, with $\Gamma_{\text{m}} = \frac{1}{4}\text{d(SNR)}/\text{d}t$ and $\text{SNR} = (2(\bar{V}_e - \bar{V}_g)/(\sigma_e + \sigma_g))^2$ as introduced in the previous chapter. To determine η_{m}, we would like to determine Γ_{m} and Γ_ϕ for the same measurement process. To do this, we execute the pulse sequence represented in Fig. 6.7. As in the previous sections, we determine Γ_ϕ by varying the Ramsey evolution time and performing a projective readout after the second $\pi/2$ pulse, producing a Ramsey trace that can be fit to determine Γ_ϕ (right inset of figure). To determine

---

[8]This may equivalently be described as not exciting the self-Kerr nonlinearity of the cavity, or as keeping the current inside the QPA $\ll I_{\text{crit}}$ such that the nonlinear terms in the Josephson inductance remain negligible.

Γ_{m}, we additionally record the homodyne detection voltage between the two $\pi/2$ pulses; for
convenience we saved only the voltage record acquired during each execution of the sequence
with maximal time separation of the Ramsey pulses (here 500 ns). The time integrals of
these voltage records can be combined to produce histograms (left inset of figure) which can
be fit to calculate the final SNR. We are free to vary the limits on the time integrals in our
analysis code; varying the total integration time produces a series of histograms which we
fit to determine SNR as a function of integration time. Fitting a line determines the slope
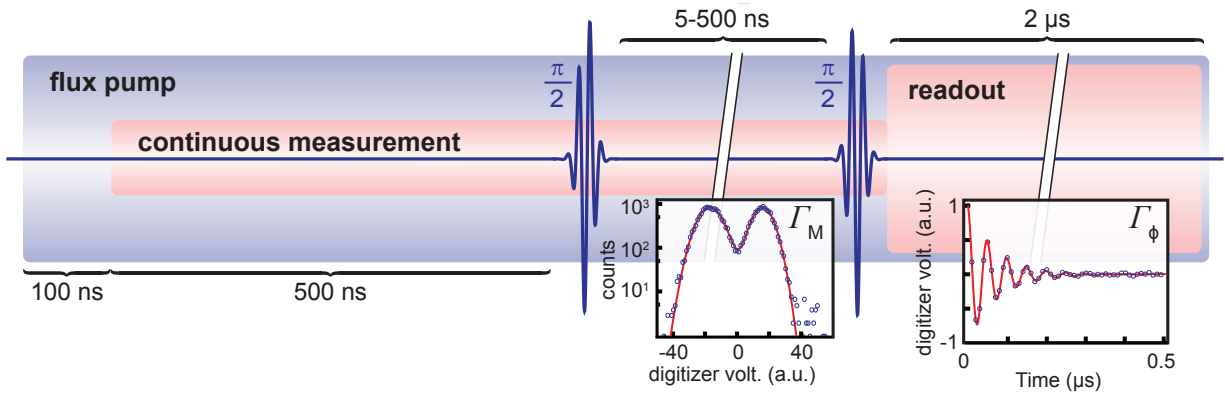of SNR(t), and thus also Γ_{m}.

Figure 6.7: Ramsey pulse sequence for efficiency measurements. The QPA flux-pump and
the continuous measurement tone are turned on well in advance of the first $\pi/2$ pulse, and
left on until after the second $\pi/2$ pulse. The homodyne voltages produced by integrating
between the two $\pi/2$ pulses in the ensemble of measurements performed are used to generate
histograms from which we infer Γ_{m}. An additional readout pulse performed after the second
$\pi/2$ pulse provides information on the dephasing rate Γ_{ϕ} during the measurement. The
measurement efficiency is determined by comparing these two rates.

This general procedure is rather standard, e.g. a similar procedure was used to generate
Fig. 5.8, though this project required additional care in a few aspects of the analysis.
First, as we restricted the scope of the project to studying efficiency in steady-state only,
i.e. after the applied measurement has finished "ringing-up" the QPA field, we followed the
usual practice of choosing the start-time of the time-integration to be after the ensemble-
mean instantaneous signal size $\langle V_{\mathrm{g}} - V_{\mathrm{e}} \rangle$ had stabilized; however, as this timescale depends
not only on κ but also on λ, care had to be taken to ensure this steady-state condition
was obtained even at the highest gain used. Second, we had to take care not to saturate
the dynamic range of any amplifiers in our measurement chain. We expect saturation to
compress larger amplitude fields, which we feared could skew the resulting histograms by
pulling one or both of the outside tails of the Gaussian distributions[9] towards the center,

---

[9]Theoretically the QPA output field does contain non-Gaussian features, though evidently the room-

leading Gaussian fits to produce an underestimate of the variances and thus an overestimate of η_m. This limited the readout power and amplifier gains that could be used. Third, although our qubit T_1 was about 9 times our voltage integration time, some T_1 decay events did occur during the integration, producing features that became increasingly apparent as the ground- and excited-state distributions became increasingly well separated. We consider these relaxation events to be dynamics of the system being measured and thus independent of the measurement operation such that they do not count against the measurement efficiency (the finite T_1 makes only a small contribution to Γ_ϕ during the measurement anyway), though a longer lived qubit would indeed improve measurement fidelity. However, the non-Gaussian features produced by these decays make it more difficult to detect amplifier compression. Thus we include the effect of these decays in our expression used to fit the histograms, using a slight generalization of the argument and expression given in Section III-A of [127]. Initially we allowed T_1 to be a free-parameter in these histogram fits, and saw the fit routine converge to the same T_1 value reported above that we had inferred from measuring the qubit population decay directly, leading us to fix T_1 in the histogram fit model for the efficiency measurements.

Our experimental procedure hit a snag in that the QPA and off-chip JPA behaved optimally at slightly different frequencies, yet needed to be operated at the same frequency for phase-sensitive amplification. Chronologically, we first noticed that by lowering our operating frequency from $\omega_\mathrm{QPA} = 6.74$ GHz to $\omega_\mathrm{QPA} = 6.7$ GHz, we could achieve greater off-chip gain G_QPA which produced a greater baseline efficiency $\eta_\mathrm{m} \approx 0.55$ before pumping the QPA for any on-chip gain. We took an efficiency dataset at this frequency for a range of measurement strengths and on-chip gain values. We observed that, while some regions of this parameter space exhibited histograms featuring a spurious third peak that we attributed to population being produced in the third transmon level (f-state), there was a well-behaved region in which high η_m was realized, presumably corresponding to drive conditions producing a lower mean photon number in the QPA field. (The photon number is monotonic in P_in but not in G_QPA). The inferred efficiency values are shown in Fig. 6.8. White asterisks indicate operating conditions at which f-state populations greater than 1% were observed. Despite this nonideal behavior, fitting the g and e peaks with our fit model still allowed us to infer nominal efficiency values for these conditions. The dashed yellow box indicates a region in which high efficiency simultaneous with low f state population were observed (see e.g. the histograms in Fig. 6.7, taken at $G_\mathrm{QPA} = 3$ dB and $|\alpha_\mathrm{in}| = 0.9$ (a.u.)); averaging results from this region to reduce random scatter leads us to report a final efficiency of $\eta = 80\%$.

After acquiring these data, we discovered that the parasitic dephasing rates $\Gamma_{\phi,\mathrm{parasitic}}(\lambda)$ at this operating frequency ($\omega_\mathrm{QPA} = 6.7$ GHz) observed with on-chip gain but no measurement tone applied are significantly greater than those observed at the original, higher operating frequency ($\omega_\mathrm{QPA} = 6.74$ GHz) shown in Fig. 6.3. We suspect that tuning the QPA down in frequency (to achieve optimal performance of the off-chip JPA) reduced the

---

temperature noise distributions were well-described by Gaussians for the operating regime of interest. At this time we have not analyzed this quantitatively.
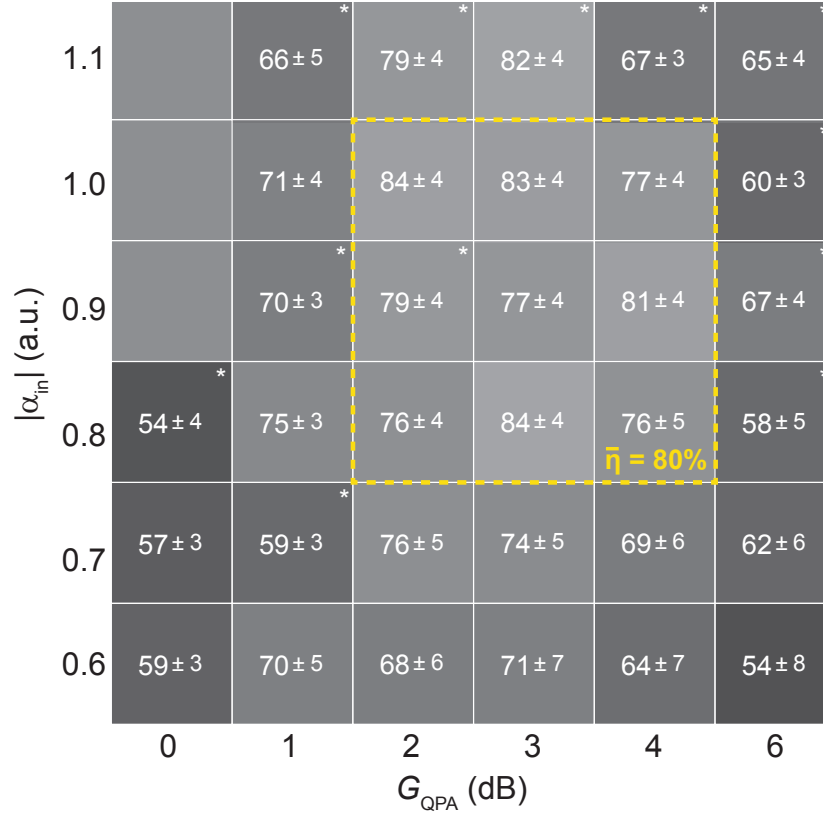
Figure 6.8: Measurement efficiency for varying amounts of on-chip gain (horizontal index) and applied measurement amplitude (vertical index). The vertical index is not calibrated to a power level at the device, and thus is indicated in arbitrary units. Asterisks indicate operating settings at which appreciable ($> 1\%$) population outside of the expected g and e histogram peaks were observed, which we attribute to f-state population produced by having a large intra-QPA photon number. The results corresponding to $G_{\mathrm{QPA}} = 3$ dB, $|\alpha_{\mathrm{in}}| = 0.9$ a.u. are displayed in the inset of Fig. 6.7. The system is fairly well behaved near this operating point; averaging the results in the indicated 3x3 square (yellow, dashed) to reduce random scatter gives $\eta = 80\%$. The three blank squares in the upper left indicate operating conditions at which the QPA was poorly behaved; this is not surprising, as the condition $G_{\mathrm{QPA}} = 0$ results in the largest intra-QPA field amplitudes.

QPA SQUID critical currents sufficiently to cause deviations from the theoretically predicted measurement interaction, moving away from the condition $\Gamma_{\phi,\mathrm{parasitic}} \ll \Gamma_{\phi,\mathrm{beneficial}}$ required for maximum efficiency, though we do not fully understand the behavior. Thus we expect with a different off-chip JPA, optimized for performance at the higher frequency 6.74 GHz to match the optimal QPA frequency, the total efficiency could be increased to 90% or more,

as supported by the plots in the next section.

6.6   On-chip and off-chip efficiencies

The overall measurement efficiency can be expressed as the product of the efficiency of the measurement process occurring on the chip, and the efficiency of the transfer of that information from the chip to room temperature; that is, $\eta_{\rm m} = \eta_{\rm on\text{-}chip}\eta_{\rm off\text{-}chip}$. Conveniently, $\eta_{\rm on\text{-}chip}$ can be estimated by looking only at Ramsey decay rates via the relation

$$\eta_{\rm on\text{-}chip} = \frac{\Gamma_{\phi,\rm beneficial}}{\Gamma_\phi} = 1 - \frac{\Gamma_{\phi,\rm parasitic}}{\Gamma_\phi}. \tag{6.4}$$

Experimentally, Γ_ϕ is the dephasing rate observed with both on-chip gain and an applied readout tone, while $\Gamma_{\phi,\rm parasitic}$ is the dephasing rate with only on-chip gain. This assumes again that $\Gamma_{\phi,\rm parasitic}$ is independent of the applied measurement tone, as predicted by the theory model. Given that $\Gamma_{\phi,\rm parasitic}$ is larger than predicted at this lower QPA operating frequency, it is not obvious a priori this is a safe assumption. Further, after calculating $\eta_{\rm on\text{-}chip}$, we can use the $\eta_{\rm m}$ values from the previous section to determine the effect of on-chip gain on $\eta_{\rm off\text{-}chip} = \eta_{\rm m}/\eta_{\rm on\text{-}chip}$. The inferred values of $\eta_{\rm on\text{-}chip}$ and $\eta_{\rm off\text{-}chip}$ are displayed in Fig. 6.9. When $G_{\rm QPA} = 0$ dB, we calculate that $\eta_{\rm on\text{-}chip} \approx 1$ since $\Gamma_{\phi,\rm parasitic} = 1/T_2^*$ is much smaller than Γ_ϕ. Qualitatively, we see that increasing the on-chip gain (vertical axes) causes additional parasitic dephasing resulting in lower $\eta_{\rm on\text{-}chip}$ for fixed readout power (horizontal axes, where $|\alpha_{\rm in}| \propto \sqrt{P_{\rm in}}$). Increasing the readout strength causes the inferred values of $\eta_{\rm on\text{-}chip}$ to increase as expected, since (we assume) $\Gamma_{\phi,\rm beneficial}$ becomes larger compared to the parasitic squeezing-induced dephasing. Division of η (Fig. 6.8) by $\eta_{\rm on\text{-}chip}$ (Fig. 6.9, left) provides an estimate of $\eta_{\rm off\text{-}chip}$, plotted in the right panel of Fig. 6.9. These values represent information loss downstream of the QPA and ideally should be independent of the measurement power used (horizontal axis), and indeed the values shown in the figure do not exhibit a clear dependence on $|\alpha_{\rm in}|$, at least within the random scatter of the results. Additional results were calculated for larger measurement strengths ($|\alpha_{\rm in}| = 1.1$ (a.u.), $G_{\rm JPA} = 6$ dB, and high-power measurements at $G_{\rm JPA} = 0$ dB), which did exhibit significant dependence on $|\alpha_{\rm in}|$. We attribute this to operating conditions driving large oscillations outside the harmonic regime of the QPA, such that by omitting these points we better restrict ourselves to the harmonic regime assumed by theory. The colored horizontal lines are simply the means of the values at each gain setting. This apparent flatness of the inferred values supports our assumption that $\Gamma_{\phi,\rm parasitic}$ is also independent of $|\alpha_{\rm in}|$. As expected, $\eta_{\rm off\text{-}chip}$ increases monotonically with $G_{\rm QPA}$, coming very close to unity for 4 dB of on-chip gain. While the lower-than-theoretically-predicted values of $\eta_{\rm on\text{-}chip}$ are somewhat disappointing, they also suggest that simply swapping out the off-chip JPA for a JPA optimized for a slightly higher frequency[10] is likely sufficient to achieve $\eta_{\rm m} \approx 90\%$ or more.

---

[10]It may even be sufficient to keep the same off-chip JPA, but sideband current-pump it, which provides greater tunability–though also introduces new potential for undesired device-device interactions.
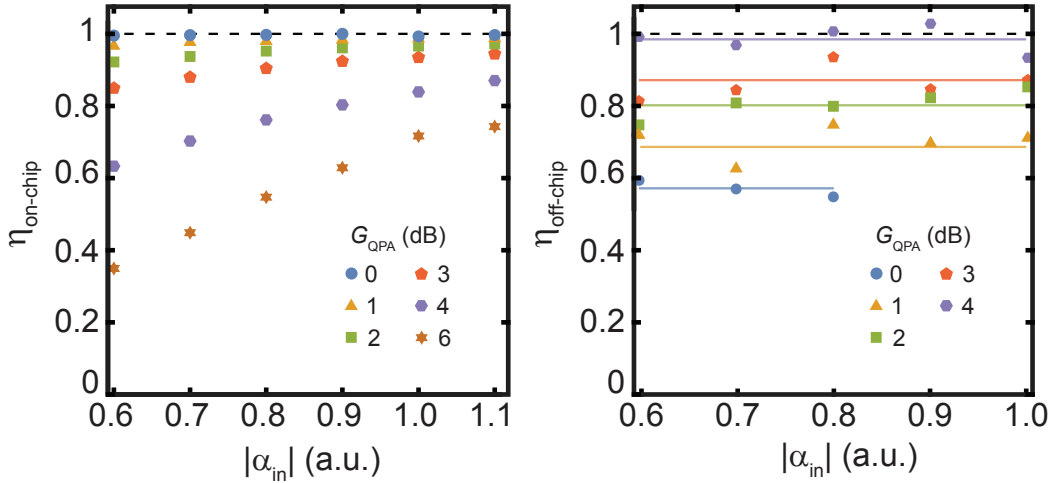
Figure 6.9: On-chip (left) and off-chip (right) efficiencies with on-chip gain.

6.7 Conclusion and outlook

In this chapter, we have presented what we believe is the first demonstration of SNR and backaction approaching the quantum limit in measurement of a superconducting qubit using an on-chip amplifier. Here we focused on using off-chip phase-sensitive amplification to maximize the possible total measurement efficiency, demonstrating the value of the QPA for continuous-measurement experiments, in which it is typically necessary to accurately track the evolution of the qubit state during the measurement. The limited scope of this work suggests a number of natural follow-up QPA experiments.

Although the on-chip gain does not significantly increase the output signal size for fixed P_{in} (Fig. 6.4 and 6.5), it does increase the signal size for fixed intra-QPA photon number $\bar{n}$, effectively increasing the maximum P_{in} that can be applied. A future investigation may determine whether this effect permits faster, or higher-fidelity, projective readout with the QPA than can be achieved with a passive readout resonator vis-a-vis limitations on photon number imposed by the dispersive interaction.

A second experiment—surely a challenging one—would be to perform stroboscopic readout in the QPA, or to realize a longitudinal qubit-resonator interaction via some other means. In Chapter 5, stroboscopic readout was used to eliminate rotation of squeezing ellipses that reduced the achievable SNR. In the current chapter, rotation of squeezing ellipses produced the parasitic dephasing $\Gamma_{\phi,\text{parasitic}}$, making high η_{m} difficult to achieve. Beyond the known limitations of stroboscopic readout as it exists now—stroboscopic readout is relatively slow, and difficult to stabilize—it may be especially difficult to perform stroboscopic readout in a QPA: first, if the stroboscopic probe tones are large enough, they may act to sideband current-pump the QPA, producing undesired nonlinear dynamics (though in principle this

may be addressed by boosting the QPA dynamic range with more SQUIDs); second, we have
not analyzed how the stroboscopic light-matter dynamics are modified by on-chip phase-
sensitive gain. If it can be done, however, the rotation of the squeezed output field and the
associated $\Gamma_{\phi,\text{parasitic}}$ can be made very small, enabling greater η_m. Alternatively, performing
this experiment with the QPA operated in squeezer mode may allow effectively for a repeat
of the experiment in Chapter 5 but with the advantage that $\epsilon_\text{in} \approx 1$ since the squeezing is
generated locally in the readout resonator.

As the QPA adds only modest additional superconducting circuitry compared to a passive
readout resonator, it should also be possible to integrate the QPA into modern multi-qubit
architectures, with many QPAs coupled to a common readout bus leading to frequency-
multiplexed amplification in a JTWPA. Though routing the flux-pump power appropriately
to all the QPAs presents an engineering challenge, such a system would allow efficient readout
of multiple qubits on the same chip.

Bigger-picture, forecasting the ultimate utility of the measurement techniques demon-
strated in this thesis is difficult. My personal guess is that, given the substantial improve-
ments in measurement capability provided by the recent development of the JTWPA and of
very high-performance JPAs, for many applications and target milestones in the immediate
future measurement will not be the limiting process, and other aspects of quantum processors
will have to improve significantly before advanced techniques such as readout using squeezed
microwaves become worth the added technical complexity. However, it does seem very plau-
sible that such a time will eventually arrive assuming efforts towards quantum computing
continue to make progress, so it is important to explore the potential of these techniques in
advance. Moreover, with on-chip integration of superconducting circulators poised to dra-
matically reduce transmission losses and thus dramatically increase the benefits of applied
squeezing, the calculus may change such that applications of microwave squeezing become
valuable for quantum information processing at-scale in the near future.

Appendix A

Wiring diagrams

The following pages contain detailed wiring diagrams and technical commentary thereof for several experimental setups utilized for this thesis. It should be noted that these diagrams provide only upper-bounds on hardware requirements; it is likely that some number of precautionary room-temperature components—namely filters and isolators—may be removed without appreciable performance degradation.

A.1 Resonance fluorescence in squeezed vacuum

Flux pump – To ensure phase coherence of the Rabi drive and the microwave squeezing, the flux-pump and Rabi drive are sourced by the same microwave generator. A Marki amplifying-doubler is used to upconvert the flux-pump from 7.3 GHz to 14.6 GHz. A Hittite switch and Hittite voltage-variable attenuator are used to programmatically control the JPA pump power and thus the JPA gain. Flux-pumping often requires a lot of power relative to other cryogenic drives, so an additional amplifier (Minicircuits ZVA-183-S+) at room temperature further boosts the pump after frequency-doubling, and the cryogenic line is only lightly attenuated. Leakage of the fundamental tone through the doubler is blocked by bandpass filters (Marki 1450) at room temperature and at the lowest temperature stage; in retrospect this may be excessive as these filters are both pricey and very effective but having at least one (preferably at cryo to block thermal noise at the near ω_c) is essential to avoid inadvertently driving the qubit-cavity resonance. Likewise, a low-pass filter (K&L 10 GHz cleanup filter 6L250-00088; for this filter series make sure the cutoff is > 2 GHz below the pump) is needed to prevent any flux-pump power from reaching the JTWPA; without this filter the JTWPA gain was observed to change significantly as the JPA pump was modified. Our qubit-cavity fortunately did not respond to this flux-pump leakage; if it had, it would have been necessary to move the low-pass filter between the JPA and circulator, which would have reduced the transfer efficiency η. Finally, in more recent setups we have observed some instability of JPA bias frequencies, which was resolved by putting an inner-outer dc block on the flux-pump line as close as possible to the JPA (note that these tend to thermally
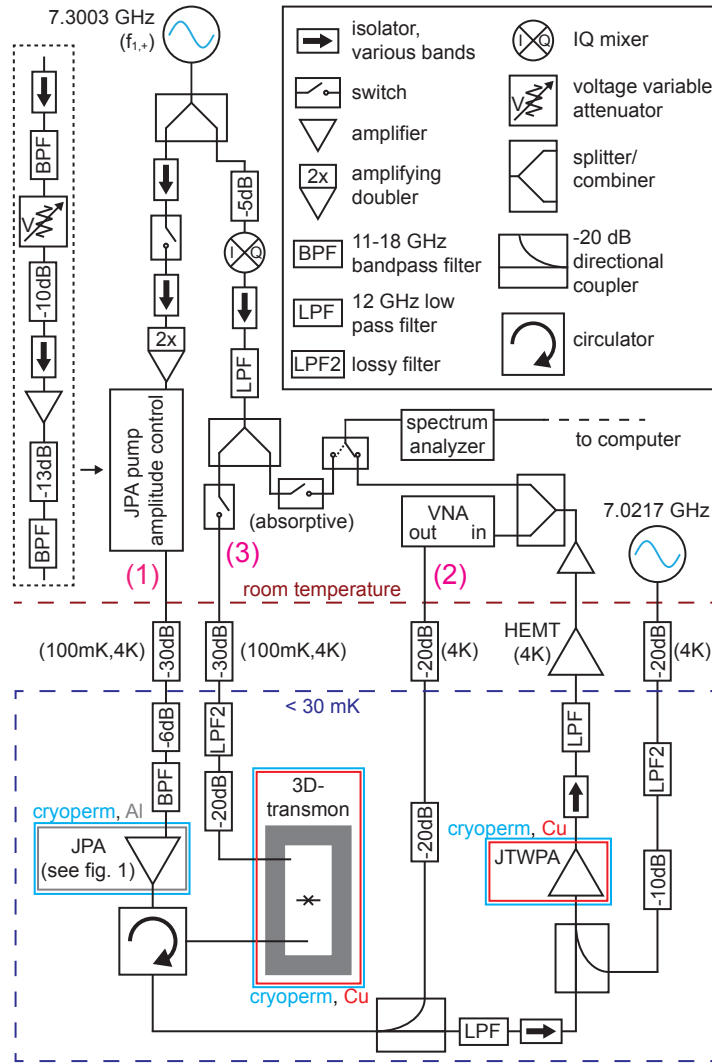
Figure A.1: Detailed setup for measuring resonance fluorescence in squeezed vacuum. There are four microwave inputs to the refrigerator: one for flux-pumping the JPA to generate squeezing (1), one for probing the JPA gain using a vector network analyzer (2), one for driving the weakly-coupled cavity port (3), and one for pumping the JTWPA.

isolate as well). The motivating hypothesis, found to be consistent with observation, was that connecting separate lines to both ends of the device created a large, destabilizing ground loop.

Rabi drive – To ensure phase-coherence with the flux-pump, the Rabi drive is produced by the same generator (Agilent PSG series). We step dc offsets applied to the IF ports of a Marki IQ mixer to programmatically control the phase and amplitude of the Rabi drive. We

first find the dc levels which minimize (null) the power out of the mixer, then rotate about that point in 2d voltage-space. To better ensure power-flatness as the phase is rotated, we use a series of switches to measure the Rabi drive power each time the phase is stepped. In principle the relative phase could also be adjusted by changing the phase of the flux-pump, and indeed we have done this for other projects when necessary, but this has the negative side effect of increased sensitivity to small variations in power as the phase is rotated due to the JPA necessarily operating near a critical point.

Qubit-cavity implementation – The qubit was a conventional aluminum single-junction 3D-transmon deposited via electron-beam evaporation on double-side polished silicon. The characteristic energies of the device were inferred to be $E_c/h = 200$ MHz and $E_J/h = 33.1$ GHz, corresponding to a fundamental frequency $\omega_q = 7.091$ GHz. To bring the qubit and cavity near resonance, the frequency of the aluminum cavity was adjusted downwards to 7.1051 GHz by introducing additional silicon chips as a dielectric (simulated in Microwave Office, though frankly empirical trial-and-error is a practical alternative); the 14 MHz residual detuning was primarily due to aging of the qubit between experimental cycles. We performed two-tone spectroscopy to determine the $|0\rangle \rightarrow |1, +\rangle$ transition frequency of 7.3003 GHz, the qubit-cavity coupling $g/2\pi = 202$ MHz, and the nearest neighboring transition frequency $|1, +\rangle \rightarrow |2, +\rangle$ at 7.262 GHz. To avoid driving this neighboring transition, the JPA was designed to have a single-side bandwidth smaller than this 38 MHz detuning. The qubit-cavity system was mounted on a cold-finger inside a light-tight gold-plated OFHC copper can (see [3] for an image of the can).

A.2 Stroboscopic qubit measurement with squeezed illumination

Getting this setup to behave was one of the hard parts of the Ph.D., despite the setup being a near replica of that developed in our lab for [102]. That statement merits some contemplation when considering a follow-up experiment, and in my opinion strongly motivates the development of qubit/cavity designs with hardwired longitudinal coupling if possible. Here most of the complexity is associated with generating the stroboscopic measurement; applying the squeezing is, by comparison, straightforward.

Flux pumps – In the resonance fluorescence setup (Fig. A.1), we kept the phase of the squeezer flux-pump fixed while varying the phase of the Rabi drive using an IQ mixer. Here we instead phase shift the squeezer flux-pump directly rather to minimize complexity of the already complex measurement line (the phase shifter would have to go just before the four-way splitter). We achieve this programmatically using a Vaunix 802 digital phase shifter which has a nominal 1 degree resolution. As the insertion loss of the phase shifter is not perfectly flat vs phase, we sample the pump power using a spectrum analyzer each time we change the phase, and feed back on these measurements using the voltage-variable attenuator. The flux pump for the second JPA, which acts as the phase-sensitive preamplifier,

does not require frequent phase adjustments so a manual phase-shifter and manual variable attenuator are used on that line. Leakage of flux-pump power out the signal port of either JPA is significant, and must either be filtered or cancelled. Filters (K&L 10 GHz "cleanup" low pass filter) are convenient but add insertion loss which reduces efficiency. We used a filter to block all leakage from the squeezer pump, used a phase-locked cancellation tone to cancel leakage from the preamplifier at the qubit, and used another filter to prevent preamplifier pump leakage from reaching the JTWPA. The amplitude and phase of the cancellation tone can be deterministically calibrated as follows. First, pump the JPA with the cancellation line disconnected and perform a Ramsey measurement to determine the Stark shift on the qubit. Next, disconnect the JPA pump line, connect the cancellation line, and adjust the cancellation tone power to produce the same Stark shift. Finally, reconnect the pump line and adjust the cancellation phase to minimize the Stark shift. Barring extreme instability of the ambient room temperature, this only needs to be set once.

Qubit drive – It is important to account for the Stark shift on the qubit produced by the strobe tones and by the squeezed noise power itself. The Stark shifts can be determined by standard Ramsey measurements. Our qubit also exhibited intermittent fluctuations in its resonance frequency that we attribute to a larger-than-ideal anharmonicity, which produced a slow beating in the Ramsey traces ($\gtrsim 15~\mu$s) and made some calibration processes more challenging. One central challenge was keeping Rabi frequency Ω_R, which is set by the Rabi drive amplitude, precisely equal to the 40 MHz strobe sideband detuning. This was done by interleaving measurements of Rabi oscillations with all other data acquisition and using the inferred Ω_R values to feed back on the drive amplitude.

Strobe pulse generation – The strobe sidebands were generated via a 40 MHz modulation applied to a carrier tone at ω_c via an IQ mixer. A Minicircuits voltage-controlled phase-shifter was used to phase shift the input to I relative to the input to Q, which can be used to adjust the relative amplitudes of the resultant sidebands. The stroboscopic measurement requires that the two sidebands drive the cavity field equally. For the qubit Rabi driven about $\hat{\sigma}_x$, an imbalance in the amplitudes produce an effective cooling of the qubit state towards $|\hat{\sigma}_x = \pm 1\rangle$. We perform additional tomographic measurements to feed back on and zero this cooling process, thereby balancing the sideband amplitudes at the cavity.

A.3 High-Efficiency Measurement of an Artificial Atom inside a Parametric Amplifier

In many ways the setup is similar to a standard configuration for dispersive measurement. Pulses for qubit manipulation and readout are produced at the qubit and QPA frequencies, respectively, and sent into the dilution refrigerator via the left-most microwave line in (a). Readout pulses reflect off the QPA (containing the qubit), are amplified at the JPA, travel through the JTWPA followed by the HEMT amplifier, and are detected via homodyne demodulation. However there are a number of idiosyncrasies.
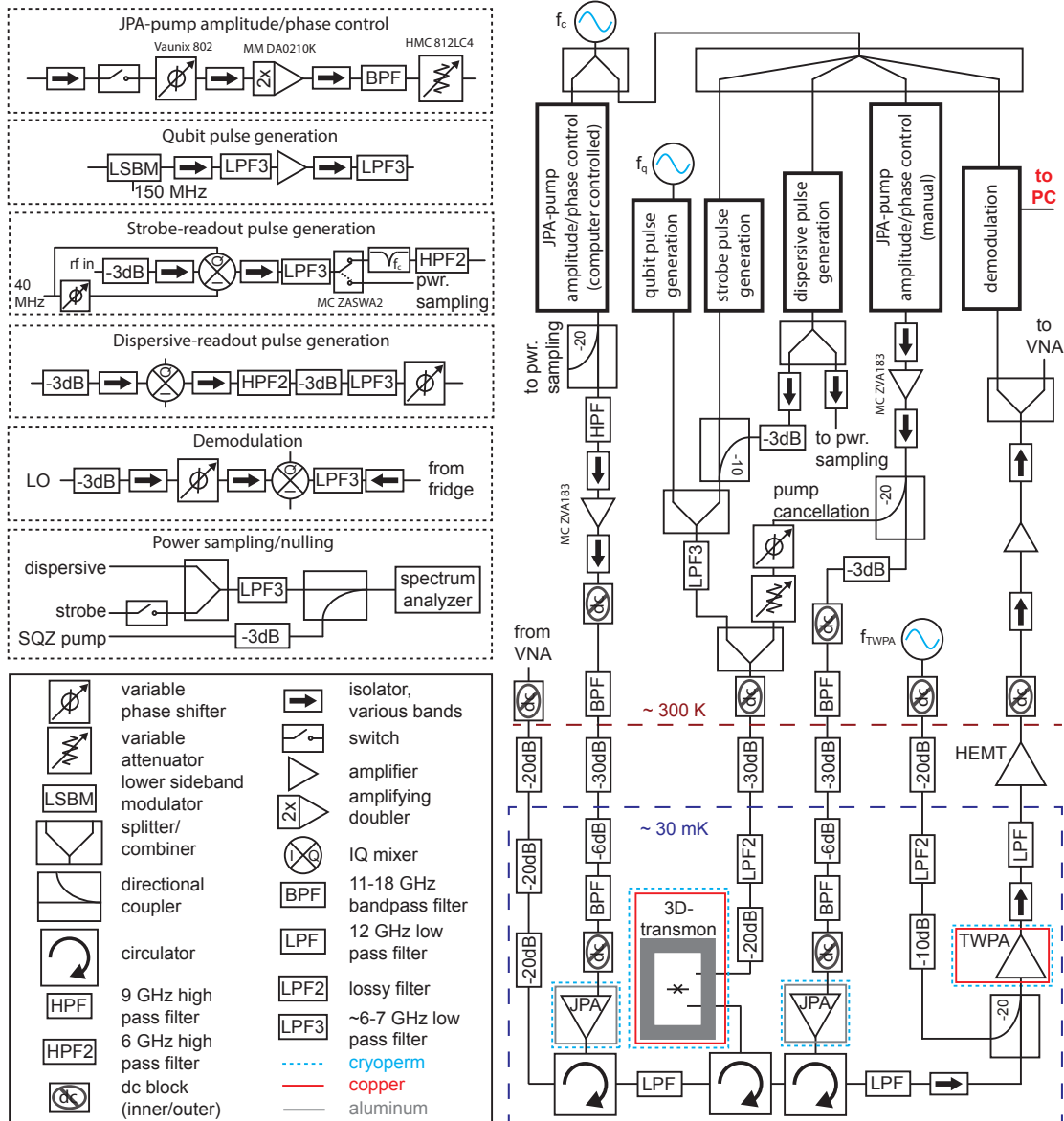
Figure A.2: Detailed setup for stroboscopic qubit measurement with input squeezing.

As in the stroboscopic-measurement experiment, low-pass filters were necessary between all superconducting amplifiers to block flux-pump leakage from producing significant amp-amp crosstalk, especially with regard to the JTWPA. Also as in that experiment, one flux-pump line (that of the QPA) had computer-controlled amplitude and phase control, allowing us to scan over both QPA phase and gain, while the other pump line was only manually controlled, as the off-chip JPA needed to be set only once assuming negligible thermal drift. During final data runs, we turned off the air-conditioning in the lab several hours in advance to further reduce this and other drifts.

As JPAs are pumped near a critical point, they are sensitive to small variations in pump power. The QPA pump power was programmatically varied using a voltage-variable atten-uator, and sampled using a spectrum analyzer to ensure power flatness as the phase was adjusted. To ensure power flatness of the off-chip JPA pump, we did not put a phase shifter on that pump line, instead putting a manual phase shifter before the four-way splitter sourc-ing all other phase-locked tones. This provided a means of effectively controlling the pump phase of the JPA without introducing any variation in the pump power. The ~ 0.2 dB variation of the input to the four-way splitter did not significantly affect the demodulation performance, and was actively compensated for on the readout and QPA-pump inputs using a spectrum analyzer.
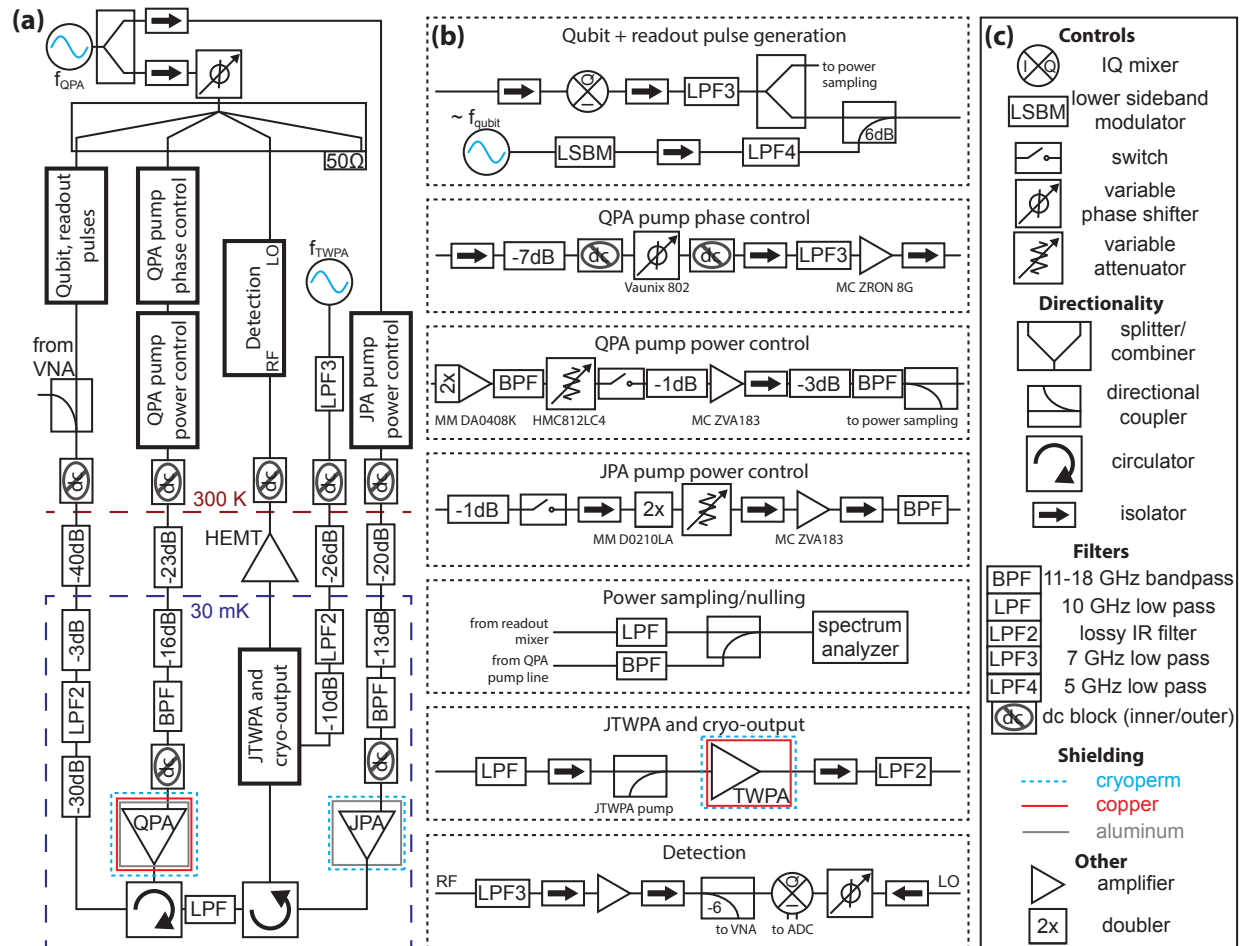
Figure A.3: Detailed setup for measurements of the qubit parametric amplifier (QPA). The three columns present (a) an overview of the complete experimental setup, (b) subsystem details, and (c) a legend of symbols used.

Bibliography

[1]   D. M. Toyli et al. "Resonance Fluorescence from an Artificial Atom in Squeezed Vacuum". In: *Physical Review X* 6.3 (July 2016), p. 031004. URL: `http://link.aps.org/doi/10.1103/PhysRevX.6.031004`.

[2]   Samuel Boutin et al. "Effect of Higher-Order Nonlinearities on Amplification and Squeezing in Josephson Parametric Amplifiers". In: *Physical Review Applied* 8.5 (Nov. 2017), p. 054030. URL: `https://link.aps.org/doi/10.1103/PhysRevApplied.8.054030`.

[3]   N. Roch et al. "Observation of Measurement-Induced Entanglement and Quantum Trajectories of Remote Superconducting Qubits". In: *Physical Review Letters* 112.17 (Apr. 2014), p. 170501. URL: `https://link.aps.org/doi/10.1103/PhysRevLett.112.170501`.

[4]   Andrew Eddins et al. "Stroboscopic qubit measurement with squeezed illumination". In: (Aug. 2017). URL: `http://arxiv.org/abs/1708.01674`.

[5]   Peter W. Shor. "Polynomial-Time Algorithms for Prime Factorization and Discrete Logarithms on a Quantum Computer". In: *SIAM Journal on Computing* 26.5 (Oct. 1997), pp. 1484–1509. URL: `http://epubs.siam.org/doi/10.1137/S0097539795293172`.

[6]   L K Grover. "A fast quantum mechanical algorithm for database search". In: *Proceedings of the twenty-eighth annual ACM symposium on Theory of computing - STOC '96*. New York, New York, USA: ACM Press, 1996, pp. 212–219. URL: `http://portal.acm.org/citation.cfm?doid=237814.237866`.

[7]   P. J. J. O'Malley et al. "Scalable Quantum Simulation of Molecular Energies". In: *Physical Review X* 6.3 (July 2016), p. 031007. URL: `https://link.aps.org/doi/10.1103/PhysRevX.6.031007`.

[8]   Abhinav Kandala et al. "Hardware-efficient variational quantum eigensolver for small molecules and quantum magnets". In: *Nature* 549.7671 (Sept. 2017), pp. 242–246. URL: `http://www.nature.com/doifinder/10.1038/nature23879`.

[9]   James I. Colless et al. "Robust determination of molecular spectra on a quantum processor". In: (July 2017). URL: `http://arxiv.org/abs/1707.06408`.

[10] Y. Nakamura, Yu. A. Pashkin, and J. S. Tsai. "Coherent control of macroscopic quantum states in a single-Cooper-pair box". In: *Nature* 398.6730 (Apr. 1999), pp. 786–788. URL: http://www.nature.com/doifinder/10.1038/19718.

[11] R. Barends et al. "Coherent Josephson Qubit Suitable for Scalable Quantum Integrated Circuits". In: *Physical Review Letters* 111.8 (Aug. 2013), p. 080502. URL: https://link.aps.org/doi/10.1103/PhysRevLett.111.080502.

[12] C. Wang et al. "Surface participation and dielectric loss in superconducting qubits". In: *Applied Physics Letters* 107.16 (Oct. 2015), p. 162601. URL: http://aip.scitation.org/doi/10.1063/1.4934486.

[13] Fei Yan et al. "The flux qubit revisited to enhance coherence and reproducibility". In: *Nature Communications* 7 (Nov. 2016), p. 12964. URL: http://www.nature.com/doifinder/10.1038/ncomms12964.

[14] IBM Newsroom. *Advances to IBM Quantum Systems and Ecosystem.* 2017. URL: https://www-03.ibm.com/press/us/en/pressrelease/53374.wss.

[15] R. J. Schoelkopf and S. M. Girvin. "Wiring up quantum systems". In: *Nature* 451.7179 (Feb. 2008), pp. 664–669. URL: http://www.nature.com/doifinder/10.1038/451664a.

[16] The Royal Swedish Academy of Sciences. *Measuring and Manipulating Individual Quantum Systems.* Nobelprize.org. 2012. URL: https://www.nobelprize.org/nobel_prizes/physics/laureates/2012/advanced.html.

[17] B. Yurke et al. "Observation of parametric amplification and deamplification in a Josephson parametric amplifier". In: *Physical Review A* 39.5 (Mar. 1989), pp. 2519–2533. URL: https://link.aps.org/doi/10.1103/PhysRevA.39.2519.

[18] T. Walter et al. "Rapid High-Fidelity Single-Shot Dispersive Readout of Superconducting Qubits". In: *Physical Review Applied* 7.5 (May 2017), p. 054020. URL: http://link.aps.org/doi/10.1103/PhysRevApplied.7.054020.

[19] Evan Jeffrey et al. "Fast accurate state measurement with superconducting qubits". In: *Physical Review Letters* 112.19 (May 2014).

[20] R. Vijay, D. H. Slichter, and I. Siddiqi. "Observation of Quantum Jumps in a Superconducting Artificial Atom". In: *Physical Review Letters* 106.11 (Mar. 2011), p. 110502. URL: https://link.aps.org/doi/10.1103/PhysRevLett.106.110502.

[21] K. W. Murch et al. "Observing single quantum trajectories of a superconducting quantum bit". In: *Nature* 502.7470 (Oct. 2013), pp. 211–214. URL: http://www.nature.com/doifinder/10.1038/nature12539.

[22] P. Campagne-Ibarcq et al. "Observing Quantum State Diffusion by Heterodyne Detection of Fluorescence". In: *Physical Review X* 6.1 (Jan. 2016), p. 011002. URL: https://link.aps.org/doi/10.1103/PhysRevX.6.011002.

[23] R. Vijay et al. "Stabilizing Rabi oscillations in a superconducting qubit using quantum feedback". In: *Nature* 490.7418 (Oct. 2012), pp. 77–80. URL: http://www.nature.com/doifinder/10.1038/nature11505.

[24] Nissim Ofek et al. "Extending the lifetime of a quantum bit with error correction in superconducting circuits". In: *Nature* 536 (2016). URL: https://www.nature.com/nature/journal/v536/n7617/pdf/nature18949.pdf.

[25] R. Movshovich et al. "Observation of zero-point noise squeezing via a Josephson-parametric amplifier". In: *Physical Review Letters* 65.12 (Sept. 1990), pp. 1419–1422. URL: https://link.aps.org/doi/10.1103/PhysRevLett.65.1419.

[26] B. Yurke et al. "Observation of 4.2-K equilibrium-noise squeezing via a Josephson-parametric amplifier". In: *Physical Review Letters* 60.9 (Feb. 1988), pp. 764–767. URL: https://link.aps.org/doi/10.1103/PhysRevLett.60.764.

[27] M. A. Castellanos-Beltran et al. "Amplification and squeezing of quantum noise with a tunable Josephson metamaterial". In: *Nature Physics* 4.12 (Dec. 2008), pp. 929–931. URL: http://www.nature.com/doifinder/10.1038/nphys1090.

[28] C. Eichler et al. "Quantum-Limited Amplification and Entanglement in Coupled Nonlinear Resonators". In: *Physical Review Letters* 113.11 (Sept. 2014), p. 110502. URL: https://link.aps.org/doi/10.1103/PhysRevLett.113.110502.

[29] Ulrik L Andersen et al. "30 years of squeezed light generation". In: *Physica Scripta* 91.5 (May 2016), p. 053001. URL: http://stacks.iop.org/1402-4896/91/i=5/a=053001?key=crossref.55d40e34c2e428c19fc293296c741aa3.

[30] R. E. Slusher et al. "Observation of Squeezed States Generated by Four-Wave Mixing in an Optical Cavity". In: *Physical Review Letters* 55.22 (Nov. 1985), pp. 2409–2412. URL: https://link.aps.org/doi/10.1103/PhysRevLett.55.2409.

[31] J. Abadie et al. "A gravitational wave observatory operating beyond the quantum shot-noise limit". In: *Nature Physics* 7.12 (2011), pp. 962–965. URL: http://www.nature.com/nphys/journal/v7/n12/abs/nphys2083.html.

[32] J. Aasi et al. "Enhanced sensitivity of the LIGO gravitational wave detector by using squeezed states of light". In: *Nature Photonics* 7.8 (2013), pp. 613–619.

[33] Huaixiu Zheng et al. "Accelerating dark-matter axion searches with quantum measurement technology". In: *arxiv:1607.02529* (). URL: http://arxiv.org/abs/1607.02529.

[34] K. W. Murch et al. "Reduction of the radiative decay of atomic coherence in squeezed vacuum." In: *Nature* 499.7456 (2013), pp. 62–5. URL: http://www.nature.com/nature/journal/v499/n7456/abs/nature12264.html.

[35] S. Kono et al. "Nonclassical Photon Number Distribution in a Superconducting Cavity under a Squeezed Drive". In: *Physical Review Letters* 119.2 (July 2017), p. 023602. URL: http://link.aps.org/doi/10.1103/PhysRevLett.119.023602.

[36] Jeremy B Clark et al. "Observation of strong radiation pressure forces from squeezed light on a mechanical oscillator". In: *Nature Physics* 12.7 (2016), p. 683. URL: http://www.nature.com/nphys/journal/v12/n7/full/nphys3701.html.

[37] Jeremy B Clark et al. "Sideband cooling beyond the quantum backaction limit with squeezed light". In: *Nature* 541.7636 (2017), p. 191. URL: http://www.nature.com/doifinder/10.1038/nature20604.

[38] A. Bienfait et al. "Magnetic Resonance with Squeezed Microwaves". In: *Physical Review X* 7.4 (Oct. 2017), p. 041011. URL: https://link.aps.org/doi/10.1103/PhysRevX.7.041011.

[39] B.D. Josephson. "Possible new effects in superconductive tunnelling". In: *Physics Letters* 1.7 (July 1962), pp. 251–253. URL: http://www.sciencedirect.com/science/article/pii/0031916362913690.

[40] Charles Kittel. *Introduction to Solid State Physics.* 8th. John Wiley and Sons, 2005.

[41] E. Schrödinger. "An Undulatory Theory of the Mechanics of Atoms and Molecules". In: *Physical Review* 28.6 (Dec. 1926), pp. 1049–1070. URL: https://link.aps.org/doi/10.1103/PhysRev.28.1049.

[42] Jens Koch et al. "Charge-insensitive qubit design derived from the Cooper pair box". In: *Physical Review A* 76.4 (Oct. 2007), p. 042319. URL: https://link.aps.org/doi/10.1103/PhysRevA.76.042319.

[43] Hanhee Paik et al. "Observation of High Coherence in Josephson Junction Qubits Measured in a Three-Dimensional Circuit QED Architecture". In: *Physical Review Letters* 107.24 (Dec. 2011), p. 240501. URL: https://link.aps.org/doi/10.1103/PhysRevLett.107.240501.

[44] Vladimir E Manucharyan et al. "Fluxonium: single cooper-pair circuit free of charge offsets." In: *Science (New York, N.Y.)* 326.5949 (Oct. 2009), pp. 113–6. URL: http://science.sciencemag.org/content/326/5949/113.

[45] Daniel Slichter. "Quantum Jumps and Measurement Backaction in a Superconducting Qubit". PhD thesis. University of California Berkeley, 2011. URL: http://digitalassets.lib.berkeley.edu/etd/ucb/text/Slichter_berkeley_0028E_11889.pdf.

[46] Eli Levenson-Falk. "Static and Microwave Transport Properties of Aluminum Nanobridge Josephson Junctions". PhD thesis. University of California Berkeley, 2013. URL: http://digitalassets.lib.berkeley.edu/etd/ucb/text/LevensonFalk_berkeley_0028E_13804.pdf.

[47] Mollie Schwartz. "Engineering Dissipation to Generate Entanglement Between Remote Superconducting Quantum Bits". PhD thesis. University of California Berkeley, 2016. URL: http://digitalassets.lib.berkeley.edu/etd/ucb/text/Schwartz_berkeley_0028E_16539.pdf.

[48]   Steven Weber. "Quantum Trajectories of a Superconducting Qubit". PhD thesis. University of California Berkeley, 2014. URL: `http://digitalassets.lib.berkeley.edu/etd/ucb/text/Weber_berkeley_0028E_14872.pdf`.

[49]   Jeffrey Birenbaum. "The C-shunt Flux Qubit: A New Generation of Superconducting Flux Qubit". PhD thesis. University of California Berkeley, 2014. URL: `http://digitalassets.lib.berkeley.edu/etd/ucb/text/Birenbaum_berkeley_0028E_14885.pdf`.

[50]   Christopher Macklin. "Quantum Feedback and Traveling-wave Parametric Amplication in Superconducting Circuits". PhD thesis. University of California Berkeley, 2015. URL: `http://digitalassets.lib.berkeley.edu/etd/ucb/text/Macklin_berkeley_0028E_15175.pdf`.

[51]   M. Simoen et al. "Characterization of a multimode coplanar waveguide parametric amplifier". In: *Journal of Applied Physics* 118.15 (Oct. 2015), p. 154501. URL: `http://aip.scitation.org/doi/10.1063/1.4933265`.

[52]   T. Yamamoto et al. "Flux-driven Josephson parametric amplifier". In: *Applied Physics Letters* 93.4 (July 2008), p. 042510. URL: `http://aip.scitation.org/doi/10.1063/1.2964182`.

[53]   Archana Kamal, Adam Marblestone, and Michel Devoret. "Signal-to-pump back action and self-oscillation in double-pump Josephson parametric amplifier". In: *Physical Review B* 79.18 (May 2009), p. 184301. URL: `https://link.aps.org/doi/10.1103/PhysRevB.79.184301`.

[54]   M. Malnou et al. "Optimal operation of a Josephson parametric amplifier for vacuum squeezing". In: (Nov. 2017). URL: `http://arxiv.org/abs/1711.02786`.

[55]   R. Movshovich et al. "Subharmonic pumping of a Josephson-parametric amplifier and the pitchfork instability". In: *Physical Review Letters* 67.11 (Sept. 1991), pp. 1411–1414. URL: `https://link.aps.org/doi/10.1103/PhysRevLett.67.1411`.

[56]   K. Wódkiewicz et al. "Squeezing and superposition states". In: *Physical Review A* 35.6 (Mar. 1987), pp. 2567–2577. URL: `https://link.aps.org/doi/10.1103/PhysRevA.35.2567`.

[57]   O. Naaman, D. G. Ferguson, and R. J. Epstein. "High Saturation Power Josephson Parametric Amplifier with GHz Bandwidth". In: (Oct. 2017). URL: `http://arxiv.org/abs/1711.07549`.

[58]   Manuel Castellanos Beltran. "Development of a Josephson Parametric Amplifier for the Preparation and Detection of Nonclassical States of Microwave Fields". PhD thesis. University of Colorado, 2010. URL: `https://jila.colorado.edu/sites/default/files/assets/files/publications/castellanos_thesis.pdf`.

[59]   Christopher Eichler and Andreas Wallraff. "Controlling the dynamic range of a Josephson parametric amplifier". In: *EPJ Quantum Technology* 1.1 (Dec. 2014), p. 2. URL: `http://www.epjquantumtechnology.com/content/1/1/2`.

[60] Rajamani Vijayaraghavan. "Josephson Bifurcation Amplifier: Amplifying quantum signals using a dynamical bifurcation". PhD thesis. Yale University, 2008. URL: http://qulab.eng.yale.edu/documents/theses/Vijay-PhDthesis-JosephsonBifurcationAmplifie AmplifyingQuantumSignalsUsingDynamicalBifurcation-DevoretLab-Yale2008.pdf.

[61] Tanay Roy et al. "Broadband parametric amplification with impedance engineering: Beyond the gain-bandwidth product". In: *Applied Physics Letters* 107.26 (Dec. 2015).

[62] J. Y. Mutus et al. "Strong environmental coupling in a Josephson parametric amplifier". In: *Applied Physics Letters* 104.26 (June 2014), p. 263513. URL: http://aip.scitation.org/doi/10.1063/1.4886408.

[63] V. E. Manucharyan et al. "Microwave bifurcation of a Josephson junction: Embedding-circuit requirements". In: *Physical Review B* 76.1 (July 2007), p. 014524. URL: https://link.aps.org/doi/10.1103/PhysRevB.76.014524.

[64] J. Y. Mutus et al. "Design and characterization of a lumped element single-ended superconducting microwave parametric amplifier with on-chip flux bias line". In: *Applied Physics Letters* 103.12 (Sept. 2013), p. 122602. URL: http://aip.scitation.org/doi/10.1063/1.4821136.

[65] X. Zhou et al. "High-gain weakly nonlinear flux-modulated Josephson parametric amplifier using a SQUID array". In: *Physical Review B* 89.21 (June 2014), p. 214517. URL: https://link.aps.org/doi/10.1103/PhysRevB.89.214517.

[66] C. W. Gardiner. "Inhibition of atomic phase decays by squeezed light: A direct effect of squeezing". In: *Physical Review Letters* 56.18 (1986), pp. 1917–1920. URL: https://link.aps.org/doi/10.1103/PhysRevLett.56.1917.

[67] Horace P. Yuen. "Two-photon coherent states of the radiation field". In: *Physical Review A* 13.6 (June 1976), pp. 2226–2243. URL: https://link.aps.org/doi/10.1103/PhysRevA.13.2226.

[68] Waltraut Wustmann and Vitaly Shumeiko. "Parametric resonance in tunable superconducting cavities". In: *Physical Review B* 87.18 (May 2013), p. 184501. URL: https://link.aps.org/doi/10.1103/PhysRevB.87.184501.

[69] Christopher Eichler. "Experimental Characterization of Quantum Microwave Radiation and its Entanglement with a Superconducting Qubit". PhD thesis. ETH Zurich, 2013. URL: http://e-collection.library.ethz.ch/eserv/eth:6886/eth-6886-02.pdf.

[70] Carlton M. Caves. "Quantum limits on noise in linear amplifiers". In: *Physical Review D* 26.8 (Oct. 1982), pp. 1817–1839. URL: https://link.aps.org/doi/10.1103/PhysRevD.26.1817.

[71] H. A. Haus and J. A. Mullen. "Quantum Noise in Linear Amplifiers". In: *Physical Review* 128.5 (Dec. 1962), pp. 2407–2413. URL: https://link.aps.org/doi/10.1103/PhysRev.128.2407.

[72] M. Hatridge et al. "Dispersive magnetometry with a quantum limited SQUID parametric amplifier". In: *Physical Review B* 83.13 (Apr. 2011), p. 134501. URL: https://link.aps.org/doi/10.1103/PhysRevB.83.134501.

[73] C. Eichler et al. "Observation of Two-Mode Squeezing in the Microwave Frequency Domain". In: *Physical Review Letters* 107.11 (Sept. 2011), p. 113601. URL: https://link.aps.org/doi/10.1103/PhysRevLett.107.113601.

[74] E. Flurin et al. "Generating entangled microwave radiation over two transmission lines". In: *Physical Review Letters* 109.18 (Oct. 2012), p. 093604. URL: https://link.aps.org/doi/10.1103/PhysRevLett.109.183901.

[75] M. J. Collett and C. W. Gardiner. "Squeezing of intracavity and traveling-wave light fields produced in parametric amplification". In: *Physical Review A* 30.3 (Sept. 1984), pp. 1386–1391. URL: https://link.aps.org/doi/10.1103/PhysRevA.30.1386.

[76] M. J. Collett and R. Loudon. "Output properties of parametric amplifiers in cavities". In: *Journal of the Optical Society of America B* 4.10 (Oct. 1987), p. 1525. URL: https://www.osapublishing.org/abstract.cfm?URI=josab-4-10-1525.

[77] N. E. Frattini et al. "3-wave mixing Josephson dipole element". In: *Applied Physics Letters* 110.22 (May 2017), p. 222603. URL: http://aip.scitation.org/doi/10.1063/1.4984142.

[78] B. R. Mollow. "Power Spectrum of Light Scattered by Two-Level Systems". In: *Physical Review* 188.5 (Dec. 1969), pp. 1969–1975. URL: https://link.aps.org/doi/10.1103/PhysRev.188.1969.

[79] Xiaodong Xu et al. "Coherent Optical Spectroscopy of a Strongly Driven Quantum Dot". In: *Science* 317.5840 (2007). URL: dx.doi.org/10.1126/science.1142979.

[80] O. Astafiev et al. "Resonance Fluorescence of a Single Artificial Atom". In: *Science* 327.5967 (2010). URL: dx.doi.org/10.1126/science.1181918.

[81] Arjan F. van Loo et al. "Photon Mediated Interactions Between Distant Artificial Atoms". In: *Science* 342.6165 (2013). URL: http://dx.doi.org/10.1126/science.1244324.

[82] H. J. Carmichael, A. S. Lane, and D. F. Walls. "Resonance fluorescence from an atom in a squeezed vacuum". In: *Physical Review Letters* 58.24 (June 1987), pp. 2539–2542. URL: https://link.aps.org/doi/10.1103/PhysRevLett.58.2539.

[83] H.J. Carmichael, A.S. Lane, and D.F. Walls. "Resonance Fluorescence in a Squeezed Vacuum". In: *Journal of Modern Optics* 34.6-7 (June 1987), pp. 821–840. URL: http://dx.doi.org/10.1080/09500348714550771.

[84] A. S. Parkins. "The Interaction of Squeezed Light with Atoms". In: *Modern Nonlinear Optics*. 1993. URL: http://www.tandfonline.com/doi/abs/10.1080/09500349908231278.

[85] B. J. Dalton, Z. Ficek, and S. Swain. "Atoms in squeezed light fields". In: *Journal of Modern Optics* 46.3 (Mar. 1999). URL: http://www.tandfonline.com/doi/abs/10.1080/09500349908231278.

[86] Q. A. Turchette et al. "Squeezed excitation in cavity QED". In: *Physical Review A* 58.5 (Nov. 1998), pp. 4056–4077. URL: https://link.aps.org/doi/10.1103/PhysRevA.58.4056.

[87] A. Wallraff et al. "Strong coupling of a single photon to a superconducting qubit using circuit quantum electrodynamics". In: *Nature* 431.7005 (Sept. 2004). URL: http://www.nature.com/doifinder/10.1038/nature02851.

[88] A. S. Parkins, P. Zoller, and H. J. Carmichael. "Spectral linewidth narrowing in a strongly coupled atom-cavity system via squeezed light excitation of a vacuum Rabi resonance". In: *Physical Review A* 48.1 (July 1993), pp. 758–763. URL: https://link.aps.org/doi/10.1103/PhysRevA.48.758.

[89] C. Macklin et al. "A near quantum limited Josephson traveling wave parametric amplifier". In: *Science* (2015). URL: https://doi.org/10.1126/science.aaa8525.

[90] F Schuda, C R Stroud, and M Hercher. "Observation of the resonant Stark effect at optical frequencies". In: *Journal of Physics B: Atomic and Molecular Physics* 7.7 (May 1974), pp. L198–L202. URL: https://doi.org/10.1088/0022-3700/7/7/002.

[91] K. Geerlings et al. "Demonstrating a Driven Reset Protocol for a Superconducting Qubit". In: *Physical Review Letters* 110.12 (Mar. 2013), p. 120501. URL: https://link.aps.org/doi/10.1103/PhysRevLett.110.120501.

[92] A. S. Parkins. "Resonance fluorescence of a two-level atom in a two-mode squeezed vacuum". In: *Physical Review A* 42.11 (Dec. 1990), pp. 6873–6883. URL: https://link.aps.org/doi/10.1103/PhysRevA.42.6873.

[93] A. S. Parkins. "Rabi sideband narrowing via strongly driven resonance fluorescence in a narrow-bandwidth squeezed vacuum". In: *Physical Review A* 42.7 (Oct. 1990), pp. 4352–4365. URL: https://link.aps.org/doi/10.1103/PhysRevA.42.4352.

[94] S. Swain. "Anomalous Resonance Fluorescence Spectra in a Squeezed Vacuum". In: *Physical Review Letters* 73.11 (Sept. 1994), pp. 1493–1496. URL: https://link.aps.org/doi/10.1103/PhysRevLett.73.1493.

[95] Alexandre Blais et al. "Cavity quantum electrodynamics for superconducting electrical circuits: An architecture for quantum computation". In: *Physical Review A* 69.6 (June 2004), p. 062320. URL: https://link.aps.org/doi/10.1103/PhysRevA.69.062320.

[96] Jay Gambetta et al. "Qubit-photon interactions in a cavity: Measurement induced dephasing and number splitting". In: *Physical Review A* 74.4 (Oct. 2006), p. 042318. URL: https://link.aps.org/doi/10.1103/PhysRevA.74.042318.

[97]   Shruti Puri and Alexandre Blais. "High-Fidelity Resonator-Induced Phase Gate with Single-Mode Squeezing". In: *Physical Review Letters* 116.18 (May 2016), p. 180501. URL: https://link.aps.org/doi/10.1103/PhysRevLett.116.180501.

[98]   Sh Barzanjeh, D. P. Divincenzo, and B. M. Terhal. "Dispersive qubit measurement by interferometry with parametric amplifiers". In: *Physical Review B* 90.13 (Oct. 2014). URL: https://journals.aps.org/prb/abstract/10.1103/PhysRevB.90.134515.

[99]   Nicolas Didier et al. "Heisenberg Limited Qubit Read-Out with Two-Mode Squeezed Light". In: *Physical Review Letters* 115.9 (Aug. 2015), p. 093604. URL: https://link.aps.org/doi/10.1103/PhysRevLett.115.093604.

[100] Luke C G Govia and Aashish A Clerk. "Enhanced qubit readout using locally generated squeezing and inbuilt Purcell-decay suppression". In: *New Journal of Physics* 19.2 (Feb. 2017), p. 023044. URL: http://stacks.iop.org/1367-2630/19/i=2/a=023044?key=crossref.b079710c324a028fd9d32cd2521b9ada.

[101] Nicolas Didier, Jerome Bourassa, and Alexandre Blais. "Fast Quantum Nondemolition Readout by Parametric Modulation of Longitudinal Qubit Oscillator Interaction". In: *Physical Review Letters* 115.20 (Nov. 2015), p. 203601. URL: https://link.aps.org/doi/10.1103/PhysRevLett.115.203601.

[102] Shay Hacohen-Gourgy et al. "Quantum dynamics of simultaneously measured non-commuting observables". In: *Nature* 538.7626 (2016), p. 491. URL: http://www.nature.com/nature/journal/v538/n7626/full/nature19762.html.

[103] J. B. Hertzberg et al. "Back-action-evading measurements of nanomechanical motion". In: *Nature Physics* 6.3 (Mar. 2010), pp. 213–217. URL: http://www.nature.com/doifinder/10.1038/nphys1479.

[104] J. Suh et al. "Mechanically detecting and avoiding the quantum fluctuations of a microwave field". In: *Science* 344.6189 (2014). URL: http://science.sciencemag.org/content/344/6189/1262.

[105] F Lecocq et al. "Quantum Nondemolition Measurement of a Nonclassical State of a Massive Object". In: *Physical Review X* 5.041037 (2015). URL: https://journals.aps.org/prx/pdf/10.1103/PhysRevX.5.041037.

[106] Bernard Yurke, Samuel L. McCall, and John R. Klauder. "SU(2) and SU(1,1) interferometers". In: *Physical Review A* 33.6 (June 1986), pp. 4033–4054. URL: https://link.aps.org/doi/10.1103/PhysRevA.33.4033.

[107] F. Mallet et al. "Quantum State Tomography of an Itinerant Squeezed Microwave Field". In: *Physical Review Letters* 106.22 (June 2011), p. 220502. URL: http://link.aps.org/doi/10.1103/PhysRevLett.106.220502.

[108] C. Laflamme and A. A. Clerk. "Weak Qubit Measurement with a Nonlinear Cavity: Beyond Perturbation Theory". In: *Physical Review Letters* 109.12 (Sept. 2012), p. 123602. URL: https://link.aps.org/doi/10.1103/PhysRevLett.109.123602.

[109] D.M. Pozar. *Microwave Engineering*. 3rd ed. (Pozar has a section on noise figure of a cascaded system, but does not refer to this as Friis's formula explicitly.) John Wiley and Sons, 2005.

[110] H Le Jeannic et al. "Slowing Quantum Decoherence by Squeezing in Phase Space". In: *arXiv:1707.06244* (). URL: https://arxiv.org/pdf/1707.06244.pdf.

[111] Jeffrey H. Shapiro. "Optical waveguide tap with infinitesimal insertion loss". In: *Optics Letters* 5.8 (Aug. 1980), p. 351. URL: https://www.osapublishing.org/abstract.cfm?URI=ol-5-8-351.

[112] J. A. Levenson et al. "Quantum optical cloning amplifier". In: *Physical Review Letters* 70.3 (Jan. 1993), pp. 267–270. URL: https://link.aps.org/doi/10.1103/PhysRevLett.70.267.

[113] K. M. Sliwa et al. "Reconfigurable josephson circulator/directional amplifier". In: *Physical Review X* 5.4 (2015). URL: https://link.aps.org/doi/10.1103/PhysRevX.5.041020.

[114] Joseph Kerckhoff et al. "On-Chip Superconducting Microwave Circulator from Synthetic Rotation". In: *Physical Review Applied* 4.3 (Sept. 2015). URL: https://link.aps.org/doi/10.1103/PhysRevApplied.4.034002.

[115] Benjamin J. Chapman et al. "Widely Tunable On-Chip Microwave Circulator for Superconducting Quantum Circuits". In: *Physical Review X* 7.4 (Nov. 2017), p. 041043. URL: https://link.aps.org/doi/10.1103/PhysRevX.7.041043.

[116] Benjamin Levitan. "Dispersive qubit measurement using an on-chip parametric amplifier". MA thesis. McGill University, 2015. URL: http://digitool.library.mcgill.ca/R/-?func=dbin-jump-full&object_id=138943&silo_library=GEN01.

[117] A. Metelmann and A. A. Clerk. "Nonreciprocal Photon Transmission and Amplification via Reservoir Engineering". In: *Physical Review X* 5.2 (June 2015), p. 021025. URL: https://link.aps.org/doi/10.1103/PhysRevX.5.021025.

[118] F. Lecocq et al. "Nonreciprocal Microwave Signal Processing with a Field-Programmable Josephson Amplifier". In: *Physical Review Applied* 7.2 (Feb. 2017), p. 024028. URL: https://link.aps.org/doi/10.1103/PhysRevApplied.7.024028.

[119] T. Thorbeck et al. "Reverse Isolation and Backaction of the SLUG Microwave Amplifier". In: *Physical Review Applied* 8.5 (Nov. 2017), p. 054007. URL: https://link.aps.org/doi/10.1103/PhysRevApplied.8.054007.

[120] I. Siddiqi et al. "RF-Driven Josephson Bifurcation Amplifier for Quantum Measurement". In: *Physical Review Letters* 93.20 (Nov. 2004), p. 207002. URL: http://link.aps.org/doi/10.1103/PhysRevLett.93.207002.

[121] Philip Krantz et al. "Single-shot read-out of a superconducting qubit using a Josephson parametric oscillator". In: *Nature Communications* 7 (May 2016), p. 11417. URL: http://www.nature.com/doifinder/10.1038/ncomms11417.

[122] V. Schmitt et al. "Multiplexed readout of transmon qubits with Josephson bifurcation amplifiers". In: *Physical Review A* 90.6 (Dec. 2014), p. 062333. URL: `https://link.aps.org/doi/10.1103/PhysRevA.90.062333`.

[123] Maxime Boissonneault et al. "Back-action of a driven nonlinear resonator on a super-conducting qubit". In: *Physical Review A* 85.2 (Feb. 2012), p. 022305. URL: `https://link.aps.org/doi/10.1103/PhysRevA.85.022305`.

[124] F. R. Ong et al. "Quantum Heating of a Nonlinear Resonator Probed by a Super-conducting Qubit". In: *Physical Review Letters* 110.4 (Jan. 2013), p. 047001. URL: `https://link.aps.org/doi/10.1103/PhysRevLett.110.047001`.

[125] Maxime Boissonneault et al. "Superconducting qubit as a probe of squeezing in a nonlinear resonator". In: *Physical Review A* 89.2 (Feb. 2014), p. 022324. URL: `https://link.aps.org/doi/10.1103/PhysRevA.89.022324`.

[126] E M Levenson-Falk et al. "A dispersive nanoSQUID magnetometer for ultra-low noise, high bandwidth flux detection". In: *Superconductor Science and Technology* 26.5 (May 2013), p. 055015. URL: `http://stacks.iop.org/0953-2048/26/i=5/a=055015?key=crossref.ca38a1d45372170e539cae5365811bbc`.

[127] Jay Gambetta et al. "Protocols for optimal readout of qubits using a continuous quantum nondemolition measurement". In: *Physical Review A* 76.1 (July 2007), p. 012325. URL: `https://link.aps.org/doi/10.1103/PhysRevA.76.012325`.